

8269



Density Functional Theory Study of Structural and Magnetic Properties of Low Dimensional Systems

A Thesis

Submitted For the Degree of
DOCTOR OF PHILOSOPHY
in the Faculty of Science

by

Mighfar Imam



THEORETICAL SCIENCES UNIT
JAWAHARLAL NEHRU CENTRE FOR ADVANCED SCIENTIFIC
RESEARCH
Bangalore - 560 064

JUNE 2012

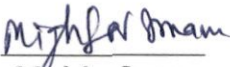
620.112 97
P12

To my parents

DECLARATION

I hereby declare that the matter embodied in the thesis entitled “**Density Functional Theory Study of Structural and Magnetic Properties of Low Dimensional Systems**” is the result of investigations carried out by me at the Theoretical Sciences Unit, Jawaharlal Nehru Centre for Advanced Scientific Research, Bangalore, India under the supervision of Prof. Shobhana Narasimhan and that it has not been submitted elsewhere for the award of any degree or diploma.

In keeping with the general practice in reporting scientific observations, due acknowledgement has been made whenever the work described is based on the findings of other investigators.


Mghfar Imam

CERTIFICATE

I hereby certify that the matter embodied in this thesis entitled “**Density Functional Theory Study of Structural and Magnetic Properties of Low Dimensional Systems**” has been carried out by Mr. Mighfar Imam at the Theoretical Sciences Unit, Jawaharlal Nehru Centre for Advanced Scientific Research, Bangalore, India under my supervision and that it has not been submitted elsewhere for the award of any degree or diploma.



Prof. Shobhana Narasimhan

(Research Supervisor)

Acknowledgement

First of all I would like to express my sincere thanks to my thesis advisor, Prof. Shobhana Narasimhan, for all her scientific and non-scientific helps, through out the entire period of my Ph.D. It would have been really impossible for me to finish my Ph.D without her showing faith and confidence in me. She not only guided me in the scientific work, but also gave me valuable pieces of advice about life, both from a practical as well as philosophical perspectives. Spending more than some six valuable years under her guidance, I gained maturity of thought and developed a more clear vision of life and its objectives. During difficult periods of my Ph.D, when I was suffering from sheer stress and negativity, she went out of her ways to help me come out of these, and offered me her valuable treasure of experience. In addition to her own advice, she gave me some good books to read, which proved really helpful to me. I would really cherish these times which helped me become a better human being.

My respectful gratitude towards Prof. M. R. S. Rao, the President of JNCASR and Prof. C. N. R. Rao, the founding president of JNCASR, for providing excellent research facilities and creating a good scientific environment. Many thanks to Prof. Rahul Pandit, Prof. Srikanth Sastry, Prof. Swapan K. Pati, Dr. N. S. Vidhyadhiraja, Prof. Chandrabhas Narayana, for all the things they have taught me through the courses they offered.

I would like to acknowledge my collaborators Prof. Sylvic Rousset, Prof. Vincent Repain from the University of Paris Diderot, Paris, France and Prof. Cyrille Barreteau from CEA Saclay, Cedex, France.

My special thanks to Prof. S. Balasubramanian and Prof. G. U. Kulkarni, who went out of their ways to help me provide computational resources to make me able to finish my calculations in time. I would also like to thank Prof. K. S. Narayan and Prof. Hemabalram who, as deans of students in their respective tenure, were specially considerate towards me. I would like to thank Mrs. G. Sukanya and Dr. Princy Pereira from the academic section for all their help and tolerance. I am thankful to the staff of the centre

for computational material science (CCMS), especially to Mr. Amit Patel and Ms. Bharati, for providing all the help and support with the computing resources. I would also like to thank all the staffs of the computer laboratory, library, academic section and the administrative office.

I am specially thankful to my lovely labmates– Prasenjit, Jaita, Madhura, Kanchan, Sananda, Nisha, Vasudevan, Lakshmi and Bulumoni– for providing such a pleasant environment in the lab. Kanchan, Nisha and Madhura should be given special mention for their help in the most crucial time: when I had to meet the deadline for the thesis submission. I am indebted to them and would cherish the time I spent with all of them.

I would like to thank UGC-CSIR, India, for providing me with a research scholarship. I am also very thankful to the Indo French Centre for the Promotion of Advanced Research (CEFIPRA) and the department of science and technology (DST), India, for the funding. I am extremely grateful to my advisor Prof. Shobhana Narasimhan for the arrangement of these fundings. Lastly, I thank all my friends and well-wishers whose names, though not mentioned here, dwell in my memory and heart.

Synopsis

This is the synopsis of the thesis entitled “Density Functional Theory Study of Structural and Magnetic Properties of Low Dimensional Systems” by Mighfar Imam.

The work presented in this thesis involves the study of magnetic nanostructures in low dimensions, using density functional theory. Materials in low dimensions are at the heart of current scientific and technological investigations. In particular, their magnetic properties constitute an exciting field of research, being stimulating both for fundamental physics and for many potential applications. With the reduction of dimensionality, the coordination number of atoms gets reduced. This change in atomic environment from the bulk state results in an enhancement in many magnetic properties. Effects that are either not present or only weakly present in the bulk state now get manifested strongly. Thus, nanomagnetism is a field of great interest today. The systems studied in this thesis consist of thin layers of magnetic materials (either a magnetic material, or an alloy composed of a magnetic element and a “non-magnetic” element), deposited on a substrate of another metal. We have also investigated the way in which these properties can be modified by the subsequent deposition of a self-assembled monolayer of organic molecules. In order to see whether we can gauge trends as a function of lattice constant and dimensionality, and to evaluate the effects of deposition on a substrate, we have also studied hypothetical model systems consisting of monoatomic wires and free-standing two dimensional monolayers of atoms.

We have mainly focused on the magnetic properties of these systems, viz., the magnetic moments and the magnetic anisotropy energy (MAE). The MAE,

which serves as a measure of the ease of flipping the orientation of magnetization, is of vital technological importance, for applications in magnetic memory storage. For the case of alloys, we have also evaluated the enthalpy of mixing, i.e., we have seen whether it is favorable for the alloy to form (as opposed to phase segregate), and tried to understand the different effects responsible for this.

All of the work in this thesis has been motivated by the attempt to understand specific experimental data and/or guide future experiments.

We have split the thesis work in to seven chapters. A brief description of the chapters is outlined as follows:

In Chapter 1, we provide a general introduction and the outline of the thesis. Chapter 2 describes the theoretical method, namely density functional theory (DFT), in the plane-wave pseudopotential approach, which has been used in all our work. After introducing the standard Kohn-Sham approach of DFT for the nonmagnetic systems, with standard approximations for the exchange-correlation, we have described how to treat collinear and non-collinear magnetism, and how to include the spin-orbit interaction, as is necessary in order to calculate the MAE. In our approach, this is done by making use of fully relativistic pseudopotentials.

In Chapter 3, we present a brief review of some magnetic properties related to our work and describe some general concepts related to magnetism and magnetic anisotropy. We also describe some experimental and theoretical methods for the measurement and calculation of magnetic anisotropy.

In Chapter 4, we study surface alloys of the type MN/S , where M is a magnetic element, N is a “non-magnetic” element, and S is a substrate (which, in our case, is restricted to Rh(111)). This work was in part motivated by experiments by Thayer *et al.* that showed that Ag-Co/Ru(0001) did not form an atomically mixed alloy, despite expectations to the contrary. In our work, we study the structural and magnetic properties of quasi-two-dimensional magnetic surface alloys of the type M_xN_{1-x} , (M =Fe, Co, Ni; N =Pt, Au, Ag, Cd, Pb; and the concentration $x = 0, 0.25, 0.33, 0.5, 0.67, 0.75, 1$), on a Rh(111) substrate. The choice of elements is made keeping in mind the Hume-Rothery alloying criterion for bulk alloys, which may, however, not

hold at the surface. Many compositions and geometric patterns of the surface alloys are considered, in order to study their mixing as well as magnetic behavior. We grouped all the patterns into two types, the linear chain type and “Chinese checkerboard” type, and compared their mixing and magnetic properties. We find that some of the combinations of these magnetic and nonmagnetic elements result in mixing (even though they are immiscible in the bulk), while some show no or very small mixing. Both chemical and elastic contributions to mixing are found to be important. We find that the greater the number the valence electrons in N , the smaller the magnetic moments in the alloy; this finding can be explained by simple density-of-states arguments. We identify suitable candidates that would be appropriate for future experiments.

In Chapter 5, we study the structural and magnetic properties of thin films of Co on Au(111), as well as how these are modified upon the subsequent adsorption of methane thiolate (CH_3S) on the Co/Au(111) substrate. With a clever choice of our unit cell we could simulate the reconstructed Co film on Au(111), which mimics the experimental structure rather well. We checked the stability of clean and thiol-adsorbed Co/Au(111) for various stackings sequences. We also studied the properties of pseudomorphic Co layers on Au(111). In all cases, we find an out-of-plane easy axis for the system. We find that the adsorption of methane thiolate slightly reduces the MAE when three Co layers are present; however, preliminary results suggest that this effect is considerably reduced when the number of Co layers is increased. These investigations were motivated by unpublished experimental investigations by Rousset, Repain *et al.*

Chapter 6 deals with the structural and magnetic properties (with focus on the magnetic anisotropy energy) of Fe in low dimensions: one-dimensional Fe chains, two-dimensional square and triangular lattices, and a monolayer of Fe on Au(111). We note that the Fe/Au(111) system has been studied experimentally by various authors. There is some uncertainty in the literature, about whether the easy axis lies in-plane, out-of-plane, or in a cone that is tilted to the plane. For the pure Fe systems, we obtain results that are similar to those of previous authors, though our study considers a wider

range of lattice constants. For Fe/Au(111), we obtain the surprising and interesting result that the sign of the MAE can be switched by changing the stacking of the Fe monolayer and/or the top Au layer, which may explain the range of results obtained by previous experimental authors.

Finally, in Chapter 7, we summarize our work and conclude with open questions which still remain to be answered, and a survey of future prospects.

List of Publications

1. Mighfar Imam and Shobhana Narasimhan, Magnetism of surface alloys of the type $M_xN_{1-x}/\text{Rh}(111)$, *Journal of Magnetism and Magnetic Materials*, **323**, 1873 (2011).
2. Madhura Marathe, Mighfar Imam and Shobhana Narasimhan, Mixing and Magnetic Properties of Surface Alloys: The Role of the Substrate, *Applied Surface Science*, **256**, 449 (2009).
3. Madhura Marathe, Mighfar Imam and Shobhana Narasimhan, Elastic and chemical contributions to the stability of magnetic surface alloys on Ru(0001), *Physical Review B*, **79**, 085413 (2009).
4. Mighfar Imam, Madhura Marathe and Shobhana Narasimhan, $\text{Ni}_x\text{Pt}_{1-x}/\text{Rh}(111)$: A Stable Surface Alloy with Enhanced Magnetic Moments, *Solid State Communications*, **149**, 559 (2009).
5. Mighfar Imam, Madhura Marathe and Shobhana Narasimhan, Competition between elastic and chemical effects in the intermixing of Ag and Co on Rh(111), *J. Chem. Sci.*, **120**, 621 (2008).

List of Abbreviations

E_f	Fermi Energy
I	Stoner exchange parameter
M_{tot}	total magnetic moment
μeV	micro electron-volts
μ_B	Bohr Magnetron
0D	zero-dimensional
1D	one-dimensional
2D	two-dimensional
3D	three-dimensional
bcc	body-centered cubic
BZ	Brillouin zone
CB	Checkerboard
DFT	Density Functional Theory
$\text{DOS}(E_f)$	Density of states at the Fermi energy
DOS	Density of states
eV	electron-volts

fcc face-centered cubic

FLAPW Full Potential Linearized Augmented Plane Wave

GGA generalized gradient approximation

GMR Giant Magnetoresistance

H-F Hellman Feynman

H-K Hohenberg Kohn

hcp hexagonal closed packing

IBZ Irreducible Brillouin zone

KKR Korringa-Kohn-Rostoker

KS Kohn Sham

LAPW Linearized Augmented Plane wave

LDA local density approximation

PDOS local density of states

LEED Low-energy electron diffraction

LMTO-ASA linear muffin-tin orbital method with the atomic-sphere approximation

LMTO linear muffin-tin orbital

LSDA local spin density approximation

MAE Magnetic Anisotropy Energy

meV mili electron-volts

ML Monolayer

M a magnetic element

MOKE magneto-optic Kerr effect

N a nonmagnetic element

NN nearest-neighbor

NP nanoparticle

NSP non spin-polarized

PDOS projected density of states

PP pseudopotential

PWscf Plane Wave self-consistent field

QE Quantum-ESPRESSO

RKKY Rudermann-Kittel-Kasuya-Yoshida

Ry Rydbergs

SAM Self-assembled monolayers

scf self-consistent field

SCLO self-consistent local orbital

SE Schrödinger equation

SMM single molecule magnets

SOC spin-orbit coupling

SQUID superconducting quantum interference device

SRT spin reorientation transition

STM scanning tunneling microscopy

TM transition metal

USPP ultrasoft pseudopotential

XMCD X-ray circular magnetic dichroism

List of Figures

2.1	Flow chart showing the self-consistency loop for the iterative solution of the KS equation. Superscripts indicate the iteration.	23
3.1	The energy of a typical magnetic system as a function of the orientation of magnetization. The easy axis, the hard axis and the magnetic anisotropy energy (MAE) are shown.	50
4.1	Top views of structural arrangements. (a) monolayer of N, i.e., $x=0$; (b) $x=0.5$ for (2×1) cell; (c) & (d) $x=0.33$ and 0.67 for (3×1) cell; (e) & (f) $x=0.33$ and 0.67 for $(\sqrt{3}\times\sqrt{3})$ cell; (g) & (h) $x=0.25$ and 0.75 for (2×2) cell; (i) to (k) $x=0.25$, 0.5 and 0.75 for (4×1) cell; and (l) monolayer of M. Magnetic atoms are represented by red spheres, nonmagnetic atoms by yellow spheres and the grey spheres represent the substrate atoms. The black solid lines mark surface unit cells.	75
4.2	Surface stress (σ_{xx}^{surf}) versus in plane nearest-neighbor distance, l_{xy} , for the monolayers on Rh(111). Black symbols denote the data points taken by compressing/stretching the slab and lines are the fit derived from Morse potential (Eq. 4.3.). For magnetic elements (Fe, Co, Ni), the calculations were done for both, the spin-polarized (SP) (filled circles and solid lines) as well as non spin-polarized (NSP) case (unfilled circles and dotted lines).	83

4.3	<p>Enthalpy of mixing ΔH of surface alloys with respect to composition x: ΔH is measured relative to pure monolayer configuration according to Eq. (1). ΔH for a given alloy is plotted for two different structural patterns: linear striped structures [corresponding to (2×1), (3×1) and (4×1) cells and denoted as "LS"] and the "Chinese checkerboard" structures [corresponding to the (2×2) and $(\sqrt{3} \times \sqrt{3})$ cells denoted as "CB"]. The two different colors of a given symbol (e.g., magenta and orange colors for the down-pointing-triangle) denote these two structures for the given alloy. The stars of a given color correspond to the (2×1) cell for the alloy of the corresponding nonmagnetic element. (a), (b) and (c) denote the surface alloys of the Fe, Co and Ni respectively.</p>	86
4.4	<p>Side view of the Fe-Pb alloys structures: (a) for $x=0.67$ and (b) for $x=0.33$ composition. Red, yellow and grey spheres are the Fe, Pb and Rh atoms respectively. See the larger buckling when the concentration of Pb atoms is high.</p>	90
4.5	<p>The difference of the enthalpy of mixing between spin polarized and non spin polarized calculations with respect to composition x: The enthalpy difference is plotted for two different structural patterns: linear striped structures [corresponding to (2×1), (3×1) and (4×1) cells and denoted as "LS"] and the "Chinese checkerboard" structures [corresponding to the (2×2) and $(\sqrt{3} \times \sqrt{3})$ cells denoted as "CB"]. The two different colors of a given symbol (e.g., magenta and orange colors for the down-pointing-triangle) denote these two structures for the given alloy. The stars of a given color correspond to the (2×1) cell for the alloy of the corresponding nonmagnetic element. (a), (b) and (c) denote the surface alloys of the Fe, Co and Ni respectively.</p>	91
4.6	<p>Contribution to the elastic energy ΔH^{ela} from the three types of bonds: M-M, N-N, and M-N for $x=0.5$ of the (2×2) cell.</p>	99

- 4.7 Enthalpy of mixing ΔH , together with the elastic and chemical contributions, as a function of x , the fraction of magnetic element, for Pt alloys. The first, second and the third row correspond to the total enthalpy of mixing (ΔH), the elastic contribution (ΔH^{ela}) and the chemical contribution (ΔH^{chem}) respectively. The three columns correspond to the alloys with the three magnetic elements, shown on the top of graph. The filled and the unfilled symbols [solid and dotted stars for (2×1) cells] correspond to the spin-polarized and the non spin-polarized cases respectively. Circles denote the Chinese checkerboard structures and triangles and stars denote the linear striped structures. 100
- 4.8 Enthalpy of mixing ΔH , together with the elastic and chemical contributions, as a function of x , the fraction of magnetic element, for Au alloys. The first, second and the third row correspond to the total enthalpy of mixing (ΔH), the elastic contribution (ΔH^{ela}) and the chemical contribution (ΔH^{chem}) respectively. The three columns correspond to the alloys with the three magnetic elements, shown on the top of graph. The filled and the unfilled symbols [solid and dotted stars for (2×1) cells] correspond to the spin-polarized and the non spin-polarized cases respectively. Circles denote the Chinese checkerboard structures and triangles and stars denote the striped structures. Note that the plots are not on the same scale. 101

- 4.9 Enthalpy of mixing ΔH , together with the elastic and chemical contributions, as a function of x , the fraction of magnetic element, for Λg alloys. The first, second and the third row correspond to the total enthalpy of mixing (ΔH), the elastic contribution (ΔH^{ela}) and the chemical contribution (ΔH^{chem}) respectively. The three columns correspond to the alloys with the three magnetic elements, shown on the top of graph. The filled and the unfilled symbols [solid and dotted stars for (2×1) cells] correspond to the spin-polarized and the non spin-polarized cases respectively. Circles denote the Chinese checkerboard structures and triangles and stars denote the striped structures. Note that the plots are not on the same scale. 102
- 4.10 Enthalpy of mixing ΔH , together with the elastic and chemical contributions, as a function of x , the fraction of magnetic element, for Cd alloys. The first, second and the third row correspond to the total enthalpy of mixing (ΔH), the elastic contribution (ΔH^{ela}) and the chemical contribution (ΔH^{chem}) respectively. The three columns correspond to the alloys with the three magnetic elements, shown on the top of graph. The filled and the unfilled symbols [solid and dotted stars for (2×1) cells] correspond to the spin-polarized and the non spin-polarized cases respectively. Circles denote the Chinese checkerboard structures and triangles and stars denote the striped structures. 103

- 4.11 Enthalpy of mixing ΔH , together with the elastic and chemical contributions, as a function of x , the fraction of magnetic element, for Pb alloys. The first, second and the third row correspond to the total enthalpy of mixing (ΔH), the elastic contribution (ΔH^{ela}) and the chemical contribution (ΔH^{chem}) respectively. The three columns correspond to the alloys with the three magnetic elements, shown on the top of graph. The filled and the unfilled symbols [solid and dotted stars for (2×1) cells] correspond to the spin-polarized and the non spin-polarized cases respectively. Circles denote the Chinese checkerboard structures and triangles and stars denote the striped structures. 104
- 4.12 Total magnetic moment, M_{tot} (in μ_B), versus composition x for Fe alloys. M_{tot} is the magnetic moment of the whole cell divided by the number of magnetic atoms on the surface. The filled symbols correspond to the (2×2) and $(\sqrt{3} \times \sqrt{3})$ structures and the unfilled symbols correspond to the (4×1) and (3×1) structures. The stars correspond to the (2×1) cell. CB and LS refer to checkerboard and linear stripe structures respectively. 107
- 4.13 Total magnetic moment, M_{tot} (in μ_B), versus composition x for Co alloys. M_{tot} is the magnetic moment of the whole cell divided by the number of magnetic atoms on the surface. The filled symbols correspond to the (2×2) and $(\sqrt{3} \times \sqrt{3})$ structures and the unfilled symbols correspond to the (4×1) and (3×1) structures. The stars correspond to the (2×1) cell. CB and LS refer to checkerboard and linear stripe structures respectively. 108

4.14	Total magnetic moment, M_{tot} (in μ_B), versus composition x for Ni alloys. M_{tot} is the magnetic moment of the whole cell divided by the number of magnetic atoms on the surface. The filled symbols correspond to the (2×2) and $(\sqrt{3} \times \sqrt{3})$ structures and the unfilled symbols correspond to the (4×1) and (3×1) structures. The stars correspond to the (2×1) cell. CB and LS refer to checkerboard and linear stripe structures respectively.	109
4.15	The variation of the average magnetic moment of Fe (in μ_B per Fe atom) in Fe alloys, with concentration x . Filled and unfilled symbols refer to checkerboard (CB) and linear stripe (LS) structures respectively. Stars denote the $x=0.5$ composition of the (2×1) cell.	115
4.16	The variation of the average magnetic moment of Co (in μ_B per Co atom) in Co alloys, with concentration x . Filled and unfilled symbols refer to checkerboard (CB) and linear stripe (LS) structures respectively. Stars denote the $x=0.5$ composition of the (2×1) cell.	116
4.17	The variation of the average magnetic moment of Ni (in μ_B per Ni atom) in Ni alloys, with concentration x . Filled and unfilled symbols refer to checkerboard (CB) and linear stripe (LS) structures respectively. Stars denote the $x=0.5$ composition of the (2×1) cell.	117
4.18	The magnetic moments (in μ_B per magnetic atom) plotted as the difference between the total moment (M_{tot}) and the moment on the magnetic atoms ($M(M)$), with respect to the concentration x , for (a) Fe-alloys, (b) Co-alloys and (c) Ni-alloys. Filled and unfilled symbols refer to checkerboard (CB) and linear stripe (LS) structures respectively. Stars denote the $x=0.5$ composition of the (2×1) cell.	118

- 4.19 The variation of the induced magnetic moments (in μ_B per magnetic atom) of the nonmagnetic surface alloy atoms, $M(N)$, with the concentration x for (a) Fe-alloys, (b) Co-alloys and (c) Ni-alloys. Filled and unfilled symbols refer to checkerboard (CB) and linear stripe (LS) structures respectively. Stars denote the $x=0.5$ composition of the (2×1) cell. 119
- 4.20 Spin-polarized charge density isosurface for $x = 0.5$ Fe-Pt alloys (for the 2×2 cell). The isosurface corresponds to a charge density of 0.07 electrons/ \AA^3 . Red, blue and grey solid spheres denote Fe, Pt and Rh atoms respectively. The spin-polarized charge density around the Fe as well as the Pt and the top substrate layer atoms can be clearly seen. 120
- 4.21 Behavior of induced moments for monolayers of $M/\text{Rh}(111)$: the oscillatory decay of the induced magnetization (in μ_B per magnetic atom) of the substrate layers with their distance from the top magnetic monolayer (Fe, Co and Ni). Solid lines are the fits by the expression described in the text (Eq. 4.13). Circles are the data points. 122
- 4.22 Non-spin-polarized density of states (DOS) of the (a) magnetic, (b) the substrate and Pt and of (c) Au, Ag, Cd and Pb elements in their bulk phase. Note the high $\text{DOS}(E_f)$ for magnetic elements. Among the nonmagnetic elements, Pt shows the highest $\text{DOS}(E_f)$ 123
- 4.23 Total magnetic moment, M_{tot} (in μ_B per magnetic atom), versus the total non spin-polarized density of states (at E_f) per magnetic atom for (a) Fe, (b) Co and (c) Ni alloys for the four compositions ($x=0.25, 0.50, 0.75, 1.0$) of the (2×2) cell. The points where all the curves meet corresponds to $x=1.0$ 124
- 4.24 d density of states (states/eV) of Fe atom in its surface alloys for different compositions and structures: (a) for Fe-Pt, (b) for Fe-Au, (c) for Fe-Ag, (d) for Fe-Cd and (e) for Fe-Pb. The dashed vertical lines indicate the positions of the Fermi levels. 125

4.25	Density of states of the five d orbitals of Fe atom in (a) $\text{Fe}_{0.25}\text{Ag}_{0.75}/\text{Rh}(111)$, (b) $\text{Fe}_{0.75}\text{Ag}_{0.25}/\text{Rh}(111)$, (c) $\text{Fe}/\text{Rh}(111)$ (Fe monolayer) and (d) bulk Fe. The dashed vertical lines indicate the positions of the Fermi levels.	126
4.26	d density of states (states/eV) of Ni atom in its surface alloys for different compositions and structures: (a) for Ni-Pt, (b) for Ni-Au, (c) for Ni-Ag, (d) for Ni-Cd and (e) for Ni-Pb. The dashed vertical lines indicate the positions of the Fermi levels.	127
4.27	Density of states of the five d orbitals of Ni atom in (a) $\text{Ni}_{0.25}\text{Pb}_{0.75}/\text{Rh}(111)$, (b) $\text{Ni}_{0.75}\text{Pb}_{0.25}/\text{Rh}(111)$, (c) $\text{Ni}/\text{Rh}(111)$ (Ni monolayer) and (d) bulk Ni. The dashed vertical lines indicate the position of the Fermi level.	128
4.28	Magnetic moment of magnetic elements, $M(M)$, versus the effective coordination number, n_{eff} , for (a) Fe, (b) Co and (c) Ni alloys, for the four compositions of a (2×2) cell: $x = 0.25, 0.5, 0.75, 1.0$. The point where all curves meet corresponds to $x = 1.0$	132
5.1	Schematic representation of a self-assembled monolayer (SAM) on a substrate (from wikipedia).	138
5.2	(a) Side view of the 1 ML Co/Au(111) in (1×1) surface unit cell (the vacuum region above the Co atoms is truncated). (b) coordinate system defining the θ (polar angle) and ϕ (azimuthal angle). (c) The three-fold hollow sites on the fcc (111) surface. The two hollow sites labeled as "B" (inside the down-pointing-triangles) and "C" (inside the up-pointing-triangles) are shown with the atoms (yellow spheres) occupying the "A" sites (not mentioned in the figure).	147

- 5.3 Top view of the interface structure of the reconstructed Co/Au(111) system showing Co (blue color spheres) and Au atoms (yellow color spheres). The black lines mark the surface unit cells. Note that the same surface unit cell serves as a $(\sqrt{3} \times \sqrt{3})$ cell for the Au layers and (2×2) cell for the Co layers. Also the Co overlayer is rotated by 30° with respect to the Au layer. . . 148
- 5.4 Structures (side view) of (a) 4 ML pseudomorphic and (b) 3ML reconstructed Co/Au(111) in $(\sqrt{3} \times \sqrt{3})$ cell. Blue and yellow spheres represent cobalt and gold atoms respectively. Vertical black lines mark the unit cells; z-axis is along the vertical direction. 149
- 5.5 The side view of the 3 ML reconstructed $\text{CH}_3\text{S}/\text{Co}/\text{Au}(111)$ in the hcp stacking of Co. The atoms are shown as spheres with their atomic symbols written on them. The vertical black lines mark the unit cells; z-axis is in vertical direction. In each unit cell, there are three Co layers with four atoms per layer and five Au layers with three atoms per layer. 150
- 5.6 Magnetic moment per Co atom for different thicknesses of Co layers in Co/Au(111) for considered stackings. The symbols, for a given n , in the decreasing order of stability are : circle, square, up-pointing-triangle, left-pointing-triangle, down-pointing-triangle, right-pointing-triangle, plus, cross and star signs. 157
- 5.7 Top view of the (a) pseudomorphic and the (b) reconstructed Co/Au(111) (hcp) system in $(\sqrt{3} \times \sqrt{3})$ cell showing the in-plane Co distances. The green spheres are the top Co layer atoms, while the brown spheres represent the Co atoms below the top Co layer. The red spheres are the Au atoms. The numbers are the in-plane interatomic distances (in Å) marked by the white lines in (b) and black lines in (a); and rhombi mark the surface unit cells used in our calculations. 160

- 5.8 Top view of the the reconstructed hcp $\text{CH}_3\text{S}/\text{Co}/\text{Au}(111)$ system in $(\sqrt{3} \times \sqrt{3})$ cell showing the in-plane Co distances. The green spheres are the top Co layer atoms, the brown spheres represent the Co atoms below the top Co layer while the red spheres are the Au atoms. The numbers are the in-plane interatomic distances (in \AA) marked by the white lines; the rhombi (black lines) mark the surface unit cells used in our calculations. 162
- 5.9 Projected magnetic moments (in μ_B) on the individual atoms of the reconstructed (a) $\text{CH}_3\text{S}/\text{Co}/\text{Au}(111)$ and (b) $\text{Co}/\text{Au}(111)$ systems are shown (labelled against the atoms). The moments on the Au, C and H atoms are negligible and not shown here. Only part of the side view of the full unit cell is shown. 164
- 5.10 Spin polarized, projected d -density of states of the top Co layer/Co atom for the 3 ML reconstructed $\text{Co}/\text{Au}(111)$, the $\text{Co}(0001)$ and the methanethiolate/ $\text{Co}/\text{Au}(111)$ systems. For the methanethiolate/ $\text{Co}/\text{Au}(111)$ system, three out of four surface layer atoms in the unit cell are equivalent (those bonded directly to thiol) and one is different. 165
- 5.11 (a) Local density of states (LDOS) integrated over the volume of region I (shown in (b)) of the reconstructed hcp $\text{CH}_3\text{S}/\text{Co}/\text{Au}(111)$ and $\text{Co}/\text{Au}(111)$. The dashed vertical line shows the position of the Fermi level. (b) side view of (part of) the unit cell of the reconstructed hcp $\text{CH}_3\text{S}/\text{Co}/\text{Au}(111)$ showing the planes (in black color) forming the boundary of regions I and II along the z direction. 166
- 5.12 The planar average of the charge difference along the z axis (in units of electronic charge per \AA^2) for the 3 ML reconstructed hcp $\text{CH}_3\text{S}/\text{Co}/\text{Au}(111)$. (a) Side view of the unit cell of $\text{CH}_3\text{S}/\text{Co}/\text{Au}(111)$ system along the z -direction, (b) the variation of the planar average of the charge transfer as a function of distance (in \AA) along the z -axis. A decrease in charge density near the Co surface and an increase near the sulfur is clearly visible. 168

6.1	Spin magnetic moments as a function of interatomic distance of Fe chain.	185
6.2	Magnetic anisotropy energy (in meV per Fe atom) of isolated Fe chain at the interatomic distances of 2.3 and 2.87 Å with respect to the number of k-points in the one-dimensional Brillouin-zone.	186
6.3	Variation of the magnetic anisotropy energy as a function of interatomic distance for the monoatomic Fe chain. Comparison with two previous references (employing different exchange-correlation functional, LDA (Ref [259]) and GGA (Ref [261])) is also made.	187
6.4	Electronic band structures of the monoatomic Fe chain at the interatomic distances of 2.0 Å (upper panel) and 2.86 Å (lower panel). (a) and (d) with scalar relativistic calculation; (b), (c), (e) and (f) with spin-orbit interaction taken into account. “Parallel and “Perpendicular denote the results from fully relativistic calculations with the magnetization parallel and perpendicular to the chain axis, respectively.	188
6.5	Projected spin polarized density of states of Fe chains at two interatomic distances.	189
6.6	Two-dimensional unsupported lattices of Fe. (a) square (b) triangular.	190
6.7	Magnetic anisotropy energy (MAE) (in meV per Fe atom) of simple square lattice (for two values of nearest-neighbor distances: 2.33 and 2.31 Å) with respect to the size of the two-dimensional k-point mesh.	191
6.8	Change in MAE as a function of interatomic distance for the monoatomic Fe square lattice.	192
6.9	Change in MAE and the direction of easy axis when one of the lateral sides of the square lattice is increased such that the 2D square lattice effectively becomes a 1D chain.	193

6.10	Electronic band structure of the square lattice at the lattice constant of 2.33 Å (upper panel) and 2.86 Å (lower panel). In the left column we show the scalar relativistic, spin polarized band structure. In the middle and the right columns, the band structure for the perpendicular and the in-plane (along the x axis) magnetization directions are respectively shown.	194
6.11	Projected partial spin polarized density of states of Fe square lattice at two lattice constants.	195
6.12	Magnetic anisotropy energy (MAE) (in meV per Fe atom) of triangular lattice at lattice constant $a = 2.31$ and 2.86 Å with respect to the size of the two-dimensional k -points mesh. . . .	196
6.13	(a) The Brillouin zone of a triangular lattice. (b) the scalar relativistic (first column) and the spin-orbit split electronic band structures (second and third columns) of the triangular lattice at the lattice constants of 2.31 Å (upper panel) and 2.86 Å (lower panel). The scalar relativistic bands are calculated for both the spin up and spin down channels. The spin-orbit split bands are calculated for two directions, one in-plane (along the x -axis) and the other perpendicular to the plane (along the z axis).	197
6.14	Projected spin polarized density of states of triangular Fe lattice calculated at lattice constants of 2.31 and 2.86 Å.	198
6.15	Side view of the Fe/Au(111) system. The spheres of red and yellow colors correspond respectively to Fe and Au atoms. . . .	199
6.16	MAE convergence with respect to k -points for monolayer Fe/Au(111) for case(i) (fcc stacking of Fe). The MAE value is in meV per Fe atom.	200
6.17	MAE convergence with respect to k -points for monolayer Fe/Au(111) for case(ii) (fcc stacking of Fe, hcp stacking of the topmost Au). The MAE value is in meV per Fe atom.	201
6.18	MAE convergence with respect to k -points for monolayer Fe/Au(111) for case(iii) (hcp stacking of Fe). The MAE value is in meV per Fe atom.	202

6.19	Magnetic anisotropy energy (MAE) (in meV per Fe atom) for the Fe/Au(111) for the case(i) (fcc) with the hard direction of magnetization ($90^\circ, 0^\circ$) taken as the reference energy. The dashed lines are spline fits as a guide to the eye, and should not be taken to represent mathematical functions. For example, the true maximum presumably occurs at $\theta=90^\circ$	203
6.20	Magnetic anisotropy energy (MAE) (in meV per Fe atom) for the Fe/Au(111) for the case(iii) (hcp) with the hard direction of magnetization ($\theta=90^\circ, \phi=0^\circ$) taken as the reference energy. The dashed lines are spline fits.	204

Contents

Synopsis	v
List of Abbreviations	x
1 Introduction	1
1.1 Low-dimensional Systems and Magnetism	1
1.2 Theoretical Tools for Studying Low Dimensional Systems	6
1.3 Thesis Outline	8
2 Theoretical Formalism	14
2.1 Density Functional Theory	14
2.1.1 Hohenberg-Kohn (H-K) Theorem	15
2.1.2 Kohn-Sham Treatment	18
2.1.3 Exchange-Correlation and Its Approximations	23
2.1.4 Bloch's Theorem and Plane Wave Basis Set	25
2.1.5 Pseudopotential	28
2.1.6 k-point Sampling	32
2.1.7 Smearing	33
2.1.8 Calculation of Forces	35
2.1.9 Calculation of Stress	36
2.2 Spin-Polarized Density Functional Theory	37
2.2.1 Noncollinear Magnetism	39
2.3 Relativistic DFT	41
2.3.1 Spin-Orbit Effects in Ultrasoft PP	44
2.3.2 Calculation of magnetic anisotropy	46

2.4	Code	46
3	Some Basic Concepts of Magnetism in Low Dimensions	47
3.1	Magnetism in reduced dimensions	47
3.2	Magnetic Anisotropy	49
3.2.1	Origin and Types of Magnetic Anisotropy	51
3.3	Experimental Techniques	53
3.3.1	Torque Magnetometry	53
3.3.2	Magneto-Optic Techniques	53
3.3.3	SQUID	54
3.4	Theoretical Approaches	55
4	Structural and Magnetic Properties of Two Dimensional Magnetic Surface Alloys on Rh(111)	63
4.1	Introduction	63
4.2	Bulk Alloying and Magnetism	67
4.3	Alloying at Surfaces	68
4.4	Previous Work	70
4.4.1	Clusters	70
4.4.2	Nanowires	71
4.4.3	Surfaces and Interfaces	72
4.5	Systems Studied by Us	73
4.6	Method	76
4.7	Results and Discussion	77
4.7.1	Bulk	77
4.7.2	Rh(111) Slab	78
4.7.3	Monolayers on Rh (111)	79
4.7.4	Surface Alloys	82
4.7.5	Discussion on Magnetic Behavior	112
4.8	Summary	132
5	Structural and Magnetic Anisotropy of Self-Assembled Monolayers (Methanethiolate) on Co/Au(111)	136
5.1	Introduction	136

5.2	Further Details of Previous Work	141
5.2.1	Co/Au(111)	141
5.2.2	Thiols on Co(0001) and Au(111) and Au Nanoparticles	143
5.3	Our Calculations: System	146
5.4	Our Calculations: Method	149
5.5	Results and Discussion	151
5.5.1	Pseudomorphic Co Films on (1×1) Au(111)	151
5.5.2	Co Films on ($\sqrt{3} \times \sqrt{3}$) Au(111)	158
5.5.3	Methanethiolate on Reconstructed Co/Au(111) Substrate	160
5.5.4	Magnetic Moments and Density of States	163
5.5.5	Charge Transfer	166
5.5.6	Magnetic Anisotropy Energy	167
5.6	Summary	170
6	Magnetic Anisotropy of Fe in Low Dimensions: 1D Chain, 2D Square and Triangular Lattices, Fe/Au(111)	174
6.1	Introduction	174
6.2	Previous work	176
6.2.1	One-dimensional Fe chain	177
6.2.2	Two-dimensional Fe Systems	179
6.2.3	Fe/Au system	181
6.3	Method	182
6.4	Results and Discussion	184
6.4.1	Fe Monoatomic Chain	184
6.4.2	Free Standing Square Lattice of Fe atoms	188
6.4.3	Free Standing Triangular Lattice	191
6.4.4	Fe/Au(111) System	195
6.5	Summary	202
7	Summary and Conclusions	206
	Bibliography	211

Chapter 1

Introduction

1.1 Low-dimensional Systems and Magnetism

With tremendous progress in materials design and characterization techniques, we are discovering more and more substances which exhibit novel properties that are not seen in conventional materials. Materials in low-dimensions are at the heart of current scientific and technological investigations. Low-dimensional systems refer to materials that extend in less than three dimensions. The microscopic degrees of freedom are therefore restricted from exploring the full three-dimensions. This can be realized in lattice structures resembling sheets (two-dimensional) or chains (one-dimensional), or molecules, cluster, and nanoparticles (zero-dimensional) or in thin-films or surface layers (quasi-two-dimensional). They are often called nanostructures as their short dimensions extend only up to the atomic scale (nanometer).

The magnetism of nanostructures is an exciting field of research, stimulated

by the interest in novel fundamental physics and by many potential applications. Much effort has been devoted to the investigation of the influence of the dimensionality on the magnetic properties of nanostructures. With the reduction of dimensionality, the coordination number of atoms also gets reduced, which changes the electronic environment from its bulk state. This gives rise to many novel electronic, magnetic and optical phenomena in reduced dimensions, which are not seen (or are present very weakly), in the corresponding three-dimensional system. With reduction in size, the increased surface/volume ratio makes them more susceptible to interaction effects with neighboring magnetic materials. “Nanostructuring” a material can result in the creation of new magnetic phenomena, like superparamagnetism and also can make magnetization time dependent (in conventional bulk ferromagnets, magnetization is time independent). One of the most interesting findings in the field of magnetism in low dimensions is the discovery that magnetism can be found in systems built out of materials that are not magnetic in the bulk state, such as $4d$ and $5d$ transition metals [1]. This brings about the term “nanomagnetism” which is well justified to indicate that here bulk properties may not apply at all.

Low-dimensional systems exhibit intriguing novel properties which result only because of their reduced dimensionality. For example, in the high-temperature cuprate superconductors [2], there are sheets of copper and oxygen atoms which are believed to be responsible for the superconducting effects. Sophisticated experiments have been conceived and successfully applied in nanomagnetism to deliver structural, electronic and magnetic information down to the atomic scale.

Extensive experimental and theoretical investigations of the magnetic properties of materials point towards a very intricate connection between magnetism and dimensionality. While nearly all the 30 transition metal atoms (i.e., zero-dimensional systems) possess magnetic moments, the magnetism disappears for most of them when they form their bulk state and only five of them (Cr, Mn, Fe, Co, Ni) show any macroscopic magnetic ordering at room temperature. Transition metal (TM) systems in low-dimensions are expected to exhibit intermediary behavior between the three-dimensional (bulk) and the zero-dimensional (atomic) limits. In reduced dimensions, many TM systems acquire magnetic moments either by themselves or induced by some other magnetic element. In general, in reduced dimensions the magnetism is enhanced in *3d* ferromagnetic transition metal systems and it gets induced in certain *4d* transition metal systems [3–9]. Also, many calculations have shown increased surface moments if the magnetic material is strained by growing it pseudomorphically onto a substrate [10–12].

Another important effect of reduced dimensionality on the magnetic properties is the enhancement of magnetic anisotropy energy (MAE) [13,14]. MAE is a measure of the ease of flipping the orientation of magnetization from one direction to another. It gives an estimate for the energy barrier necessary to stabilize the magnetic moments against quantum tunneling and thermal fluctuations. Therefore, a high magnetic anisotropy energy provides a more stable orientation of magnetization. The MAE is largely responsible for the spontaneous magnetic ordering (i.e., the magnetic ordering at low or zero externally applied field) in magnetic solids and nanomagnets and determines

the size and shape of magnetic domains. Magnetic anisotropy is also a prerequisite for hysteresis in ferromagnets.

From the applications viewpoint, the enhancement of magnetic moments and the anisotropy energy are the keys to the design of non-conventional high density magnetic data storage devices. Here the goal is to squeeze the largest possible amount of data onto the smallest possible area. In all magnetic storage media, the essential components include a magnetic material suspended in a nonmagnetic mixture on a suitable substrate. The magnetic material is generally a grain having thousands of magnetic atoms forming a single magnetic domain. Each grain is exchange decoupled so that the magnetization direction of individual grains can be independently controlled. In a digital magnetic storage medium, the information is stored in the form of magnetization held in one of the easy directions. The automatic flipping of magnetization between the two easy directions must be energetically forbidden in order to avoid the loss of information. Technically, this means that the material should have a high MAE. Because of the reduced dimensions, for high-temperature applications, the magnetic bits should have large values of magnetic anisotropy to resist the temperature fluctuations. The minimum value of MAE required to prevent the magnetization reversal due to thermal fluctuations is estimated to be 1.2 eV/grain [15]. Also, in order to avoid dipolar magnetic interaction (which favors in-plane magnetization) between neighboring bits, the easy axis should ideally be perpendicular to the plane [15].

As an example, a bit for an IBM hard disk using a Co-based alloy, consists of about 1900 grains with a grain size of about 20 nm with a storage density

of $0.184 \text{ Gbit cm}^{-2}$ [16]. Attempts have been directed towards reducing the physical size of the magnetic grains and to achieve the minimum number of grains per bit, so that the same amount of data can be stored in a smaller area. It would be better to achieve a storage of 1 bit per grain. The ultimate limit to this size would be a single atom, able to hold magnetization in a given direction, and at the same time magnetically isolated from other such atoms by a suitable nonmagnetic material. Recently there have been efforts to explore this possibility in single magnetic atoms of Fe embedded in a nonmagnetic matrix of CuCN [17] and very recently researchers at IBM have been successful in making a bit consisting of just 12 Fe atoms [18].

Reducing the grain size, however, must be accompanied by an enhanced magnetization density and MAE in order to push down the superparamagnetic limit: when grains are too small, thermal fluctuations can easily flip the direction of magnetization, causing permanent loss of information. $3d$ transition metals (Fe, Co and Ni) have large magnetic moments whereas high spin-orbit coupling (the microscopic origin of MAE) is found in the $4d$ and $5d$ elements (which are, however, nonmagnetic). Moreover, MAE is found to be very sensitive to the crystalline structure and symmetries. In bulk ferromagnets, the MAE is of the order of μeV whereas in lower dimensions and reduced symmetries, it is found to get enhanced by up to three orders of magnitude. Therefore, low dimensional systems consisting of $3d$, $4d$ and $5d$ elements, arranged in a way so as to exploit the sensitivity of MAE to the symmetries and coordination, are expected to offer desirable features for the magnetic data storage industry. Therefore, two dimensional magnetic films are very promising for high density magnetic data storage.

Controlling these magnetic behaviors in nanostructures is not only a prerequisite to design novel magnetic storage and logic devices but also represents a fundamental challenge.

1.2 Theoretical Tools for Studying Low Dimensional Systems

Although progress in nanotechnologies, for example nanostructure fabrication implemented by atom manipulation with scanning tunneling microscopy (STM), has opened up novel avenues for materials design, there still remains the difficulty of selecting the right material from a vast range of possibilities. The experimental preparation of a new material with desired properties is often expensive and time consuming and one is not sure that the material thus prepared, even after so much of labor and time, would meet expectations. Also, the simultaneous control over shape, size and uniformity of nanostructures presents a challenge in experimental fabrication.

The search for solutions to real-world problems constantly pushes us to expand the current state-of-the-art to go beyond available approaches and find new tools. Modern high performance computer simulation based on first-principles quantum mechanical electronic structure calculations, is the method of choice in computational material science that seeks to gain understanding of materials, and it is increasingly becoming very helpful in guiding as well as narrowing down the search range for finding the right candidates. A first-principles or *ab initio* calculation refers to a calculation which starts

from the established basic laws (e.g., Schrödinger's equation), without relying on any additional assumptions or models or their parameters. It requires only the atomic numbers of elements as input and does not need any parameters to be fit from experiments. Computer simulation is a modern theoretical approach which complements the traditional experimental and theoretical approaches. In fact, it serves as a bridge between theory and experiment. Computer simulations are inexpensive, quick, and most importantly, offer the freedom of gauging the influence of various factors, such as the presence or absence of magnetic interactions, on the properties of the material under study. For example, in one of our studies (presented later), we could actually assess the role of magnetism on the mixing of two-dimensional alloys by simply switching it (magnetism) on or off. This is one of the main advantages of doing theory over experiments— that in theory one can turn on or off different interactions to factor out their effects, which is usually not possible in experiments. In this way, one can resolve some of the experimental uncertainties.

However, often the computational costs of the expensive calculations as well as the availability of computational resources, limit the first-principles study of materials to consider only a small and simple prototype of the actual experimental system. In most of the first-principles simulation tools used currently, the calculations become increasingly difficult as the system size increases beyond ~ 1000 atoms. Nevertheless, advances in computer performance and efficient numerical algorithms are making the notion of *ab initio* design of materials more and more realistic.

Thus, the first-principles calculations have proved very useful in finding magnetic materials with novel properties. There have been many instances where the experimental investigations were guided by theoretical predictions, e.g., recently, the existence of topological insulating electronic phases in systems with a strong spin-orbit interaction was predicted by theory [19–21] and only later realized experimentally [22].

Nanomagnetism is an exciting and cutting-edge research field and holds promise for potential applications in fields such as data storage, spintronics and optoelectronic technologies. Apart from applications, one encounters new and fascinating fundamental physics in the study of nanomagnetism which presents considerable challenges to our understanding of magnetic phenomena at nanoscale. Therefore, exploration in this rich and exciting field will come with both challenges and rewards!

In this thesis, we have performed first-principles density functional theory (DFT) calculations to study the electronic and magnetic properties of various low-dimensional magnetic nanostructures. Below we give an outline of the thesis work.

1.3 Thesis Outline

We have split the thesis work into seven chapters. A brief description of the chapters is outlined as follows:

In Chapter 1 (the present chapter), we provide a general introduction and the outline of the thesis.

Chapter 2 describes the theoretical method, namely density functional theory

(DFT) in the plane-wave pseudopotential approach, which has been used in all our work. After introducing the standard Kohn-Sham approach of DFT for the nonmagnetic systems with standard approximations for the exchange-correlation, we have described the spin-polarized DFT which treats magnetic systems with collinear magnetism. We have also described non-collinear magnetism (i.e., different atoms in the system can have different orientations of spin). To study the magnetic anisotropy, the spin-orbit interaction needs to be taken into account. The inclusion of spin-orbit interaction in the calculation requires the non-collinear treatment of spin. In our approach, the spin-orbit interaction is incorporated in the pseudopotential. Since the spin-orbit interaction is a relativistic effect, one needs to use relativistic pseudopotentials. Therefore, along with the usual scalar relativistic ultrasoft pseudopotentials, we briefly describe the formalism of the fully relativistic ultrasoft pseudopotentials which have been used for the study of the magnetic anisotropy energy.

In Chapter 3, we present a brief review of some magnetic properties related to our work and describe some general concepts related to magnetism and magnetic anisotropy. We also describe some experimental and theoretical methods for the measurement and calculation of magnetic anisotropy.

The work presented in the next three chapters was motivated by an attempt to interpret and/or guide experiments.

Surface alloys composed of magnetic components are attractive candidates for many potential applications. However, many candidate systems phase segregate instead of showing atomic level mixing. We therefore attempt to

gain an understanding of the factors governing alloying at the surface, especially when the component elements are bulk immiscible. In Chapter 4, we present our study of the structural and magnetic properties of quasi-two-dimensional magnetic surface alloys of the type $M_x N_{1-x}$, where M is a magnetic element and N is a nonmagnetic element ($M=\text{Fe, Co, Ni}$; $N=\text{Pt, Au, Ag, Cd, Pb}$); and the concentration $x = 0, 0.25, 0.33, 0.5, 0.67, 0.75, 1$), on a Rh(111) substrate. The choice of elements is made keeping in mind the alloying criterion of Hume-Rothery which says (in addition to other conditions) that in the bulk, the atomic level mixing of two elements will take place if their atomic sizes differ by not more than 15%. The size mismatch between the alloying elements taken by us ranges from 13% (for Fe-Pt) to 41% (for Ni-Pb) (here we have taken half of the nearest-neighbor distance in the bulk state of the element as the "atomic size"). However, when the mixing is confined to surfaces only (resulting in the so-called surface alloys), other effects such as the structure and chemical nature of the supporting substrate, the surface stress, etc., are also expected to play a crucial role in mixing. We studied the mixing (formation energy) of these binary components on the Rh(111) substrate and assess the validity of the Hume-Rothery rule for the (quasi) two-dimensional cases. Many compositions and geometric patterns of the surface alloys are considered in order to study their mixing as well as magnetic behavior. We grouped all the patterns in two types: (i) the linear chain type [corresponding to (2×1) , (3×1) and (4×1) cells] and (ii) the mixed checkerboard type [corresponding to (2×2) and $(\sqrt{3}\times\sqrt{3})$ cells] and compared their mixing properties and magnetic moments. We find that many of the combinations of these magnetic and nonmagnetic elements

result in mixing (even though they are immiscible in the bulk) while some show no or very small mixing. Contributions to the mixing from the chemical and elastic interactions are evaluated. The change in magnetic moments of the magnetic elements due to reduced dimensionality and coordination and the effect of alloying with the nonmagnetic elements are studied. We identify candidate systems that might be suitable for experimental investigation.

In Chapter 5, we study the structural and magnetic properties of Co thin films on Au(111) as well as the effect of adsorption of methane thiolate (CH_3S) on the Co/Au(111) substrate. These calculations were motivated by an attempt to interpret recent experiments which explored the issue of whether it is possible to alter the MAE of ferromagnetic thin films by the deposition of a self-assembled monolayer of organic molecules. Thiols are organic molecules extensively used for their properties of self-assembly in monolayers over many metal surfaces and nanoparticles. Self-assembled alkanethiols on gold nanoparticles show a very intriguing phenomenon of stable ferromagnetism up to room temperature.

The Co/Au(111) system in itself is very interesting as it shows a number of interesting magnetic properties: it exhibits giant magnetoresistance (GMR), a spin reorientation transition from in-plane to out-of-plane at low thicknesses (3–5 monolayers typically) and Co films on Au(111) reconstruct to form a structure which very much resembles its bulk structure. With a clever choice of our unit cell we could simulate the reconstructed Co film on Au(111) which mimics the experimental structure rather well. We checked the stability of clean and thiol adsorbed Co/Au(111) for two stackings sequences of Co layers: fcc and hcp. We found that the hcp stacked Co gives

higher stability compared to the fcc one. In addition to the reconstructed Co/Au(111), we have also studied pseudomorphic $\text{Co}_n/\text{Au}(111)$ for $n=1$ to 5. We have studied relative stabilities and magnetic moments of $\text{Co}_n/\text{Au}(111)$ for various stackings sequences (of Co layers) for a given n .

We have calculated the magnetic anisotropy energy of the reconstructed clean Co/Au(111) and CH_3S adsorbed Co/Au(111). We considered 3 ML and 5 monolayers (ML) thick Co films on Au(111). Only the electronic (spin-orbit) contribution to the MAE is calculated while the contribution from the magnetostatic anisotropy, which can be thought as resulting from the classical magnetic dipolar interaction, is not considered in our study. We find that the out-of-plane orientation of magnetization is more stable compared to in-plane orientation, for both clean as well as thiol adsorbed Co/Au(111) substrate for both the 3 ML and 5 ML Co systems. Our finding of an out-of-plane easy axis for 3 ML Co/Au(111) film is in agreement with the experimental findings; however, we do not find an enhancement in MAE upon thiol adsorption on Co/Au(111).

Chapter 6 deals with the structural and magnetic properties (with focus on the magnetic anisotropy energy) of Fe in low dimensions: one dimensional Fe chain, two dimensional square and triangular lattices and a monolayer Fe on Au(111). The Fe/Au(111) system is one where there is some uncertainty in the literature about the nature of the MAE— whether it is in-plane, out-of-plane, or canted at an angle. The top Au layer and the Fe overlayer together are considered in four different stacking sequences, allowing these layers to occupy different combinations of fcc and hcp sites with respect to the remaining Au substrate. We compared the stability and magnetic

moments of the four stacking cases and the MAE of the three most stable configurations (out of the four) of Fe/Au(111). We have also studied the MAEs of unsupported (free-standing) one- and two-dimensional Fe systems namely the mono-atomic Fe chain (one-dimensional) and Fe in triangular and square lattices (two-dimensional). For the Fe chain, we have studied the evolution of the MAE and easy and hard axes with the interatomic distance of Fe. We have also studied this effect for the triangular and square lattices (only at a few lattice constants). The effect of the the presence of a substrate on the MAE and the easy-axis of a Fe film is studied. Based on our study we found that unlike the magnetic moments, the MAE does not depend on the coordination number in any simple way. Also, the MAE is very sensitive to small structural parameters such as site occupancies and layer stackings. This may, in part, explain the range of results obtained in experiments. Finally, in Chapter 7, we summarize our work and conclude with open questions which still remain to be answered, and the future prospects.

Chapter 2

Theoretical Formalism

2.1 Density Functional Theory

In density functional theory (DFT), the problem of a many-body interacting system is mapped on to a non-interacting single particle system. The real interactions are mapped to an effective interaction that incorporates many-body effects into a one-body term. The extraordinary concept introduced by DFT is the use of electronic density, which is a scalar quantity and a function of three (position) variables only, instead of the many-body wavefunction, which is a $3N$ -variable quantity for a N -particle system. This reformulation of the usual many-body wavefunction based quantum mechanics in terms of the density as a central parameter results in a great simplification of the problem.

2.1.1 Hohenberg-Kohn (H-K) Theorem

The problem of a many-body interacting system is dealt with in quantum mechanics by using the Schrödinger equation (SE). The non-relativistic SE for a system of N electrons moving under a static external potential $V(\mathbf{r})$ is

$$\left(-\frac{\hbar^2}{2m} \sum_i^N \nabla^2 + \sum_i^N V(\mathbf{r}_i) + \sum_{i<j}^N U(\mathbf{r}_i, \mathbf{r}_j) - E \right) \Psi(\mathbf{r}_1, \mathbf{r}_2, \dots, \mathbf{r}_N) = 0, \quad (2.1)$$

where $U(\mathbf{r}_i, \mathbf{r}_j)$ is the interaction between the i^{th} and the j^{th} electrons at positions \mathbf{r}_i and \mathbf{r}_j respectively, E is the total energy and Ψ is the N -particle wavefunction of the system. $\hbar = h/2\pi$ where h is Planck's constant and m is the mass of the free electron. The first term represents the kinetic energy, where the kinetic energy operator, ∇^2 , is the Laplacian operator, which in Cartesian coordinates is the sum of unmixed second partial derivatives:

$$\nabla^2 = \frac{\partial^2}{\partial x^2} + \frac{\partial^2}{\partial y^2} + \frac{\partial^2}{\partial z^2}.$$

In principle, all the relevant information about the system is contained in its wavefunction. In practice, however, it is hard to get Ψ since this equation is hopelessly difficult to solve owing to the presence of the many-body interaction term U . Nevertheless, methods based on the expansion of the wavefunction in Slater determinants have been devised to solve this equation (e.g., the Hartree-Fock method) but they are limited in their ability to deal with larger and more complex systems.

If the many-body wavefunction of any system is known, the charge density, $n(\mathbf{r})$, of the system can easily be calculated as

$$n(\mathbf{r}) = N \int |\Psi(\mathbf{r}, \mathbf{r}_2, \mathbf{r}_3, \dots, \mathbf{r}_N)|^2 d\mathbf{r}_2 \dots d\mathbf{r}_N. \quad (2.2)$$

Hohenberg and Kohn in 1965 [23] proved that the reverse is also true (at least for the ground state), i.e., if the ground state charge density, $n^o(\mathbf{r})$, is known, it is in principle possible to calculate the corresponding ground state wavefunction, $\Psi^o(\mathbf{r}_1, \mathbf{r}_2, \dots, \mathbf{r}_N)$.

Hohenberg and Kohn proved that the total energy of a many-body interacting system in the presence of a static external potential (e.g., that exerted by atomic nuclei in solids) is a unique functional of the electronic charge density, $n(\mathbf{r})$. The minimum of the total energy functional gives the ground state energy of the system and the corresponding $n(\mathbf{r})$ which minimizes this functional is the correct ground state charge density.

Proof

Let us consider a system of N interacting electrons under an external potential $V(\mathbf{r})$ (usually the Coulomb potential of the nuclei). Let $\hat{H} = T + U + V$ be the many-electron Hamiltonian with ground state wavefunction ψ , where T is the kinetic energy, U the electron-electron interaction and V the external potential.

Let us consider now a different Hamiltonian $\hat{H}' = T + U + V'$ (where V and V' are different potentials and do not differ simply by a constant), with ground state wavefunction Ψ' . Let us assume that the ground state charge densities are the same: $n[V] = n'[V']$. Since Ψ' is not an eigenfunction of \hat{H} , the following inequality holds:

$$E' = \langle \Psi' | \hat{H}' | \Psi' \rangle < \langle \Psi | \hat{H}' | \Psi \rangle = \langle \Psi | \hat{H} + V' - V | \Psi \rangle, \quad (2.3)$$

that is,

$$E' < E + \int (V(\mathbf{r}) - V'(\mathbf{r}))n(\mathbf{r})d\mathbf{r}, \quad (2.4)$$

By interchanging primed and unprimed quantities one finds also:

$$E < E' + \int (V'(\mathbf{r}) - V(\mathbf{r}))n(\mathbf{r})d\mathbf{r}. \quad (2.5)$$

Adding the two equations we get the absurd result: $E + E' < E + E'$. Hence by a *reductio ad absurdum* argument the assumption that two different potentials can give rise to the same charge density is wrong. So the external potential uniquely specifies the ground state charge density. The consequence of the H-K theorem is that the ground state energy E is uniquely specified by the ground state charge density. In mathematical terms E is a *functional* of $n(\mathbf{r})$, written as $E[n(\mathbf{r})]$:

$$E[n(\mathbf{r})] = \langle \Psi | T + U + V | \Psi \rangle = \langle \Psi | T + U | \Psi \rangle + \langle \Psi | V | \Psi \rangle = F[n(\mathbf{r})] + \int n(\mathbf{r})V(\mathbf{r})d\mathbf{r}, \quad (2.6)$$

where $F[n(\mathbf{r})]$ is a *universal* functional of $n(\mathbf{r})$. It is universal because it does not depend on the form of the external potential $V(\mathbf{r})$ and hence is system-independent. The ground state energy is minimized by the ground state charge density. The problem has been reduced from finding a N -body electron wavefunction to finding a three-dimensional function $n(\mathbf{r})$ which

minimizes $E[n(\mathbf{r})]$. The main hindrance confronting DFT to be used as an efficient electronic structure theory of solids lies in our ignorance of the functional $F[n(\mathbf{r})]$. This lack of the knowledge of $F[n(\mathbf{r})]$ makes DFT an approximate calculation, otherwise, the H-K minimum principle is formally exact.

2.1.2 Kohn-Sham Treatment

The H-K theorem only tells us about the existence of a functional whose minimization would yield the ground state energy and charge density. It does not give any way to obtain it. It was Kohn and Sham [24] who proposed a methodology to get this energy functional.

Kohn and Sham showed that it is possible to replace the many-electron problem by an exactly equivalent set of self-consistent one-electron equations for a system of many atoms. The total energy functional can be written as a sum of the following terms:

- (1) kinetic energy of electrons,
- (2) the interaction between ions and electrons,
- (3) the interaction among electrons,
- (4) the term containing the effects of exchange and correlation

The main difference from the Hartree theory comes in the inclusion of exchange and correlation effects.

The starting point of any theory of electronic structure of matter is the non-relativistic Schrödinger equation for the many-electron wavefunction $\Psi(\mathbf{r}_1, \mathbf{r}_2 \dots \mathbf{r}_N)$,

under the Born-Oppenheimer approximation:

$$\left\{ \frac{-\hbar^2}{2m} \sum_i \nabla_i^2 - \sum_{i,l} \frac{Z_l e^2}{|\mathbf{r}_i - \mathbf{R}_l|} + \sum_{i,j} \frac{e^2}{|\mathbf{r}_i - \mathbf{r}_j|} - E \right\} \Psi = 0. \quad (2.7)$$

The first two terms in the above equation are the kinetic energy (T) of electrons and the interaction between electrons and nuclei (the external potential). The third term represents the many-body interaction among electrons (denoted as E_{ee} for later use). In the Kohn-Sham (KS) treatment, the total energy functional can be written as:

$$E[n(\mathbf{r})] = T_s[n(\mathbf{r})] + \frac{1}{2} \int \frac{n(\mathbf{r})n(\mathbf{r}')}{|\mathbf{r} - \mathbf{r}'|} d\mathbf{r}d\mathbf{r}' + \int n(\mathbf{r})V(\mathbf{r})d\mathbf{r} + E_{xc}[n(\mathbf{r})]. \quad (2.8)$$

The first term on the right hand side of Eq. 2.8 is the KS kinetic energy (i.e., the kinetic energy of the non-interacting electron gas), the second term is the Hartree energy (E_H) containing the electrostatic interaction between electrons, the third term is the interaction of electrons with the external potential and the fourth term is the non-classical exchange-correlation interaction between electrons.

The system of interacting electrons is mapped onto a system of non-interacting electrons and for this non-interacting system the one-particle Schrödinger equation can be written as:

$$\left(-\frac{\hbar^2}{2m} \nabla^2 + V_{KS}(\mathbf{r}) - \epsilon_i \right) \psi_i(\mathbf{r}) = 0, \quad (2.9)$$

where the effective potential

$$V_{KS}(\mathbf{r}) = V(\mathbf{r}) + \int \frac{n(\mathbf{r}')}{|\mathbf{r} - \mathbf{r}'|} d\mathbf{r}' + V_{xc}[n(\mathbf{r})], \quad (2.10)$$

consisting of, besides the external potential $V(\mathbf{r})$, the Hartree potential:

$$V_H[n(\mathbf{r})] = \int \frac{n(\mathbf{r}')}{|\mathbf{r} - \mathbf{r}'|} d\mathbf{r}', \quad (2.11)$$

and the *local* exchange-correlation potential:

$$V_{xc}[n(\mathbf{r})] = \frac{\delta}{\delta n(\mathbf{r})} E_{xc}[n(\mathbf{r})]; \quad (2.12)$$

the ground state charge density, $n(\mathbf{r})$, is represented in terms of one-electron orbitals (known as KS orbitals), $\psi_i(\mathbf{r})$:

$$n(\mathbf{r}) = \sum_i^N |\psi_i(\mathbf{r})|^2. \quad (2.13)$$

The ψ_i are orthonormal:

$$\int \psi_i^*(\mathbf{r}) \psi_j(\mathbf{r}) d\mathbf{r} = \delta_{ij}, \quad (2.14)$$

where δ_{ij} is the Kronecker delta. Equations (2.9-2.13) are called the self-consistent KS equations. The problem has now been reduced to finding the solution of a Schrödinger-like equation describing a single particle moving in an effective potential $V_{KS}(\mathbf{r})$. However, this apparent simplicity comes at the cost of self-consistency: now the equation has to be solved self-consistently as the solution depends on the effective potential which depends on the density

which again depends on the solution (KS orbitals). This non-linear, self-consistency problem is solved iteratively, as shown in Fig. 2.1. The existence of a unique potential, V_{KS} , having $n^o(\mathbf{r})$ as its ground state charge density is a consequence of the H-K theorem which holds irrespective of the form of the electron-electron interaction, U . If we were to know the exact $E_{xc}[n(\mathbf{r})]$, these single-particle KS equations include all many-body effects. Thus, DFT, although derived originally from a many-particle Schrödinger equation, is finally expressed in terms of the three-dimensional density, $n(\mathbf{r})$, and the effective single-particle wavefunctions, $\psi_i(\mathbf{r})$.

The effective single-particle KS potential, V_{KS} , is a fictitious external potential which leads to the same charge density, $n^o(\mathbf{r})$, as that obtained by the real external potential for the interacting electron system. Likewise, the single-particle KS orbitals, $\psi_i(\mathbf{r})$, and the corresponding eigenenergies, ϵ_i , also do not correspond to any known physically observable quantities. However, later it was shown that the energy of the highest occupied KS orbital in fact corresponds to the ionization energy [25, 26] and it is now a common practice to compare KS eigenvalue differences to optical spectra of molecules and solids.

Once the correct (ground state) charge density is known, the total energy of the system can be calculated by adding different terms:

$$E_{tot} = \sum_i^{N/2} \epsilon_i - \frac{1}{2} \int \frac{n(\mathbf{r})n(\mathbf{r}')}{|\mathbf{r} - \mathbf{r}'|} d\mathbf{r}' d\mathbf{r} + E_{xc}[n(\mathbf{r})] - \int n(\mathbf{r})V_{xc}(\mathbf{r})d\mathbf{r} + E_{Ewald}. \quad (2.15)$$

Half of the Hartree energy (the second term on the right hand side) is subtracted because of the double counting of electrons in calculating the KS

eigenvalues. The contribution of the exchange interaction to the KS eigenvalues, i.e., $\langle \psi_i | V_{xc} | \psi_i \rangle$, is also subtracted out. The nuclear-nuclear interaction energy, E_{Ewald} , is finally added. Fig. 2.1 shows the flow chart of the iterative way of solving the KS equations. First, a trial (input) density n^{in} is obtained (usually from a combination of atomic wavefunctions and plane waves). The KS potential is then calculated using this density and the KS equation is solved for the KS orbitals. The new (output) density n^{out} is obtained from these KS orbitals. If the difference between the input and the output densities is lower than a pre-defined tolerance, self-consistency is achieved. Otherwise, this output density is used, after some mixing (defined in the function f) with the input density to speed up the convergence, for a new iteration and the whole procedure is repeated until the convergence is achieved. There exist various mixing schemes to speed up the convergence. In the calculations presented in this thesis, a modified Broyden's mixing method [31] (with some more refinements) is used.

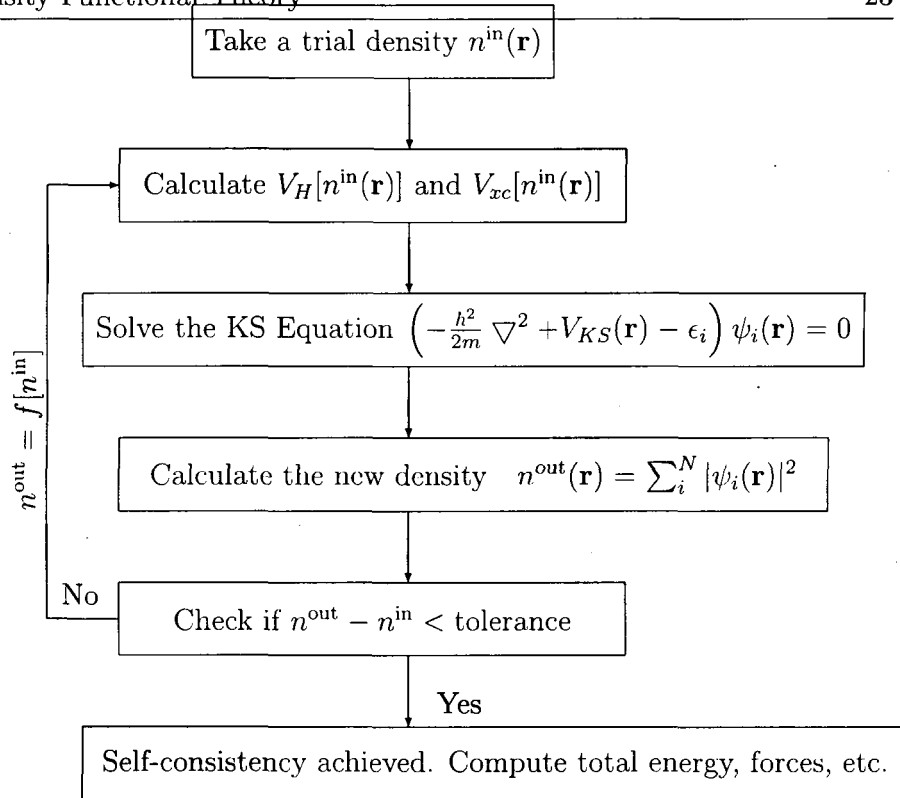


Figure 2.1: Flow chart showing the self-consistency loop for the iterative solution of the KS equation. Superscripts indicate the iteration.

2.1.3 Exchange-Correlation and Its Approximations

Exchange effects arise due to the additional degrees of freedom (spin), and the fermionic nature of electrons. The Pauli exclusion principle forbids two electrons of the same spin from occupying the same state, thus causing a sort of repulsion between them. This interaction is called the exchange interaction. A further effect of the many-body nature of the electronic system is the correlation. The electron at a point \mathbf{r} is correlated in some “mysterious” way

to electrons at other places, irrespective of their spin, to avoid each other. The correlation energy is defined as the difference between the Hartree-Fock energy (which takes only the exchange energy into account) and the exact non-relativistic energy of the system. The overall effect of the exchange and correlation is to reduce the electron density at point \mathbf{r} due to the electrons at other points. Together, the exchange and correlation energy can be defined as:

$$E_{xc}[n(\mathbf{r})] = T[n(\mathbf{r})] + E_{ee}[n(\mathbf{r})] - T_s[n(\mathbf{r})] - E_H[n(\mathbf{r})], \quad (2.16)$$

where $T[n(\mathbf{r})]$ and $E_{ee}[n(\mathbf{r})]$ are the exact kinetic and electron-electron interaction energies respectively. This is the difference between the true total energy (kinetic plus potential) and the total energy at Hartree level.

As we have seen in the previous section, the usefulness of DFT relies on the knowledge of the exchange-correlation functional, $E_{xc}[n(\mathbf{r})]$. Various approximations for this functional have been developed, which in most of the cases work well. Among them are the local density approximation (LDA) [27] and various gradient corrected generalized gradient approximations (GGAs) [28]. The simplest approximation for $E_{xc}[n(\mathbf{r})]$ is the local density approximation. In this approximation, the exchange-correlation functional is written as:

$$E_{xc}^{LDA} = \int e_{xc}^{hom}(n(\mathbf{r}))n(\mathbf{r})d\mathbf{r}, \quad (2.17)$$

where $e_{xc}^{hom}(n)$ is the exchange-correlation energy per particle of a *homogeneous* electron gas of density n .

Although the LDA is exact for a uniform electron gas and is expected to give good results only for densities varying slowly on the scale of the local

Fermi wavelength, it has been found to give remarkably good results for most of the applications. However, it is generally found to overbind, giving rise to smaller bond lengths. It is not expected to give satisfactory results for systems dominated by strong correlation effects, such as heavy fermion systems.

Improvements to the LDA are done by taking into account not only the density at \mathbf{r} but also its gradients, allowing for the nonhomogeneous charge density. These are called generalized gradient approximations (GGAs). The GGA exchange-correlation functional can be written as:

$$E_{xc}^{GGA} = \int e_{xc}^{hom}(n(\mathbf{r})) F_{xc}[n(\mathbf{r}), \nabla n(\mathbf{r})](\mathbf{r}) d\mathbf{r}, \quad (2.18)$$

where F_{xc} is called the enhancement factor. There is no unique form of the GGA and several variations exist [32–34] leading to different values for the enhancement factor.

The GGA has been found to reduce the effects of LDA overbinding; rather it usually underbinds for solid state systems. However, it has been found to give significantly better results when applied to molecules. Also, it gives better estimates of magnetic moments. In this thesis, where we have made use of the GGA, we have used the Perdew-Burke-Ernzerhof (PBE) form [33].

2.1.4 Bloch's Theorem and Plane Wave Basis Set

In any crystal there are infinitely many interacting electrons moving in the electrostatic field of ions, through the entire volume of the solid, making the problem of studying electronic motion rather difficult. But thanks to the

periodic nature of the structure of crystals, one does not need to consider the entire crystal, making the problem much easier to handle.

Since the ions in a perfect crystal are arranged in a regular periodic way, the external potential produced by these ions in which electrons move will also be periodic. If $\{\mathbf{R}\}$ be the lattice vectors of the crystal (expressing the periodicity of the crystal), the external potential felt by an electron at a position \mathbf{r} will satisfy the condition $V(\mathbf{r}) = V(\mathbf{r} + \mathbf{R})$. Bloch's theorem makes use of this periodicity of the crystal. It expresses the real space wavefunction of an electron in the infinite crystal, in terms of the wavefunctions at reciprocal space vectors in the (finite) first Brillouin zone (BZ). Though the number of reciprocal space vectors (\mathbf{k} -points) in the first BZ is still infinite, in practice one chooses some small number of representative \mathbf{k} -points using the symmetries of the crystal (see the section below on \mathbf{k} -point sampling).

Using Bloch's theorem, the electronic wavefunction at each \mathbf{k} -point in the first BZ can be expressed in terms of a Fourier series:

$$\psi_i(\mathbf{r}) = \sum_{\mathbf{G}} c_{i,\mathbf{k}+\mathbf{G}} \exp\{i(\mathbf{k} + \mathbf{G}) \cdot \mathbf{r}\}, \quad (2.19)$$

where $\{\mathbf{G}\}$ are the reciprocal lattice vectors defined by the condition $\exp(i\mathbf{G} \cdot \mathbf{R}) = 1$. Each component has a kinetic energy $(\hbar^2/2m)|\mathbf{k} + \mathbf{G}|^2$. The number of \mathbf{G} s in the above expansion decides the size of basis set, which is in principle infinite. However, the fact that the valence electrons are more important than the core electrons for the description of most of the properties of a solid, thereby making the rapidly oscillating part of the valence electron wavefunction in the core region less important than the slowly varying part in the

valence region, allows one to replace the true electronic wavefunction with a “pseudo” wavefunction (see the next section) which is smooth enough to not require high frequency components in the above Fourier expansion. Thus, one can limit the size of the basis set by setting a cutoff for the highest \mathbf{G} in terms of a quantity called the kinetic energy or plane wave cut-off, E_{cut} . For a given \mathbf{k} , the highest plane wave basis vector \mathbf{G}_c has to satisfy the relation

$$\frac{\hbar^2}{2m} |\mathbf{k} + \mathbf{G}_c|^2 = E_{cut}.$$

However, restricting the size of the basis set introduces an error in the total energy of the system, but this error can always be made arbitrarily small by setting a larger cut-off. The cut-off depends on the system and the electronic states under investigation. For example, the description of magnetism in transition metals which essentially arises from the localized d -states, requires high energy cut-off. On the other hand, s -like states which are fairly delocalized can be expressed using a much lower energy cut-off.

Another advantage of expanding the electronic wavefunctions in terms of plane waves is that in the \mathbf{k} -space representation of the KS equations, the kinetic energy becomes diagonal. Also, the size of the Hamiltonian matrix depends on the size of the basis set which can be made much smaller by using ultrasoft pseudopotentials (see the next section). The use of plane wave basis also removes the requirement of calculating the Pulay forces when calculating forces making use of the Hellmann Feynman theorem.

2.1.5 Pseudopotential

The Coulomb interaction between electrons and nuclei goes to infinity at each ionic site. Moreover, the large oscillations in the wavefunction of valence electrons in the core region also demand a large basis set, making it computationally expensive. Fortunately, most physical properties of solids are dependent on the valence electrons to a much greater degree than on the tightly bound core electrons. So the behaviour of electrons in the core region can be ignored for most of the properties of solids. Thus the true potential of electrons near the core region can be approximated by some artificially constructed potential called a “pseudopotential” (PP) [35–37] to lower the computational cost without compromising much on the accuracy of the description of physical phenomena. The pseudopotential approximation removes the core-electrons and the strong nuclear potential and replaces them with a weaker pseudopotential which acts on a set of pseudo wavefunctions rather than the true valence wavefunctions. As a result, both the number of explicitly treated electrons as well as the number of basis functions needed to describe them get drastically reduced.

In applying the PP approximation one has to define separate core and valence regions. Beyond a certain radial distance from the atom called the cutoff radius, r_c , the region is termed as the valence region, and in this region the pseudopotential and the pseudo wavefunctions are chosen to be identical with the true potential and the true wavefunction (known as all-electron wavefunction). r_c is chosen such that the last node of the all-electron wavefunction falls within it.



Although a PP is not unique, it must obey certain conditions:

First, for a continuous pseudopotential, the pseudo wavefunctions must be continuously differentiable at least twice at r_c . Second, often the total core charge produced by the pseudo wavefunctions and the all-electron wavefunctions are the same. In such a case, the PP is called a norm-conserving PP [38]. Norm-conserving PPs ensure that the pseudo-atom produces the same scattering properties as the true atom. Pseudo wavefunctions (ϕ) also have to satisfy the usual orthonormality condition: $\langle \phi_i | \phi_j \rangle = \delta_{ij}$. However, as we will see in the next section, these constraints (i.e., the orthonormality and the norm-conservation) if relaxed, can allow for an even softer PP (known as an ultrasoft PP), making the computational cost much more cheaper.

A PP is said to be transferable if it can be used to describe different chemical environments of the same atom. Norm conserving PPs automatically have transferability built into them.

The replacement of the true wavefunction by the pseudo wavefunction introduces an extra energy dependent nonlocal potential in the Hamiltonian. This can be seen from the following:

If \hat{H} , $|\chi_n\rangle$, and E_n be respectively the Hamiltonian, core eigenstates and core energy eigenvalues of an atom and $|\psi\rangle$ be a particular valence state with energy E , then one can construct a smoother pseudo wavefunction $|\phi\rangle$ defined by

$$|\psi\rangle = |\phi\rangle + \sum_n^{\text{core}} a_n |\chi_n\rangle = |\phi\rangle - \sum_n^{\text{core}} |\chi_n\rangle \langle \chi_n | \phi \rangle, \quad (2.20)$$

where in the second equation the orthogonality property of the wavefunctions has been utilized to fix the coefficients a_n . Substituting $|\psi\rangle$ in the Schrödinger

620.112 97
P12

equation $H|\psi\rangle = E|\psi\rangle$ one obtains

$$\hat{H}|\phi\rangle + \sum_n^{core} (E - E_n) |\chi_n\rangle \langle \chi_n | \phi \rangle = E|\phi\rangle, \quad (2.21)$$

so that the pseudo wavefunction obeys the Schrödinger equation with the extra potential term in the Hamiltonian given by

$$V_{NL} = \sum_n^{core} (E - E_n) |\chi_n\rangle \langle \chi_n|. \quad (2.22)$$

The effect of this energy dependent potential, which is repulsive in nature, is localized only in the core. This potential is called a nonlocal potential as it depends on the angular momentum of the states. Thus we get PPs which have two parts: (1) a local part which is energy and angular momentum independent and hence the same for all the (s, p, d, \dots) states and, (2) a nonlocal part which is energy and angular momentum dependent and thus different for different states. This nonlocal part of the PP is generally written in terms of the projectors on the angular momentum states.

Ultrasoft Pseudopotential

A further reduction in the computational cost can be achieved by introducing the so-called Vanderbilt ultrasoft PP [39]. The PP in the core region is further smoothed to make it even softer so that a smaller basis set can be used. However, now the charge density has to be augmented in the core region in order to recover the full electronic charge. The use of an ultrasoft PP requires a recasting of KS equations in terms of a generalized eigenvalue formalism

by introducing a non-local overlap operator:

$$\hat{S} = 1 + \sum_{i,j} Q_{i,j} |\beta_i\rangle \langle \beta_j|, \quad (2.23)$$

where the augmentation functions $Q_{i,j}$ are the matrix elements

$$Q_{i,j} = \langle \psi_i | \psi_j \rangle - \langle \phi_i | \phi_j \rangle, \quad (2.24)$$

and the β_i are projector functions depending upon ionic positions. In terms of this nonlocal operator, the orthonormality condition can be recast as:

$$\langle \phi_i | \hat{S} | \phi_j \rangle = \delta_{ij}. \quad (2.25)$$

This is called the generalized orthonormality condition. So, now the pseudo wavefunctions are not orthonormal and the charge inside the core region is not conserved (i.e., not equal to that obtained by the all-electron calculation). However now the advantage is that the pseudo wavefunction can be chosen to be much smoother than the norm-conserving pseudo wavefunction requiring much smaller basis size. The generalized eigenvalue problem is now rewritten in terms of the operator \hat{S} as:

$$\hat{H} \phi_{nk} = \epsilon_{nk} \hat{S} \phi_{nk}. \quad (2.26)$$

The deficit in the charge is compensated for by augmenting extra charge from outside. Since the ultrasoft PP itself is involved in solving the KS equations, changes in the charge configuration are automatically taken into account

while solving the self-consistent KS equations thus allowing the increase in r_c without having to sacrifice the transferability of the ultrasoft PP. In the present work we have used ultrasoft PPs for all the elements.

2.1.6 **k**-point Sampling

Many physical quantities, for example, total energy, density of states, etc. are obtained by integrating over all the wavevectors in the first BZ. Since the number of **k**-points in a zone is infinite and the electronic wavefunction needs to be calculated at each **k**-point, this will result in infinite computational cost even if the size of basis set is finite. So, in practice this integration over the entire first BZ is replaced by a summation at some finite number of **k**-points. These **k**-points can be chosen to lie on a uniform mesh (Monkhorst-Pack grid) [40] or can be specified specifically [41].

The **k**-point sampling approximation is given by:

$$n(\mathbf{r}) = \frac{\Omega}{(2\pi)^3} \int_{BZ} n_{\mathbf{k}}(\mathbf{r}) d\mathbf{k} \approx \sum_{\{\mathbf{k}\}} n_{\mathbf{k}}(\mathbf{r}) \omega_{\mathbf{k}} \quad (2.27)$$

where Ω is the unit cell volume, $\omega_{\mathbf{k}}$ is the weight of the **k**-point and

$$n_{\mathbf{k}}(\mathbf{r}) = \sum_i \psi_{i,\mathbf{k}}^*(\mathbf{r}) \psi_{i,\mathbf{k}}(\mathbf{r}), \quad (2.28)$$

where $\psi_{i,\mathbf{k}}(\mathbf{r})$ is the Fourier transform of $\psi_i(\mathbf{k})$. Here **k** runs over the a set of **k**-points and i labels the occupied states and the integral over the Brillouin zone is replaced by a sum over the discrete **k**-point set.

By using the symmetries of the BZ (if any), the number of **k**-points to be

sampled can further be reduced. In the Monkhorst-Pack scheme, the set of \mathbf{k} -points in the BZ is generated based on the point group symmetries. In our calculations, we use the Monkhorst-Pack grid method. The number of \mathbf{k} -points generated depends on the convergence of the quantity of interest with respect to \mathbf{k} -points. For our magnetic anisotropy energy calculations, for example, we have to use a very fine grid of \mathbf{k} -points as the energy scale in this case (meV) is of the same order as the order of the error introduced in usual \mathbf{k} -point samplings.

2.1.7 Smearing

Metals have unoccupied states near the Fermi level and several bands may cross over near the Fermi surface. Generally, for insulators, the unoccupied bands are well above the Fermi level. Since the bands are orthogonal to each other, in calculations, one needs to impose orthogonalization condition for every new band calculated. In the case of insulators, these higher lying unoccupied states need not be calculated so that the valence bands need not be orthogonalized with respect to them, and thus they are removed from the top band by the energy minimization. But in metals, due to their proximity to the occupied bands, these unoccupied bands should be included ensuring their orthogonalization with respect to the valence bands. The computational cost scales quadratically with the number of bands and one does not know beforehand which bands are important.

The total occupancy (\bar{f}_i) is the sum over the BZ of the occupancies at each \mathbf{k} -point ($f_i(\mathbf{k})$) which are either one or zero depending on whether the level

falls below or above the Fermi level (E_f):

$$\bar{f}_i = \sum_{\mathbf{k}}^{\text{IBZ}} \omega_{\mathbf{k}} f_i(\mathbf{k}) \theta_i(E_i(\mathbf{k}) - E_f), \quad (2.29)$$

$\omega_{\mathbf{k}}$ is the weight of the \mathbf{k} -point in the *irreducible* Brillouin zone (IBZ) and $\theta_i(E_i(\mathbf{k}) - E_f)$ is the step function.

For insulators and semiconductors, the density of states goes to zero smoothly before the Fermi level or the unoccupied states. For metals, the density of states does not go to zero and remains finite at the point separating the occupied and the unoccupied states. One therefore multiplies it with a sharp (step) function ensuring no contribution from the unoccupied states. However, the resolution of the step function θ at E_f (Eq. 2.29) is very difficult in plane waves. So one replaces it with a smoother function $F_i(E_i(\mathbf{k}))$ allowing partial occupancies at the E_f :

$$\bar{f}_i = \sum_{\mathbf{k}}^{\text{IBZ}} \omega_{\mathbf{k}} f_i(\mathbf{k}) F_i(E_i(\mathbf{k})). \quad (2.30)$$

Also, the discontinuous occupancies many a times lead to instabilities during minimization. At finite temperatures, the occupancies become continuous. Mermin [42] extended the idea of zero temperature DFT by smearing the bands in energy near the Fermi level using the Fermi-Dirac distribution. However, this would introduce an entropic contribution to the total energy and one would be required to minimize the free energy rather than the total energy. One can get to the zero temperature results by subtracting out the entropic part. Various techniques for smearing exist, e.g; Gaussian smearing [43], where levels near the Fermi energy are broadened by Gaussian functions,

Methfessel-Paxton smearing [44], and Marzari-Vanderbilt cold smearing [45] etc. We have used Methfessel-Paxton smearing in our calculation.

2.1.8 Calculation of Forces

Minimization of the forces acting on the atoms is necessary in order to get the relaxed equilibrium structure of a system. The important caution for calculating the forces is that the expression used for the force acting on an ion must reproduce the derivative of the expression used for the total energy with respect to the ion's position, otherwise the energy of the system will not be conserved. In this thesis, forces are calculated using the Hellmann-Feynman (H-F) theorem [46]. The force on the I^{th} ion, as in classical mechanics, is the negative of the derivative of the total energy (which is the eigenvalue of the total Hamiltonian (see Eq. 2.7), H , of the system corresponding to a fixed nuclear configuration $\{\mathbf{R}\}$) with respect to the ionic position \mathbf{R}_I , is given by:

$$\begin{aligned}
 f_I &= -\frac{\partial \langle E(\mathbf{R}) \rangle}{\partial \mathbf{R}_I} \\
 &= -\frac{\partial}{\partial \mathbf{R}_I} \langle \Psi(\mathbf{R}) | H | \Psi(\mathbf{R}) \rangle \\
 &= -\left\langle \frac{\partial \Psi}{\partial \mathbf{R}_I} | H | \Psi \right\rangle - \left\langle \Psi | \frac{\partial H}{\partial \mathbf{R}_I} | \Psi \right\rangle - \left\langle \Psi | H | \frac{\partial \Psi}{\partial \mathbf{R}_I} \right\rangle \\
 &= -E \left\{ \left\langle \frac{\partial \Psi}{\partial \mathbf{R}_I} | \Psi \right\rangle + \left\langle \Psi | \frac{\partial \Psi}{\partial \mathbf{R}_I} \right\rangle \right\} - \left\langle \Psi | \frac{\partial H}{\partial \mathbf{R}_I} | \Psi \right\rangle \\
 &= -E \frac{\partial}{\partial \mathbf{R}_I} \langle \Psi | \Psi \rangle - \left\langle \Psi | \frac{\partial H}{\partial \mathbf{R}_I} | \Psi \right\rangle \\
 &= -\left\langle \Psi | \frac{\partial H}{\partial \mathbf{R}_I} | \Psi \right\rangle.
 \end{aligned} \tag{2.31}$$

$\Psi(\mathbf{R})$ is the electronic eigenstate of the Hamiltonian H corresponding to the ionic configuration $\{\mathbf{R}\}$. The H-F theorem assumes a complete basis. The advantages of calculating the forces using the H-F theorem are that one does not need to sample total energies at many configurations and the force constant of different bonds between atoms can be easily calculated. If the basis is incomplete (which is always the case in practice), the Ψ will not be an exact eigenstate of H and the other two terms in the general expression will not vanish. The derivative of the wavefunction with respect to the atomic displacements will therefore not vanish if one uses an incomplete, position-dependent, localized basis set. This results in a finite force, called the Pulay force [47,48]. The use of a plane wave (i.e. a position-independent) basis means that one need not calculate Pulay forces. Note that the Pulay forces are zero in the limit of a complete basis set (whether localized or position-independent). However, the use of ultrasoft PP introduces similar kind of forces due to modified orthogonality constraint brought about by the localized augmentation charge [49].

2.1.9 Calculation of Stress

The stress tensor ($\sigma_{\alpha\beta}$), based on the expression derived by Nielsen and Martin [50], is the derivative of the total energy with respect to the strain tensor $\epsilon_{\alpha\beta}$, per unit volume Ω :

$$\sigma_{\alpha\beta} = -\frac{1}{\Omega} \frac{\partial E_{tot}}{\partial \epsilon_{\alpha\beta}}, \quad (2.32)$$

where α, β are Cartesian indices. Using the H-F theorem, it can be written as

$$\sigma_{\alpha\beta} = -\frac{1}{\Omega} \langle \Psi | \frac{\partial H}{\partial \epsilon_{\alpha\beta}} | \Psi \rangle. \quad (2.33)$$

The H-F theorem assumes that the basis is complete. Upon applying the strain, the basis set (i.e., the number of plane waves) changes. However, even for the incomplete basis set, the above equation holds if one can keep the basis set unchanged while calculating the derivative of the total energy with respect to the strain. This can be achieved, for isotropic strain, by changing the kinetic energy cut-off accordingly. For anisotropic strain, however, this becomes difficult and thus in practice one adopts a procedure of obtaining the stress tensor by differentiating the total energy calculated at the fixed energy cut-off in the finite difference calculation. The discontinuity introduced in the pressure-volume curves as a result of this is partially removed by introducing a smooth penalty function for the plane waves whose kinetic energy exceeds some given cut-off [51].

2.2 Spin-Polarized Density Functional Theory

So far we have considered the spin-degenerate charge density $n(\mathbf{r})$ of electrons only. Magnetism arises largely due to the polarization of electronic spins. To describe magnetism, one needs to take care of the spin-polarized charge densities. One defines, along the lines of usual (non spin-polarized) DFT,

charge densities for spin-up and spin-down electrons in terms of spin-up and spin-down Kohn-Sham orbitals $\psi_i^\uparrow(\mathbf{r})$ and $\psi_i^\downarrow(\mathbf{r})$ as:

$$n^\uparrow(\mathbf{r}) = \sum_i |\psi_i^\uparrow(\mathbf{r})|^2, \quad (2.34)$$

and

$$n^\downarrow(\mathbf{r}) = \sum_i |\psi_i^\downarrow(\mathbf{r})|^2. \quad (2.35)$$

The scalar electron density can be expressed as

$$n(\mathbf{r}) = n^\uparrow(\mathbf{r}) + n^\downarrow(\mathbf{r}), \quad (2.36)$$

and the magnetization density is

$$\mathbf{m}(\mathbf{r}) = n^\uparrow(\mathbf{r}) - n^\downarrow(\mathbf{r}). \quad (2.37)$$

These four variables ($n(\mathbf{r})$ and the three components of vector $\mathbf{m}(\mathbf{r})$) constitute the basic variables of spin-density-functional theory.

In terms of these variables, the KS equation for the spin-polarized case can be recast as,

$$\left(-\frac{\hbar^2}{2m} \nabla^2 + V_{KS}^{\uparrow\downarrow}(\mathbf{r}) - \epsilon_i^{\uparrow\downarrow} \right) \psi_i^{\uparrow\downarrow}(\mathbf{r}) = 0, \quad (2.38)$$

where the effective KS potential takes the form

$$V_{KS}^{\uparrow\downarrow}(\mathbf{r}) = V(\mathbf{r}) + \int \frac{n(\mathbf{r}')}{|\mathbf{r} - \mathbf{r}'|} d\mathbf{r}' + V_{xc}^{\uparrow\downarrow}(\mathbf{r}), \quad (2.39)$$

and the spin-dependent exchange-correlation potential $V_{xc}^{\uparrow\downarrow}(\mathbf{r})$, are now given by,

$$V_{xc}^{\uparrow\downarrow}(\mathbf{r}) = \frac{\delta}{\delta n(\mathbf{r})} E_{xc}[n(\mathbf{r}), \mathbf{m}(\mathbf{r})]. \quad (2.40)$$

Note that the external potential here includes the external magnetic fields H (if any) also, which will contribute a $\pm\mu_B H$ term, where μ_B is the Bohr magneton. The minus sign means that the majority spins (\uparrow) are energetically favoured over the minority spins (\downarrow).

Like DFT, Spin-Polarized DFT is also formally exact. Approximations enter due to the lack of knowledge of the exchange-correlation functionals E_{xc} and $V_{xc}^{\uparrow\downarrow}$ which embody all the many-body effects in the system. Magnetic versions of LDA, LSDA (local-spin-density approximation) [52–54], and GGA [33,55] have been developed and had been shown to work rather well for many applications.

2.2.1 Noncollinear Magnetism

The KS eigenfunctions for the collinear magnetic case are scalar functions. In order to describe a general state of magnetization where the spins could be oriented in any direction, one needs to introduce orthonormal bi-dimensional spinors as KS eigenfunctions:

$$\Psi_i(\mathbf{r}) = \begin{pmatrix} \psi_{i\uparrow}(\mathbf{r}) \\ \psi_{i\downarrow}(\mathbf{r}) \end{pmatrix} \quad (2.41)$$

In terms of these two-component spinors, the magnetization can be expressed as the expectation value of the Pauli matrices:

$$\mathbf{m}(\mathbf{r}) = \mu_B \sum_i^{occ} \Psi_i^\dagger(\mathbf{r}) \boldsymbol{\sigma} \Psi_i(\mathbf{r}), \quad (2.42)$$

where the sum runs over all the occupied states. The $\boldsymbol{\sigma}$ is the Pauli matrix with the three components:

$$\sigma_x = \begin{pmatrix} 0 & 1 \\ 1 & 0 \end{pmatrix}; \sigma_y = \begin{pmatrix} 0 & i \\ -i & 0 \end{pmatrix}; \sigma_z = \begin{pmatrix} 1 & 0 \\ 0 & -1 \end{pmatrix}. \quad (2.43)$$

The components of the magnetization can then be written as,

$$m_x(\mathbf{r}) = \mu_B \sum_i^{occ} \Psi_i^\dagger(\mathbf{r}) \sigma_x \Psi_i(\mathbf{r}) = \mu_B \sum_i^{occ} (\psi_{i\uparrow}^* \psi_{i\downarrow} + \psi_{i\downarrow}^* \psi_{i\uparrow}) \quad (2.44)$$

$$m_y(\mathbf{r}) = \mu_B \sum_i^{occ} \Psi_i^\dagger(\mathbf{r}) \sigma_y \Psi_i(\mathbf{r}) = i\mu_B \sum_i^{occ} (\psi_{i\uparrow}^* \psi_{i\downarrow} - \psi_{i\downarrow}^* \psi_{i\uparrow}) \quad (2.45)$$

$$m_z(\mathbf{r}) = \mu_B \sum_i^{occ} \Psi_i^\dagger(\mathbf{r}) \sigma_z \Psi_i(\mathbf{r}) = \mu_B \sum_i^{occ} (|\psi_{i\uparrow}|^2 - |\psi_{i\downarrow}|^2) \quad (2.46)$$

The charge density is the sum of the up and the down spin charge densities:

$$n(\mathbf{r}) = \sum_i^{occ} \Psi_i^\dagger(\mathbf{r}) \Psi_i(\mathbf{r}) = \sum_i^{occ} (\psi_{i\uparrow}^* \psi_{i\uparrow} + \psi_{i\downarrow}^* \psi_{i\downarrow}). \quad (2.47)$$

The noncollinear KS equation becomes:

$$(T + V_{ion} + V_H + V_{xc} + \mathbf{B}(\mathbf{r}) \cdot \boldsymbol{\sigma}) \Psi(\mathbf{r}) = \epsilon_i \Psi(\mathbf{r}) \quad (2.48)$$

where the exchange and correlation potential V_{xc} and the exchange-correlation field \mathbf{B} are defined as:

$$V_{xc} = \frac{\delta E_{xc}[n(\mathbf{r}), m(\mathbf{r})]}{\delta n(\mathbf{r})} \quad (2.49)$$

and

$$B_i = \frac{\delta E_{xc}[n(\mathbf{r}), \mathbf{m}(\mathbf{r})]}{\delta m_i(\mathbf{r})}. \quad (2.50)$$

The exchange-correlation functional contains now the full magnetization $\mathbf{m}(\mathbf{r})$ instead of the z -component $m_z(\mathbf{r})$ only. The non-collinear treatment of magnetization was employed by Kübler and co-workers [57] to study the magnetic and electronic properties of RhMn_3 and PtMn_3 . In their approximation, they fixed the direction of the magnetization of each atom but allowed the spins to have different directions. Bylander and Kleinman [58] lifted the constraints on the direction of magnetization and used instead a self-consistent non-collinear method. Our calculations of magnetic anisotropy, which require noncollinear magnetism, are based on this approach.

2.3 Relativistic DFT

In early calculations, the relativistic effects of the electron dynamics were treated in an average way. The ultrasoft PP used were generated from the non-relativistic (or the semi-relativistic) Hamiltonian. However, many physical properties of solids are the result of relativistic effects, e.g., the magnetic anisotropy (the dependence of the ease of magnetizing a magnetic sample on the directions or the orientation of the crystal). Therefore, a fully-relativistic

treatment of the electron spin is essential in some electronic structure calculations. Here we describe the theory behind the ultrasoft PP obtained from the fully-relativistic KS equation.

One of the important consequences of a relativistic treatment is the spin-orbit coupling (SOC). The effect of this coupling is to split states that are degenerate in a non-relativistic description. The electron spin gets coupled with its orbital motion making the spin dependent on the direction, giving rise to the magnetic anisotropy. The electronic states no more remain a scalar function but are described by two-component spinors. The fully relativistic treatment becomes necessary especially in low-dimensional nanomagnets as the magnetic anisotropy stabilizes the magnetism in these systems [59].

To account for the relativistic effects of electronic motion, the starting point is to use the Dirac equation. The relativistic Dirac Hamiltonian for a free electron is written as:

$$H = \beta mc^2 + c\underline{\alpha} \cdot \mathbf{p}, \quad (2.51)$$

where c is the speed of light, m is the electron mass and β and $\underline{\alpha}$ are 4×4 matrices (their forms are not unique. They are usually expressed in terms of the Pauli matrices). The solutions are expressed as four-component spinors:

$$\psi(\mathbf{r}) = \begin{pmatrix} \psi_1(\mathbf{r}) \\ \psi_2(\mathbf{r}) \\ \psi_3(\mathbf{r}) \\ \psi_4(\mathbf{r}) \end{pmatrix} = \begin{pmatrix} \psi_A(\mathbf{r}) \\ \psi_B(\mathbf{r}) \end{pmatrix}, \quad (2.52)$$

where $\psi_A(\mathbf{r})$ and $\psi_B(\mathbf{r})$ are two-component spinors. $\psi_A(\mathbf{r})$ and $\psi_B(\mathbf{r})$ are called the large and the small components respectively as the latter turns out to be of the order v/c (v being the speed of the electron and c the speed of light) of the former. In the presence of an electromagnetic field, the Dirac equation gives rise to the spin-orbit coupling term in addition to the relativistic corrections in the kinetic and the potential energies of the electron [56]. The Dirac-like equation for a system of interacting electrons in an electromagnetic field (given by the scalar and the vector potentials $\phi(\mathbf{r})$ and $\mathbf{A}(\mathbf{r})$ respectively) can be written as:

$$H = \sum_i [(\mathbf{p}_i - e\mathbf{A}(\mathbf{r}))^2 - \mu_B \boldsymbol{\sigma}_i \cdot \mathbf{B}(\mathbf{r}_i) + e\phi(\mathbf{r}_i)] + \frac{1}{2} \sum_{ij} \frac{e^2}{|\mathbf{r}_i - \mathbf{r}_j|} \quad (2.53)$$

where $\mathbf{B}(\mathbf{r}) = \nabla \times \mathbf{A}(\mathbf{r})$. We can write the external one-body potential as a 2×2 matrix:

$$V_{ext}^{\sigma, \sigma'}(\mathbf{r}) = \begin{pmatrix} e\phi(\mathbf{r}) - \mu_B B_z(\mathbf{r}) & -\mu_B(B_x(\mathbf{r}) - iB_y(\mathbf{r})) \\ -\mu_B(B_x(\mathbf{r}) + iB_y(\mathbf{r})) & e\phi(\mathbf{r}) + \mu_B B_z(\mathbf{r}) \end{pmatrix}. \quad (2.54)$$

Along the lines of the standard KS formulation, one maps this system of interacting electrons onto an auxiliary system of non-interacting electrons with spin that has the same spin-density as the original system. The basic variable of relativistic DFT is the spin-density expressed in terms of the two-component spinors ($\psi_i(\mathbf{r}, \sigma)$) one-electron wavefunctions:

$$n(\mathbf{r}, \sigma, \sigma') = \sum_i \psi_i^*(\mathbf{r}, \sigma) \psi_i(\mathbf{r}, \sigma'). \quad (2.55)$$

2.3.1 Spin-Orbit Effects in Ultrasoft PP

In a relativistic pseudopotential DFT, the relativistic effects are incorporated in the pseudopotential part of the Hamiltonian rather than treating them as a perturbation. Since the most significant relativistic effects come from the core region [60], the non-local part of the PP needs to be modified (see section 2.1.5). The spin-orbit effects have been treated in norm-conserving PPs in fully separable form [61,62] and the splitting of bands due to SOC in semiconductors like MnAs and MnSe have been reported [63]. The inclusion of SOC effects in ultrasoft PP has been accomplished only recently [64].

In the scalar relativistic or non relativistic [65] equation, the radial component of the solution depends only on the orbital angular momentum quantum number l , whereas the radial component of the fully relativistic atomic Dirac-like equation depends on l as well as on the total angular momentum quantum number j . For each value of l , there are two values of j , one corresponding to $l + 1/2$ and the other corresponding to $l - 1/2$. Thus, each l value gets split into two j values. The solutions of the scalar relativistic equation are j -averaged over the solutions of the fully relativistic equation. The ultrasoft PPs generated using the scalar or the non relativistic KS equation are thus j -averaged. They are generated by requiring that the scattering properties of the ultrasoft PP are exact at N_e values of the energy for each l . The ultrasoft PP accounting for the SOC is generated by requiring that the scattering properties of the PP are exact at N_e values of the energy for both l and j . The coefficients for the nonlocal PP form a l and j dependent matrix $E_{l,j}$ of dimension $N_e \times N_e$. If the PP is generated using the solutions

(large components) of the radial Dirac equation, one obtains the projectors, $\beta_{l,j}$, and PP coefficients, $E_{l,j}$, for each value of l and j . The nonlocal part of the PP is written in terms of the projector functions onto the states of total angular momentum about each atom:

$$V_{NL}^{\sigma,\sigma'} = \sum_I \sum_{l,j,m_j} E_{l,j}^I |\beta_{l,j}^I Y_{l,1/2}^{I,j,m_j}\rangle \langle \beta_{l,j}^I Y_{l,1/2}^{I,j,m_j}| \quad (2.56)$$

The $Y_{l,1/2}^{j,m_j}$ are 2×1 spin angle functions, which are the eigenfunctions of the total angular momentum, defined in terms of spherical harmonics:

$$Y_{l,1/2}^{j,m_j} = \begin{pmatrix} \left(\frac{l+m_j+1/2}{2l+1}\right)^{1/2} Y_{l,m_j-1/2} \\ \left(\frac{l-m_j+1/2}{2l+1}\right)^{1/2} Y_{l,m_j+1/2} \end{pmatrix}, Y_{l,1/2}^{j,m_j} = \begin{pmatrix} \left(\frac{l-m_j+1/2}{2l+1}\right)^{1/2} Y_{l,m_j-1/2} \\ -\left(\frac{l+m_j+1/2}{2l+1}\right)^{1/2} Y_{l,m_j+1/2} \end{pmatrix}, \quad (2.57)$$

for $j = l + 1/2$ and $j = l - 1/2$ respectively. Introducing unitary transformations of the spherical harmonics and the Clebsch-Gordan coefficients we can write each component of the spin angle function as:

$$Y_{l,1/2}^{j,m_j,\sigma} = \alpha_{m_j}^{\sigma,l,j} \sum_{m'=-l}^l U_{m_j,m'}^{\sigma,l,j} Y_{l,m'} \quad (2.58)$$

and the nonlocal PP becomes:

$$V_{NL}^{\sigma,\sigma'} = \sum_I \sum_{l,j,m,m'} E_{l,j,m,m'}^{I,\sigma,\sigma'} |\beta_{l,j}^I Y_{l,m}^I\rangle \langle \beta_{l,j}^I Y_{l,m'}^I|. \quad (2.59)$$

The coefficients become spin-dependent:

$$E_{l,j,m,m'}^{I,\sigma,\sigma'} = E_{l,j}^I \sum_{m_j=-j}^j \alpha_{m_j}^{\sigma,l,j} U_{m_j,m}^{\sigma,l,j} \alpha_{m_j}^{\sigma',l,j} U_{m_j,m'}^{*\sigma',l,j}. \quad (2.60)$$

This is similar in form to what one had in the scalar-relativistic treatment so that it can be applied to each component of the spin separately.

2.3.2 Calculation of magnetic anisotropy

The magnetic anisotropy energy (MAE) is estimated by calculating the total energy from a fully-relativistic PP calculation for different fixed directions of the total magnetization and taking the difference of the highest and the lowest total energy (corresponding to the “easy” and the “hard” directions). This method of taking MAE as the difference between the *total* energies instead of the difference between the *band* energies calculated from the scalar-relativistic all-electron calculations with and without account of the SO coupling, is better in that it takes into account the exchange-correlation contributions to the MAE [66]. This is discussed in greater detail in the next chapter.

2.4 Code

Our calculations are performed using PWscf codes of Quantum ESPRESSO distribution [67]. This is a freely downloadable open-source software package.

Chapter 3

Some Basic Concepts of Magnetism in Low Dimensions

3.1 Magnetism in reduced dimensions

The magnetic properties of systems in reduced dimensions and altered symmetries show a remarkable difference from their bulk behavior. In general, it is found that the magnetic moments of $3d$ transition metals (TMs) in reduced dimensions are enhanced compared to their bulk values. TM systems of the $4d$ and $5d$ series, which are nonmagnetic in their bulk state, can get magnetism induced in them when they are subjected to reduced dimensions. This enhancement is generally attributed to the increase in the electronic density of states (DOS) near the Fermi level due to the narrowing of d -bands as a result of the reduction of the coordination number in reduced dimensions. There has been a lot of theoretical and experimental work on the TMs and their alloys in reduced dimensions, e.g., surfaces, thin films (monolayers as

well as multilayers) on a variety of substrates, clusters and one-dimensional nanowires. The magnetic properties of these systems seem to display intriguing behavior depending upon the size, and/or the type of constituent materials.

Stoner criterion: Before going on to survey magnetism in reduced dimension, we must mention an important model which attempts to explain this behavior. The Stoner model [68] assumes the existence of rigid electronic bands of spin-up and spin-down electrons. Initially, if the up and the down bands are symmetric with respect to energy (i.e., there is no net magnetization), the system would acquire a spontaneous magnetization by shifting the up and down bands relative to each other, if the gain in the magnetic exchange energy due to the shifting is larger than the energy cost due to the band shifting towards the higher energy. Based on the rigid-band model, the Stoner criterion for the onset of the instability of the paramagnetic phase to the ferromagnetic phase states that ferromagnetism is favoured when the product of the paramagnetic density of states at the Fermi level, $DOS(E_f)$, and the Stoner exchange parameter, I , exceeds unity, i.e., $I \text{ DOS}(E_f) > 1$. The exchange parameter I is almost independent of the atomic environment or the magnetic configuration [69] and its value turns out to be about 1 eV. Thus, systems which have higher (non-spin-polarized) electronic density of states near the Fermi level are more likely to be ferromagnetic. In the case of elemental bulk ferromagnets (Fe, Co and Ni), the Stoner criterion is roughly verified. However, many systems are found to be not following this rigid-band model e.g., antiferromagnets, TM impurities in hosts like Pd, and certain TM compounds [70].

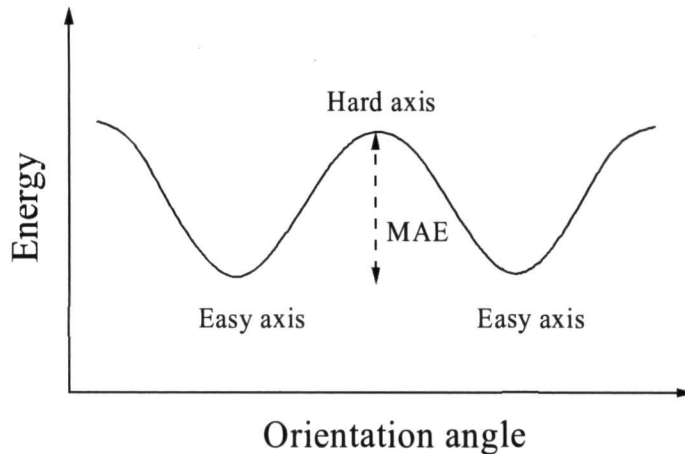
Reduction of coordination: With a reduction in dimensionality, the coordination number also usually decreases. In the bulk, the equilibrium distances between atoms are established by the minimization of the potential due to the neighboring atoms. As we know, when a solid is formed by bringing atoms closer, the electronic energy levels of isolated atoms get broadened, forming energy bands. The greater the coordination of an atom, the greater the broadening of the energy level. When the number of (nearest) neighbours is reduced, even though the remaining atoms move closer to adjust to the new charge density environment, the band broadening gets also reduced. With the narrowing of the bands, the DOS increases and there is a possibility of increasing the DOS at E_f . This, following the Stoner argument, may result in the emergence of ferromagnetism. In fact, there have been innumerable instances where the reduction of the coordination had been found to result either in the enhancement of ferromagnetism or in induced ferromagnetism (where the original system was nonmagnetic).

3.2 Magnetic Anisotropy

Another important effect of reduced dimensionality on the magnetic properties is the enhancement of magnetic anisotropy energy (MAE) [13, 14]. The MAE is a measure of the ease of flipping the orientation of magnetization from one direction to another, and it is found to be very sensitive to the crystalline structure and symmetries.

For most crystalline magnetic solids, there are some preferred directions of magnetization known as “easy axes” which often coincide with one of the high

Figure 3.1: *The energy of a typical magnetic system as a function of the orientation of magnetization. The easy axis, the hard axis and the magnetic anisotropy energy (MAE) are shown.*



symmetry crystallographic directions. The two opposite directions along an easy axis are usually equivalent, and the actual direction of magnetization can be either of them. For example, the direction of easy axis for the $3d$ bulk ferromagnetic solids [71], Fe, Co and Ni, are respectively, $[100]$, $[0001]$ and $[111]$. In general, between two easy axes there lies an energetically disfavored direction of magnetization called the “hard axis”. The difference between the energies corresponding to the magnetization along the easy axis and the hard axis is termed the magnetic anisotropy energy (MAE) (see Fig. 3.1). A high magnetic anisotropy leads to a stable alignment of magnetic moments. The MAE is largely responsible for the spontaneous magnetic ordering (i.e., the magnetic ordering at low or zero externally applied field) in magnetic solids and nanomagnets and determines the size and shape of magnetic domains. Magnetic anisotropy is a prerequisite for hysteresis in ferromagnets.

3.2.1 Origin and Types of Magnetic Anisotropy

The dominant contribution to the magnetic moment comes from the spin (moment) of the electrons. For an isolated atom, there is no anisotropy or preferred direction for the spin moments as the electron spin by itself has spherical symmetry. When two atoms are brought together, forming a molecule or dimer, the line joining the two atoms (intermolecular axis) provides a natural reference direction for the binding of (otherwise directionless) atomic orbitals. Through the atomic SOC, spins get tied to the orbitals, giving rise to a preferred direction for the magnetic moments.

The two main contributions to the MAE come from the SOC and the magnetic dipolar interactions. The former gives rise to magnetocrystalline and magnetoelastic anisotropy; the latter is responsible for shape anisotropy. The dipolar interaction is a classical magnetostatic interaction between two magnetic dipoles (having magnetic moments \mathbf{m}_1 and \mathbf{m}_2) kept at a distance \mathbf{r} :

$$H_{dip} = \frac{\mu_0}{4\pi} \left[\frac{\mathbf{m}_1 \cdot \mathbf{m}_2}{r^3} - 3 \frac{(\mathbf{m}_1 \cdot \mathbf{r})(\mathbf{m}_2 \cdot \mathbf{r})}{r^5} \right]. \quad (3.1)$$

The dipolar term depends on the macroscopic shape of the sample and for thin films, always favors an in-plane magnetization. However, its contribution is small and can usually be neglected as we are interested in the effects that are of microscopic origin.

The magnetocrystalline anisotropy, resulting from the interaction of the spin magnetic moment with the crystal lattice (spin-orbit interaction), is an intrinsic property of the magnetic material and is independent of the grain size and shape. The easy and hard directions thus arise from the SOC.

There is no simple rule available to predict the magnitude or the direction of magnetic anisotropy arising from SOC. The SOC plays a significant role in the electronic structure of both magnetic and nonmagnetic systems. It has been now realized that the SOC also plays an important role in systems with reduced coordination and dimensionality [72–75, 77]. In fact, the dipolar and the spin-orbit interactions are necessary to explain the very existence of ferromagnetism in low-dimensional systems as the Mermin-Wagner theorem predicts that at any finite temperature, ferromagnetism can not exist in two-dimensional (2D) systems with only short-range, isotropic exchange interactions. The SOC plays an important role not only for magnetic properties but also for nonmagnetic electronic structure: e.g., it has been shown to be important in the splitting of Au(111) surface states [74, 75] and in getting the correct equilibrium geometry of Pt nanoclusters [72].

Another anisotropy resulting from the SOC is the magnetostriction—the magnetic anisotropy caused by the strain. Due to magnetostriction, a magnetic material changes its dimension upon magnetization. The inverse effect, i.e., the change in magnetization upon stress application, also occurs. The magnetic anisotropy constants quantifying the various anisotropy energies are temperature dependent. In general they decrease with temperature and vanish at the Curie temperature.

The study of low dimensional systems has been made possible due to the development of highly sophisticated experimental techniques such as scanning tunneling microscopy (STM) and the rapid advancement in the computer processor technology, alongside the development and implementation of density functional theory (DFT) (described in the previous chapter) based

efficient numerical algorithms. In the following we briefly describe some experimental techniques and give a brief review of the theoretical approaches used.

3.3 Experimental Techniques

Below we outline some of the main experimental techniques for the measurement of MAE.

3.3.1 Torque Magnetometry

Torque magnetometry is a method for the characterization of macroscopic magnetic substances in single-crystal form. It measures the mechanical torque τ experienced by a magnetic sample in a homogeneous external magnetic field \mathbf{B} : $\tau = \mathbf{M} \times \mathbf{B}$, where \mathbf{M} is the bulk magnetization. The magnetic torque arises from the noncollinearity between the applied magnetic field and the magnetization of the sample. In an external magnetic field, the sample would experience a torque which will vanish when the field is parallel to the equilibrium magnetization directions (easy axes). This torque acts on a very fine torsion fiber by which the sample is suspended, resulting in a tiny rotation of the sample about the suspension axis. The rotation can be detected optically or electrically.

3.3.2 Magneto-Optic Techniques

Magnetic measurements exploiting magneto-optic effects rely on the change in the state of polarization of linearly polarized light upon interaction with

the magnetization of a sample. The magneto-optic Kerr effect (MOKE) which uses the change in the ellipticity and the (Kerr) rotation angle of the polarization depending on the relative orientation of the magnetization and the polarization axis, can be used to measure a certain component of magnetization for a specific arrangement. Using different arrangements of incident light and magnetizing fields relative to the sample (usually thin films), the in-plane and perpendicular components of magnetization are measured. There are basically three different arrangements in which measurements can be done: (1) the polar Kerr effect which measures the perpendicular component of magnetization of the film; (2) the longitudinal Kerr effect which measures the in-plane component of magnetization parallel to the plane of incidence; and (3) the transverse Kerr effect which measures the in-plane component perpendicular to the plane of incidence. Although MOKE does not allow for a quantitative measurement of the absolute value of the magnetization, it is one of the most useful techniques to measure magnetic anisotropies. When the photon energy is in the (soft) X-ray range and circularly polarized light is used, we have X-ray circular magnetic dichroism (XMCD) [76]. XMCD offers element-specific measurement of the magnetic moment by tuning the photon energy to a core-level absorption edge.

3.3.3 SQUID

Another method of determining the MAE is using superconducting quantum interference devices (SQUIDs) which have a very high sensitivity to detect very minute magnetic fields (as small as 10^{-14} Tesla). SQUIDs are considered

to be the world's most sensitive detectors of magnetic signals. It consists of two superconductors separated by thin insulating layers to form two parallel Josephson junctions that are used for the detection of the magnetic flux. The sample oscillates with a vibration frequency of 0.1 – 5 Hz, causing a change of magnetic flux in superconducting detector coils called the pick-up coils. The device is operated in a constant-flux mode using a feedback circuitry. The flux change is converted into a current signal through an amplifier which is fed to the feedback coil such that this flux change is exactly compensated. The output signal is proportional to this compensating current. The sensitivity of the SQUID depends largely on the geometry and position of the pick-up coils. The magnetic anisotropy can be measured by taking measurements at various angles.

3.4 Theoretical Approaches

The earliest attempts to get a quantitative estimation of MAE (of bulk crystals) were based on macroscopic phenomenological models employing thermodynamic free energy with magnetization and its direction (with respect to the crystalline axes) as thermodynamic variables:

$$F(\mathbf{M}) = F_0 + K_1 F_1(\alpha_1^{h_1}, \alpha_2^{k_1}, \alpha_3^{l_1}) + K_2 F_2(\alpha_1^{h_2}, \alpha_2^{k_2}, \alpha_3^{l_3}) + \dots \quad (3.2)$$

where $(\alpha_1, \alpha_2, \alpha_3) = (\sin \theta \cos \phi, \sin \theta \sin \phi, \cos \theta)$ are the direction cosines

of the magnetization \mathbf{M} with respect to the crystal axes; h_i , k_i and l_i are integers and depend on the symmetry of the crystal lattice; K_i are the anisotropy coefficients which generally depend on the temperature and other variables and may also depend on the magnitude of the magnetization. Exploiting the crystalline symmetries [78,79], the functional form of F can be deduced. The anisotropy coefficients can be determined from the experimental magnetization (torque) curves. This model helped in understanding the effect of symmetries and it was shown that a lowering of the symmetry results in an increase of the anisotropy energy. For example, the anisotropy of bulk Co, which has a lower (hexagonal) symmetry, is one order of magnitude larger than that of Fe and Ni, which have a higher (cubic) symmetry.

From 1930, people started approaching this problem from the quantum mechanical electronic structure point of view (see the review by van Vleck [80]). The Heisenberg exchange interaction, which accounts so well for the magnetic states of a system, is of no use in explaining the magnetic anisotropy, since it does not depend on the absolute orientation of spins relative to the crystal lattice. The magnetic dipolar interactions between the spins were proposed but this was not able to account for the observed anisotropy for the cubic bulk ferromagnets, because in the cubic symmetry, the contribution from all the nearest-neighbors add to zero. Bloch and Gentile [81] and van Vleck [80] advanced the idea that the magnetic anisotropy results from the interplay between the spin and orbital moments through spin-orbit coupling. It has now been established that the magnetic anisotropy is primarily due to the simultaneous occurrence of relativity (spin-orbit coupling) and magnetism. Therefore, a detailed understanding of it would in-principle require a study

of relativistic many-electron systems.

The elucidation of the magnitude, sign, temperature and alloy composition dependence of the anisotropy coefficients were first attempted within the itinerant-electron model of metals by Brooks [82] in 1940. For small systems of molecules such as single molecule magnets (SMM), the quantum mechanical calculation of the magnetic anisotropy is routinely done in the exchange Hamiltonian model in which the exchange interaction between the magnetic centers (in the molecule) is taken as the unperturbed Hamiltonian and the SOC is treated as a perturbation. Neglecting the inter-site dipolar interactions and assuming the other interactions responsible for the anisotropy to be short ranged, only the intra-center (on-site) contributions are considered [83]. As we have seen, the microscopic origin of MAE comes from two main interactions: (1) the dipolar and (2) the spin-orbit. The different theoretical approaches attempting to calculate the MAE from a microscopic consideration essentially differ in taking different approximations, at different levels of sophistication, for these interactions. Generally, the dipolar interaction is treated at the classical level and the SOC is treated either as a perturbation to the nonrelativistic Hamiltonian, or fully relativistically. As the MAE is much smaller compared to other electronic energies, its accurate prediction becomes very sensitive to the subtle details of the Fermi surface. Therefore, high numerical accuracy and a tighter convergence criterion are very necessary, making the computational requirements of first-principles calculations very demanding.

Structural and magnetic changes take place due to intricate electronic interactions at the atomic scale. Pair-potential or semiempirical potential methods cannot be used as these are either insensitive to change in coordination or do not capture these changes very well, which often involve very small energy differences (of the order of meV).

The state of the art density functional theory is currently one of the best theories to describe a vast number of structural and magnetic properties at the electronic level. It is a powerful tool which can do *ab initio* calculations, i.e., it does not require any empirical input parameter other than the atomic number of the elements. However, being able to describe these intricate quantum mechanical electronic interactions accurately, it is limited to being able to deal with systems with a small number of atoms (typically 100 to 1000), as the computing cost typically scales as the third power of the system size.

Magnetic anisotropy being a ground state property, is in principle accessible by DFT. Since the SOC is a relativistic effect, the calculation of magnetic anisotropy for extended systems requires a relativistic treatment of electron dynamics, which is not explicitly described within the standard Kohn-Sham DFT (as it is a non-relativistic treatment). However, the relativistic generalization of density functional theory has been carried out in the framework of quantum electrodynamics [84, 85], and the resulting equations are one-particle four-component Dirac-like equations with the self-consistent potential.

Spin-orbit effects in all-electron DFT calculations have been included, e.g., the Korringa-Kohn-Rostoker (KKR) method [86, 87] or the linear muffin-tin

orbital method with the atomic-sphere approximation (LMTO-ASA) [88]. These calculations often involve some shape approximations for the potential. However, due to all-electron nature and the approximation for the potential, the efficiency of these calculations are limited.

The first-principles calculations of MAE are expensive due to the small energy scale. For bulk ferromagnetic materials, the typical MAE values are very small, of the order of $10^{-5} - 10^{-6}$ eV per atom, which makes its calculation very difficult, since it is at the limit of accuracy of electronic structure methods [89]. Various high-quality calculations of MAE employing the local spin-density approximation (LSDA) on ferromagnetic bulk metals (Fe, Co and Ni) have not yielded good results: for Fe, the computed values differ from experiment by a factor of about 2, the result for hcp Co is far worse, and for Ni, even the direction of easy axis is not correct. By adding explicitly the orbital polarization [82] which is underestimated by LSDA, the LSDA predicted MAEs and orbital moments can be improved for Fe and Co [89]. However for Ni, the predicted easy axis was still wrong [89], which only could be calculated correctly with a LDA + U method, at some particular value of U [90]. The total energies per atom, however, are of the order of 10^2 eV making the MAE a very small fraction of the former. Since the MAE is the *difference* of total energies between two different (non-equivalent) directions of magnetization, therefore, in order to see the contribution of the MAE, the total energies need to be calculated with extremely high numerical accuracy. The MAE of the low-dimensional system such as thin films and one-dimensional wires are of the order of meV and thus can be calculated with a greater precision compared to the bulk systems.

One possible approach assumes that most of the contributions to the total energy are not affected by changing the direction of magnetization, then the total energy differences are approximated, using the force theorem, by the differences between the sum of band energies calculated non self-consistently with the SOC included. This approach is employed in many all-electron calculations such as KKR, full potential linearized augmented plane wave (FLAPW) and linear muffin-tin orbital (LMTO) methods, mentioned above. It should be noted that this assumption neglects the changes in the exchange and correlation energies upon changing the magnetization direction.

Alternatively, instead of using the fully relativistic Hamiltonian or the all-electron methods, one can include relativistic effects up to order α^2 (where α is the fine structure constant) by using the pseudopotentials generated from the atomic Dirac equation in the nonrelativistic Kohn-Sham equations for two-component spinors [91]. The state of the art planewave pseudopotential DFT is one of the most efficient methods for electronic and magnetic structure calculations. The SOC in the norm-conserving pseudopotential [91] had already been included. The recent inclusion of SOC in the ultrasoft pseudopotential scheme now enables one to calculate relativistic effects while benefitting from the computational cost-effectiveness of ultrasoft pseudopotentials [64].

In this thesis we employ noncollinear spin-polarized density functional theory in which the spin-orbit interactions are described by fully relativistic ultrasoft pseudopotentials to calculate the MAE. Instead of taking the MAE as the difference between the sum of band energies, we take the difference between the total energies which takes into account the changes in the exchange

and correlation and the Hartree energies upon the change in the magnetization direction. Thus we do fully self-consistent total energy calculations in different directions of magnetization.

In principle, the energy minimization in noncollinear spin-polarized DFT calculations will ensure that a system, initially with magnetization in a generic direction, will end up in its ground state with the magnetization along the easy axis. This, however, involves two different energy scales: the energy scale corresponding to the change in the magnitude of individual magnetic moments, which is of the order of 0.1 eV, and the energy scale corresponding to the change in the direction of magnetization which is of the order of 1.0 meV. Consequently, the energy convergence due to the latter becomes very slow. However, instead of obtaining the magnetic ground state by performing a time consuming self-consistent field (scf) calculation, one can do a set of different scf calculations, each with the initial total magnetization kept fixed in different directions. One thus samples the total energy landscape as a function of magnetization direction and the difference between the minimum (corresponding to the easy axis) and the maximum (corresponding to the hard axis) of these energies corresponds to the MAE.

In our scheme of planewave pseudopotential DFT, the calculation of MAE consists of obtaining the total energies of the system as a function of fixed directions of magnetization and the difference in the minimum and the maximum of these energies is taken as the MAE. Because of the small energy scale of the MAE, the convergence of the MAE with respect to the planewave cutoff and the k-space integration must be carefully tested as the error due to insufficient k-space sampling and planewave cutoff is of the same order as the

typical values of MAE.

We have performed *ab initio* total energy DFT calculations to get the MAE for our systems. We have done MAE calculations for the low dimensional Fe systems (free standing Fe-chain, two-dimensional square and triangular lattices) and a monolayer Fe deposited on an Au(111) substrate. We have also done MAE calculations on another system consisting of clean Co/Au(111) and methancthiol adsorbed on Co/Au(111).

Chapter 4

Structural and Magnetic

Properties of Two Dimensional

Magnetic Surface Alloys on

Rh(111)

4.1 Introduction

Over the last two decades, tremendous progress has been made in the synthesis and characterization of materials with novel electronic and magnetic properties. This has partly been driven by the emergence of unique and fascinating properties at the nanoscale which find unconventional applications in nanoscale devices, outperforming conventional devices. In general, structural and magnetic properties at the nanoscale, which is characterized by a reduced dimensionality and coordination, are greatly altered from their

three-dimensional bulk values. Although the discovery of magnetic phenomena at the atomic scale dates back to the early decades of the last century, in recent years our knowledge of magnetic phenomena in the solid state has improved. This can be attributed to our ability to synthesize, as well as to do first-principles calculations on, low dimensional nanostructures of these materials. Experimental as well as theoretical studies on nanoscale systems with reduced dimensionality have contributed a lot to our understanding of magnetic phenomena at this length scale.

Among the systems in reduced dimensions, two-dimensional films are particularly important from the technological point of view. Two-dimensional films consisting of one magnetic and one nonmagnetic element are very promising candidate for high density magnetic data storage [92–98].

Besides being of interest for their technological applications, they are also important from the basic physics point of view. The mechanism of magnetic interactions at the nanoscale presents a considerable challenge to our understanding of these phenomena. It has now been established after nearly two decades of experimental and theoretical investigations that magnetism at surfaces and interfaces is drastically altered compared to the bulk, and that materials that are nonmagnetic in their bulk can pick up considerable magnetism in reduced dimensions.

It is well known that the local environment of transition-metal atoms can strongly affect their magnetic behavior [99]. In general, reduced coordination enhances magnetism in $3d$ ferromagnetic transition metal systems and induces magnetism in certain $4d$ transition metal systems [3–9]. Many calculations have shown increased surface moments, as well as enhanced values

if the magnetic material is strained by growing it pseudomorphically onto a substrate [10–12]. Interestingly, reduced dimensionality does not always lead to enhanced magnetism, there can also be a drastic reduction in the magnetism as exemplified in the so-called magnetic “dead” layers of ferromagnetic films [100, 101].

$4d$ metals such as Rh, Ru and Pd when used as a substrate for a magnetic thin film are of particular interest as they have a lower d -band width compared to the $5d$ metals such as Pt. A low band width makes them more susceptible to the onset of magnetism. Induced moments on a Rh substrate having magnetic layers deposited on it have shown varying behavior: induced moments limited only to the interface Rh layer for multilayers of Fe/Rh(001) and Co/Rh(001) [102, 103], while a long-range oscillatory induced magnetization of Rh layers was found for monolayers of Fe/Rh(111) and Co/Rh(111) [104, 105]; while Fe and Co monolayer films on Rh(111) have experimentally been observed to exhibit ferromagnetic order [15]. Rh, apart from being highly polarizable, possesses a high spin-orbit coupling constant which is desirable for magnetic storage applications as it might give rise to a large magnetic anisotropy.

While the magnetism of ferromagnetic layers on Rh(111) has been studied [15], hitherto less attention has been paid to the magnetism of $3d$ ferromagnetic elements alloyed with other nonmagnetic transition metals (TMs) on Rh(111). The understanding of the magnetic behavior of these ferromagnetic elements when alloyed with nonmagnetic TMs in reduced dimensions will be of particular importance as it manifests the effect of (surface) alloying

as well as the reduction of dimensionality together. In particular, the phenomenon of surface-confined alloying, when two or more metals are allowed to mix on the surface of a substrate, has been discovered [106, 107], opening up new possibilities for materials design and engineering.

Alloy formation at surfaces differs in many ways from that in the bulk. Some combinations of metals which are immiscible in the bulk have been found to form alloys when mixing is confined to surfaces [3, 108]. The tendency of surfaces to minimize their surface energy is responsible for the observation of many unique surface structures. Surface alloying is governed by differences in the surface energy of the components, and also by the surface stress which couples with the size mismatch between the alloy components. The presence of magnetism has also been recently found to play a crucial role in surface-alloying [109]. The kinetics of surface alloy formation is also very different from that of the bulk situation, due in part to a much faster diffusion at the surface. Furthermore, surface alloying processes are more easily accessible to microscopy, making them an ideal subject for combined experimental and theoretical investigations. The combined effects of reduced dimensionality, reduced coordination, adsorbate-substrate coupling and surface alloying can lead to intriguing outcomes, and there seems to be a very complex interplay between the structure, dimensionality and magnetism where a clearcut picture is still lacking.

In the present work, we study the electronic and magnetic properties of various two-dimensional binary magnetic alloys on a Rh(111) substrate. The majority of binary combinations we consider are immiscible in their bulk

phase. These low-dimensional systems combine the complications of structure, magnetism and alloying. In the next sections we outline some of the concepts pertaining to the alloying and magnetism both in the bulk and reduced dimensions, make a survey of the literature and present and discuss our results.

4.2 Bulk Alloying and Magnetism

Alloys are atomic-level mixtures (solid solutions) of two or more metals (sometimes a small concentration of nonmetals also) mixed in definite proportions. The enhancement in the mechanical properties of pure metals brought about by the suitable mixing of two or more different metals has been known since ancient times. However, one is left only with limited choices of materials as not all pairs of metals mix with each other. The laws explaining the limited atomic level mixing of metals were first formulated by Hume-Rothery in the form of a set of empirical rules [110]. The first of these rules states that if the atomic-size mismatch between the two metals is greater than 15%, they will not form a substitutional binary alloy. For example, in equilibrium, Co and Ag are almost insoluble in each other in the solid state [111] as this system does not meet the Hume-Rothery criterion: Co and Ag have a large atomic size difference. Another factor affecting the miscibility in this system is the large difference in the surface free energy of Co and Ag.

The bulk alloying between magnetic metals has been an extensive area of scientific as well as technological research. It was observed that the average magnetization per atom as function of the number of valence electrons of

3d substitutional ferromagnetic alloys falls on a curve known as the Slater-Pauling curve [112]. This curve consists of two straight lines of opposite gradients, classifying most of the alloys in two classes: one whose average magnetization versus electron number falls on the line with the positive slope, and another whose average magnetization falls on the negative slope line.

4.3 Alloying at Surfaces

In bulk alloys, generally, the concentration of the constituent metals remains the same throughout the bulk. However, the concentration at and near the surfaces may differ from that in the bulk. Sometimes, one of the constituent elements of the alloy may get altogether segregated from the other constituents at the surface – a phenomenon called surface segregation. Thus the properties of the surface of an alloy may differ from that of the alloy itself. This finds many applications in industry, and the study of alloy surfaces is an active area of research. Different from alloy surfaces, which essentially arise from alloying in the bulk, another mechanism of alloying which is confined to the two-dimensions only, has been made possible due to advances in the experimental techniques of epitaxial growth, coupled with the advances in characterization methods like field ion microscopy [113] and scanning tunneling microscopy [114, 115]. During the growth of metal on metal, the possibility of mixing of the growing layer with the substrate opens up new avenues of alloying which is confined only to the few top layers of the substrate resulting in the so-called surface alloys. This has been demonstrated in the growth of Au on Cu(001) [115] and Au on Ag(110) [116] where

Au gets alloyed with the top substrate layers. However, Au is bulk-miscible both with Ag and Cu. This field got additional impetus when it was discovered that even metals which are *bulk-immiscible* can form atomically-mixed structures which are largely confined to the surface layer [117–119]. Some of these findings have been explained through the effects brought about by the changes in the coordination of atoms at the surface relative to the bulk. Nielsen *et al.* [117] argued that, in case of the surface alloys of Au on Ni(110), which is a bulk-immiscible system, the reduced coordination at the Ni(110) surface provides an optimum charge density for Au atoms to sit at Ni sites, as the smaller charge density provided by fewer neighbors is compensated for by their being now at a closer distance.

Apart from the deposition of one metal on the other, the co-deposition of two metals on a third metal substrate can also lead to alloying between them [106, 120]. In a class of surface alloys where the individual components have a large size mismatch with respect to the substrate, alloying has been observed. In such a system, because of the intermediate size of the substrate relative to the two components, the opposite strains imposed by the substrate on the two components can considerably get cancelled upon mixing, resulting in strain-stabilized surface alloys [106, 107, 120, 122]. However, it was found that for the Ag-Co/Ru(0001) system [123], Ag and Co did not atomically mix on the Ru(0001) surface even though this system would fulfill the size mismatch criterion: the nearest-neighbor (NN) distance of the bulk Ag is 8% larger than that of the substrate while that of Co is 7% smaller than the substrate, making the average NN distance of Ag-Co comparable to that of Ru. This suggests that elastic interactions alone cannot account for the

observed disfavoring of alloying in such systems. The cost of forming Ag-Co bonds from the breaking of Ag-Ag and Co-Co bonds affects the alloying and hence chemical interactions also play a crucial role. The presence of magnetism can further complicate matters.

Surface alloying of bulk-immiscible systems has been observed in many cases [124–130]. The formation of surface alloys is of particular interest also in the context of metal epitaxy. There has been observed the intermixing of adsorbate and substrate forming a thin film alloy [131]. Many nanoscale patterns have been observed in these systems, including CoAg/Ru(0001) [132, 133], CoAg/Mo(110), FeAg/Mo(110) [134], CuAg/Ru(0001) [106], and PdAu/Ru(0001) [122]. Some system-independent simulation studies on these two-dimensional nanopatterns have also been carried out explaining some of the experimentally observed phenomena [135–137].

Our goal is to get a better understanding of the factors governing alloying in such systems, identify suitable candidates that would merit experimental investigation, as well as to do a detailed investigation of magnetism in such systems.

4.4 Previous Work

4.4.1 Clusters

Atomic clusters represent the zero-dimensional systems. Small atomic clusters have been observed to exhibit novel electronic, magnetic and chemical properties [138]. Small clusters of ferromagnetic metals are known to show

enhanced magnetic moments [5, 139–142]. Ni_4 and Ni_5 clusters are found to be possessing magnetic moments per atom that are even higher than bulk Co [139]. Clusters of non-ferromagnetic transition metals like Rh, Pd and Ru have also been observed to be magnetic, while a more interesting observation is that there are magic sizes for which the magnetic moments are large. For example Rh_{15} , Rh_{19} , Rh_{22} , and Rh_{26} clusters are found to be magnetic magic sizes [143, 144].

4.4.2 Nanowires

Nanowires (or chains) are examples of one-dimensional systems. Magnetic nanowires hold promise in applications where the transport is required to be through a very small (nanometer) one-dimensional medium, such as in spintronics [145], tips used in magnetic microscopy [146, 147] and biomedical applications [148]. Since the pioneer experimental work of Elmers *et al.* [149] on Fe chains on the W(110) surface, a large amount of experimental and theoretical work has been done on the electronic and magnetic properties of these quasi-one-dimensional systems [150–154]. The nanowires of magnetic elements on noble metal surfaces show a huge enhancement in the magnetic moment both in the spin as well as in the orbital moment. First-principles study of finite Co_n ($n = 1, 3, 5, 7, 9$) nanowires [155] on Cu(001) show a spin moment of 1.8–1.9 μ_B . The moments decrease with increasing chain length and increasing the coordination of Co atoms. Similar behavior is observed for Fe chains on Cu(001) and Cu(111) surfaces [156] and for Co chains on Pt(111) using fully relativistic embedding techniques [157]. Delin *et al.* [158],

using all-electron DFT calculations including spin-orbit coupling, have shown that long Pd monostrand nanowires show a magnetic moment of about $0.7 \mu_B$ whereas Bahn *et al.* [159], using a pseudopotential approach, find no magnetism for the same system.

4.4.3 Surfaces and Interfaces

Surfaces and interfaces represent the two-dimensional or quasi-two-dimensional systems. The magnetism of surfaces of the TMs offers interesting observations: whereas all investigated surfaces of bulk magnets (Cr, Fe, Co and Ni) are found to be magnetic, the (100) surfaces of Ru, Pd are nonmagnetic and the surface magnetism of Rh(100) and V(100) is controversial. In some experimental [160–162] and theoretical [163–166] investigations, both the surfaces are found to be magnetic while in other work, these are found to be nonmagnetic [167–170]. Interestingly, the (100) surfaces of the M_xV_{1-x} , alloys where $M = \text{Ru, Rh, Pd}$, are found to be magnetic [171] in spite of the fact that the (100) surfaces of all these individual metals are nonmagnetic. The magnetism in this case is attributed to the presence of V(100)-surface-states in the pseudogap of the bulk density of states (DOS) of V that get extended to the Fermi level after alloying. The case of Pd(100) is an interesting example of the effect of reduced symmetry on magnetism. Due to the reduction of translational symmetry on surfaces, the degeneracy of energy states gets lifted, resulting in a splitting or broadening of the density of states. Thus, even though bulk Pd has a large paramagnetic susceptibility and is isoelectronic to Ni and is said to be “nearly” ferromagnetic owing to the presence of

a high DOS at E_f , the Pd(100) surface and even a Pd monolayer on Ag(100) remain nonmagnetic [168] as the enhancement of the band narrowing due to reduced coordination is counteracted by the band broadening caused by the reduction of symmetry at the surface. The effect of coordination and symmetry on magnetism can be studied by considering monolayers/thin films on different surfaces of a given crystal. For example, the (111) surface of a face-centered cubic (fcc) crystal and the (0001) surface of a hexagonal closed packing (hcp) crystal represent a triangular lattice with an in-plane coordination number of six, whereas the square lattice established by a fcc(100) surface has got fewer symmetries (four-fold) and lower in-plane coordination number (four). In general, it has been found that the magnetic moments of a four-fold coordinated monolayer are larger than those of six-fold coordinated ones. The local moments of transition metals on noble metal substrates have been studied extensively. For all the $3d$, $4d$ and $5d$ TM monolayers on Ag(100) and Ag(111), it has been found that the local moments are higher on Ag(100) than on Ag(111) [172–174].

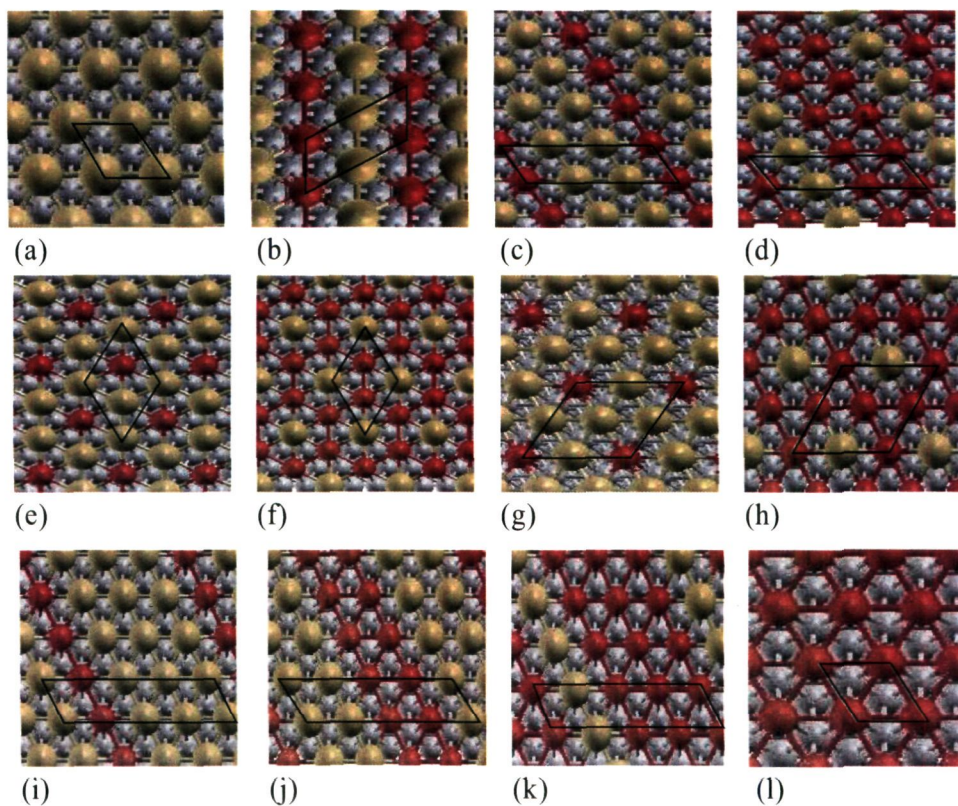
4.5 Systems Studied by Us

In our calculations, we consider a pair of metals, one magnetic, M, and the other nonmagnetic, N, (in their bulk state), and “deposit” a one atomic layer thick mixture of them on a substrate. Fe, Co and Ni are the magnetic components and Pb, Cd, Ag, Au and Pt, the nonmagnetic components of the pair, and Rh(111) is the substrate. We have considered all possible unit cells with one, two, three and four atoms, giving rise to six types of surface

unit cells: (1×1) , (2×1) , (3×1) , $(\sqrt{3} \times \sqrt{3})$, (2×2) and (4×1) . There are two surface atoms in (2×1) , three in (3×1) and $(\sqrt{3} \times \sqrt{3})$ each and four in each of the (2×2) and (4×1) cells. These cells together enable us to consider seven different compositions, namely $x = 0.0, 0.25, 0.33, 0.5, 0.67, 0.75$ and 1.0 for alloys of the type $M_xN_{1-x}/\text{Rh}(111)$. The (2×1) , (3×1) and the (4×1) cells give rise to linear chain type patterns (striped phase) (see Fig. 4.1) of alternating magnetic and nonmagnetic elements while the (2×2) and the $(\sqrt{3} \times \sqrt{3})$ cells lead to “Chinese checkerboard” like patterns. There are two types of low-energy sites available on the surface of the substrate: hcp and fcc sites. We have checked the relative stabilities of both these sites for the positions of overlayer (alloy) atoms.

Our choice of the M and N elements was guided primarily by the prevailing understanding of the mechanism of stress relaxation on surfaces [123, 131]. The bulk nearest-neighbor distances of magnetic and nonmagnetic elements chosen by us are respectively smaller and larger than that of the substrate. It was expected that putting a mixture of two elements with different sizes, on a third substrate, such that their average size is close to that of the substrate, would cancel the opposite stresses caused by opposite-sized atoms and thus stabilize the system [131]. Thus, even if two metals, due to their size mismatch, are immiscible in the bulk phase (first Hume-Rothery rule [110]), they would perhaps mix together on a surface provided by a suitable substrate, forming so-called strain stabilized surface alloys. Therefore, the initial expectation was that combinations of M and N that produce an average NN distance comparable to that of the Rh substrate might lead to a higher stability than other combinations. However, the effective atomic sizes on the

Figure 4.1: Top views of structural arrangements. (a) monolayer of N , i.e., $x=0$; (b) $x=0.5$ for (2×1) cell; (c) & (d) $x=0.33$ and 0.67 for (3×1) cell; (e) & (f) $x=0.33$ and 0.67 for $(\sqrt{3}\times\sqrt{3})$ cell; (g) & (h) $x=0.25$ and 0.75 for (2×2) cell; (i) to (k) $x=0.25$, 0.5 and 0.75 for (4×1) cell; and (l) monolayer of M . Magnetic atoms are represented by red spheres, nonmagnetic atoms by yellow spheres and the grey spheres represent the substrate atoms. The black solid lines mark surface unit cells.



Rh substrate could possibly be different than sizes in the bulk and this could alter mixing behavior. This choice (i.e., one magnetic and one nonmagnetic) can also test the validity of this simple mixing rule in the presence of magnetic species. Magnetic interactions can significantly affect how important stress-relaxation is in determining the energetics of these two-dimensional structures. As we will show, we find that this simple criterion of when surface mixing is favored indeed does not always hold true.

4.6 Method

Our calculations were done using *ab initio* spin polarized density functional theory [23] as implemented in the PWscf package of the Quantum-ESPRESSO (QE) distribution [67,175]. The interaction between ions and valence electrons for all metals was described by an ultrasoft pseudopotential [39]. The Perdew-Burke-Ernzerhof form of the generalized gradient approximation (GGA) [33] for the exchange-correlation functional was used. The Methfessel-Paxton smearing scheme [44] was used, with the smearing parameter set equal to 0.05 Ry. A plane wave basis set up to a kinetic energy cutoff of 20 Ry (272 eV) was used, together with a kinetic energy cutoff for the charge density of 160 Ry. All the structures were relaxed using Hellmann-Feynman forces [46]. The NN distances of all metals in their respective bulk structures were determined by performing a series of self-consistent total energy calculations at different lattice constants and fitting the data to get the equilibrium lattice constant. For bulk calculations, Brillouin zone integrations were done using an $8 \times 8 \times 8$ Monkhorst-Pack k-point grid [40].

We considered a single ordered overlayer of M and/or N, deposited pseudomorphically on a Rh (111) substrate. We did not consider reconstruction, i.e., a change in the surface atomic density was not allowed. The system was modeled using a supercell consisting of six substrate layers and one alloy overlayer, along with a vacuum layer of about 17 Å along the z ([111]) direction.

The top four layers (three of substrate and one of alloy overlayer) were allowed to relax and the bottom three were kept fixed at the bulk separation of the substrate. For surface calculations, we used $8 \times 8 \times 1$, $4 \times 8 \times 1$, $3 \times 8 \times 1$, $6 \times 6 \times 1$, $4 \times 4 \times 1$ and $2 \times 8 \times 1$ k-point meshes for Brillouin zone integration respectively for the (1×1) , (2×1) , (3×1) , $(\sqrt{3} \times \sqrt{3})$, (2×2) and (4×1) cells. We verified that our results were converged with respect to k-points and the energy cutoff, for both bulk as well as slab structures.

The calculation of the density of states (DOS) and the magnetic moments on individual atoms of the alloy were carried out by considering projection of total wavefunctions on individual spin-polarized atomic states (as implemented in `projwfc.x` code of QE).

4.7 Results and Discussion

4.7.1 Bulk

The bulk nearest-neighbor distance of each metal was calculated in its respective equilibrium structure. For Rh, these values were obtained using not the primitive fcc cell but a unit cell consisting of three atoms stacked along the

Table 4.1: *Calculated bulk nearest-neighbor distances (in Å). Experimental values are from Ref. [176]*

System	Rh	Co	Ni	Fe	Pt	Au	Ag	Cd	Pb
Ours	2.74	2.49	2.52	2.47	2.83	2.93	2.95	3.04	3.56
Expt.	2.69	2.49	2.51	2.52	2.77	2.88	2.89	3.02	3.50

[111] direction. This cell is commensurate to that used for the surface alloy calculations. The calculated magnetic moments for Fe, Co and Ni of 2.47, 1.71 and 0.74 μ_B per atom, respectively, are in reasonably good agreement with the corresponding experimental values of 2.22, 1.72 and 0.61 μ_B [71].

In Table 4.1 we have shown our calculated values for bulk nearest-neighbor distances. They are in fairly good agreement with experimental values; the errors are typical of those due to the use of the GGA.

4.7.2 Rh(111) Slab

We considered both a nine-layer and a six-layer Rh slab in the [111] direction, and converged our calculations with respect to vacuum and k-points convergence. We also considered two cases: (1) symmetric slab and (2) asymmetric slab. In the six layer symmetric case we allowed the two top and two bottom layers to relax whereas in the 9 layer symmetric case we allowed the three top and three bottom layers to relax. In the asymmetric case, only the corresponding numbers of top layers were relaxed. We calculated the surface energy and the degree of relaxation between the layers. It is found that all the top layers which were allowed to relax tend to relax inward in all the

cases. This inward relaxation is found to be similar for the two slabs: asymmetric slab ($\Delta_{12}=-2.4\%$, $\Delta_{23}=-1.3\%$, $\Delta_{34}=-0.34\%$) and the symmetric slab ($\Delta_{12}=-2.3\%$, $\Delta_{23}=-1.2\%$, $\Delta_{34}=-0.29\%$). Also we found the surface energy of the relaxed surface to be equal to 2.015 Joule/m² which is in excellent agreement with the result of an earlier calculation (2.01 Joule/m²) [177].

4.7.3 Monolayers on Rh (111)

Before studying alloying behavior, we first deposited pseudomorphic monolayers of M or N on the substrate separately. This corresponds to $x = 1.00$ or 0.00. In Table 4.2, we have tabulated the total energy differences between the monolayers on Rh(111) when they are put on the fcc and the hcp sites on the Rh(111) surface. From the results, we see that Fe and Co prefer to occupy the hcp sites while Ni prefers the fcc sites, even though the bulk stacking sequence is fcc for Rh(111). In contrast, monolayers of the nonmagnetic elements prefer fcc sites, with the exception of Pb. The energy differences between hcp and fcc stacking for the Fe and Co monolayers are less than 10.0 meV/surface atom, in agreement with another recent first-principles calculation [15].

The magnetic moments of magnetic monolayers on Rh(111) were found to be considerably enhanced compared to their bulk values. The total magnetic moment per magnetic atom respectively for Fe, Co and Ni monolayers were 3.32, 2.67 and 1.28 μ_B . The magnetic moments of the M atoms as well as induced moments on the four successive substrate layers along with the comparison with Ref [15], are given in Table 4.3. Interestingly, we find that

Table 4.2: *Energy difference, δE (in meV per surface atom), between fcc and hcp sites for monolayers on Rh(111). A negative value means that the fcc site is preferred over the hcp site.*

Monolayer	Pt	Au	Ag	Cd	Pb	Fe	Co	Ni
δE	-27.7	-19.3	-17.3	-8.2	9.5	5.2	7.8	-10.2

the induced moments on the first substrate layer is highest ($0.66 \mu_B$) when the overlayer is Co rather than Fe, even though bulk Fe has a higher magnetic moment than bulk Co. In fact, the moment on the first Rh(111) layer induced by an Fe monolayer ($0.33 \mu_B$) is lower than even the one induced by a Ni monolayer ($0.42 \mu_B$). The first and the third Rh(111) layers are coupled ferromagnetically to M layers (for all the three M). The second Rh layer is coupled ferromagnetically for the monolayers of Co and Ni, whereas the Fe monolayer induces an antiferromagnetic ordering in this layer. The behavior of Co and Ni monolayers is qualitatively similar. In agreement with Ref [15], antiferromagnetic moments are observed on the second and the third layers of Fe/Rh(111) and Co/Rh(111) respectively. The small disagreement in the values of these induced moments from Ref [15] could be due to the different number of substrate layers used in the two calculations. However, it should be noted that these induced moments become very small beyond the first substrate layer. This oscillatory behavior, which is similar to an RKKY-like interaction, has been discussed later in the chapter.

In Table 4.4, we tabulate the results obtained, upon geometry optimization, for δd_{12} , the percent change in the interlayer distances between the top substrate layer and the overlayer of M or N, relative to the bulk interlayer separation in the substrate. We find that the monolayers of M are relaxed

Table 4.3: *Magnetic moments, M , (in μ_B) of the monolayers of magnetic atoms M ($M=Fe, Co$ and Ni) on $Rh(111)$ and the induced moments on the four successive substrate layers Rh_1, Rh_2, Rh_3 and Rh_4 (from the top).*

Moments	Fe monolayer		Co monolayer		Ni monolayer
	Ours	Ref [15]	Ours	Ref [15]	Ours
$M(M)$	3.087	2.820	1.982	1.966	0.892
$M(Rh_1)$	0.332	0.161	0.657	0.531	0.418
$M(Rh_2)$	-0.063	-0.105	0.081	0.028	0.033
$M(Rh_3)$	-0.034	-0.032	-0.029	-0.083	-0.031
$M(Rh_4)$	0.001	0.017	-0.010	-0.003	-0.007

Table 4.4: *Percent change in the interlayer distances between the overlayer (M or N) and the top substrate layer, relative to the bulk interlayer distance in Rh .*

Monolayer	Pt	Au	Ag	Cd	Pb	Fe	Co	Ni
δd_{12} (%)	4.0	11.7	9.9	9.4	12.1	-7.6	-9.9	-9.0

inward while those of N are relaxed outward with respect to the bulk interlayer distance of the substrate. This can be attributed to the relative sizes of M (smaller) and N (larger) atoms with respect to atoms of the substrate. We expect that the effective size of the overlayer atoms is different at the surface compared to its bulk value. The calculation of this effective size (also called the “surface atomic diameter”) was done as follows [179]: we compressed/stretched the whole slab in the xy plane, while keeping the separation along the z direction constant, and calculated the corresponding surface stress. (Note that the contribution to the stress from the bulk, if present, has to be subtracted out.) A plot (see Fig. 4.2) of surface stress versus in-plane lattice constant was obtained and the in-plane lattice constant at which the surface stress was found to be equal to zero (by fitting a function derived

from Morse potential, described in the next section) was defined as the effective NN distance on the surface or the surface atomic diameter, b . In Fig. 4.2, we have shown this surface stress versus in-plane lattice constant for the monolayers of all the five nonmagnetic (Pt, Au, Ag, Cd, Pb) and the three magnetic elements (Fe, Co, Ni) on Rh(111). For the monolayers of magnetic elements, we have done this calculation for both the spin-polarized (filled circles and solid lines) as well as the non spin-polarized (unfilled circles and dotted lines) cases.

4.7.4 Surface Alloys

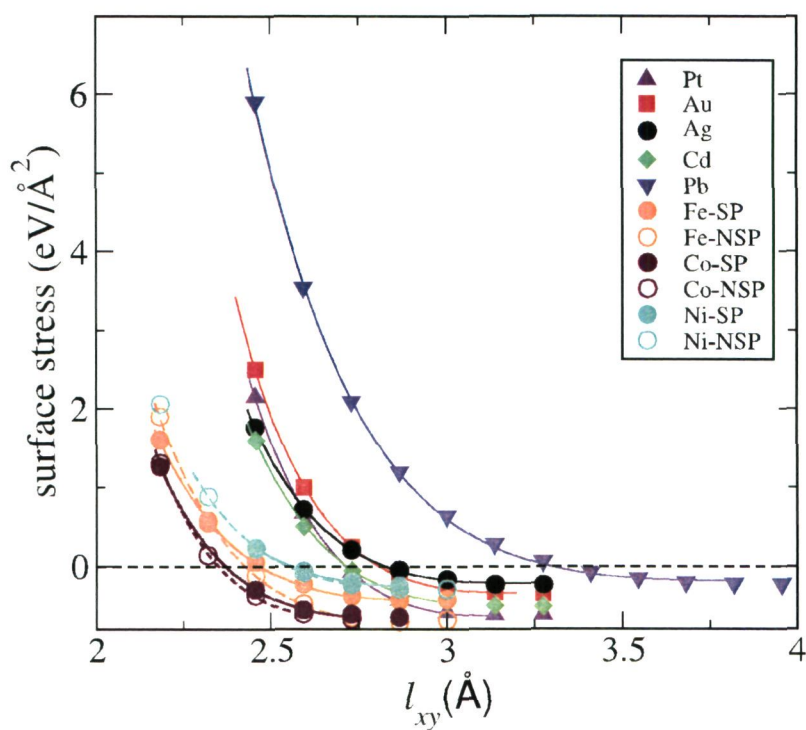
Structure and Miscibility

Next, we determine the mixing behavior of our surface alloys. The enthalpy of mixing, ΔH , of a surface alloy phase relative to the phase segregated forms is calculated according to the equation:

$$\Delta H = E(M_x N_{1-x}/Rh(111)) - xE(M/Rh(111)) - (1-x)E(N/Rh(111)) \quad (4.1)$$

where $E(M_x N_{1-x}/Rh(111))$ is the total energy of the slab with alloy-overlayer at composition x , $E(N/Rh(111))$ and $E(M/Rh(111))$ are the total energies of the slab with only non-magnetic and magnetic overlayers respectively; i.e., ΔH is the enthalpy of mixing of a given overlayer structure for a composition x relative to the phase segregated components (M/Rh(111) and N/Rh(111)). A negative ΔH implies that mixing of the two constituent metals is preferred

Figure 4.2: Surface stress (σ_{xx}^{surf}) versus in plane nearest-neighbor distance, l_{xy} , for the monolayers on Rh(111). Black symbols denote the data points taken by compressing/stretching the slab and lines are the fit derived from Morse potential



over their phase segregated forms.

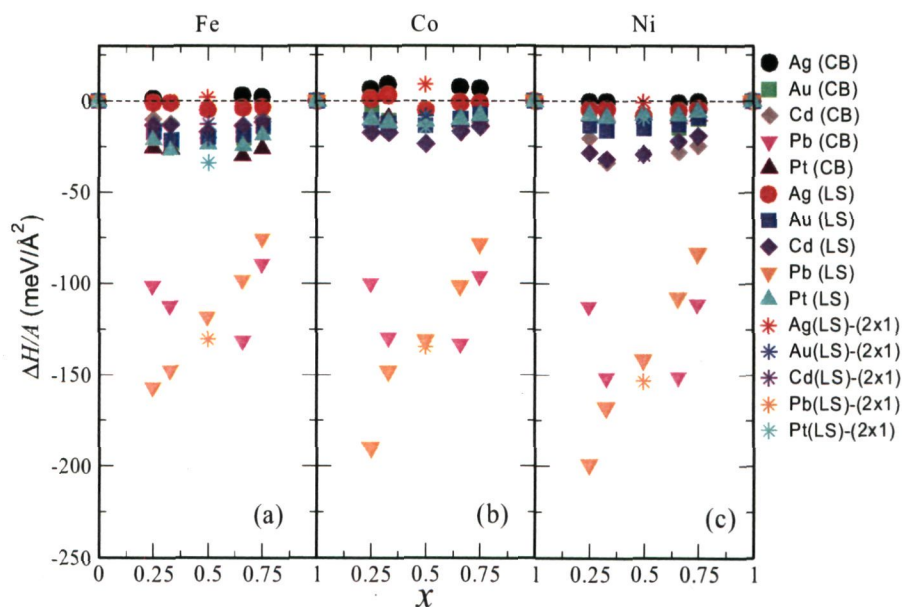
In Table 4.5 we have shown the favored site (fcc or hcp) of the surface alloys for all compositions considered. From Table 4.5 we see that in general a high concentration of Fe in its surface alloys favors the occupancy of hcp sites. This is particularly true for the Fe alloys with Ag and Cd. However, for a low concentration of Fe, the surface alloys with Pt, Au and Ag show a preference for the fcc site. Surprisingly, the surface alloys of Co in general prefer fcc sites even though the monolayer of Co (like that of Fe) shows a strong preference for the hcp site. Surface alloys of Ni prefer fcc sites for all the elements and at all the concentrations. This is expected as a Ni monolayer on Rh(111) shows a preference for the fcc site. However, it should be remarked that in all the cases the energy differences between the fcc and hcp configurations were small, of the order of 10 meV per surface atom, and in real experimental situations both of these configurations may conceivably be present. For subsequent analysis, we use the configurations which have the minimum energy.

Among the alloy systems studied by us, it is known for some pairs (e.g., Co-Au, Fe-Au, Co-Pb, Fe-Pb, Fe-Ag, Co-Ag and Ni-Ag) that they do not mix or show very limited solubility in their bulk phases [178]. The low surface energy of Ag promotes surface segregation of Ag in its alloys. Ag is bulk immiscible with all the three magnetic elements considered by us. The bulk alloy phase of Au with Ni shows a large miscibility gap leading to no alloying at low temperatures. However, surface alloying has been reported for Au on Ni(110) and Ni(111) surfaces [3,108].

Table 4.5: Site dependence (fcc or hcp) of surface alloys on Rh(111).

	Pt	Au	Ag	Cd	Pb
$M_{0.25}N_{0.75}$	(2×2) cell				
Fe	fcc	fcc	fcc	hcp	hcp
Co	fcc	fcc	fcc	fcc	fcc
Ni	fcc	fcc	fcc	fcc	fcc
$M_{0.25}N_{0.75}$	(4×1) cell				
Fe	fcc	fcc	fcc	hcp	hcp
Co	fcc	fcc	fcc	fcc	fcc
Ni	fcc	fcc	fcc	fcc	fcc
$M_{0.33}N_{0.67}$	$(\sqrt{3} \times \sqrt{3})$ cell				
Fe	fcc	fcc	hcp	hcp	fcc
Co	fcc	fcc	hcp	fcc	fcc
Ni	fcc	fcc	fcc	fcc	fcc
$M_{0.33}N_{0.67}$	(3×1) cell				
Fe	fcc	fcc	hcp	hcp	hcp
Co	fcc	fcc	fcc	fcc	fcc
Ni	fcc	fcc	fcc	fcc	fcc
$M_{0.50}N_{0.50}$	(2×2) cell				
Fe	fcc	fcc	hcp	hcp	fcc
Co	fcc	fcc	fcc	fcc	fcc
Ni	fcc	fcc	fcc	fcc	fcc
	Pt	Au	Ag	Cd	Pb
$M_{0.50}N_{0.50}$	(4×1) cell				
Fe	fcc	fcc	hcp	hcp	hcp
Co	fcc	fcc	fcc	fcc	fcc
Ni	fcc	fcc	fcc	fcc	fcc
$M_{0.67}N_{0.33}$	$(\sqrt{3} \times \sqrt{3})$ cell				
Fe	hcp	hcp	hcp	hcp	fcc
Co	fcc	fcc	hcp	fcc	fcc
Ni	fcc	fcc	fcc	fcc	fcc
$M_{0.67}N_{0.33}$	(3×1) cell				
Fe	hcp	hcp	hcp	hcp	hcp
Co	fcc	fcc	hcp	fcc	fcc
Ni	fcc	fcc	fcc	fcc	fcc
$M_{0.75}N_{0.25}$	(2×2) cell				
Fe	hcp	hcp	hcp	hcp	hcp
Co	fcc	hcp	fcc	fcc	fcc
Ni	fcc	fcc	fcc	fcc	fcc
$M_{0.75}N_{0.25}$	(4×1) cell				
Fe	hcp	hcp	hcp	hcp	hcp
Co	fcc	fcc	hcp	fcc	fcc
Ni	fcc	fcc	fcc	fcc	fcc

Figure 4.3: Enthalpy of mixing ΔH of surface alloys with respect to composition x : ΔH is measured relative to pure monolayer configuration according to Eq. (1). ΔH for a given alloy is plotted for two different structural patterns: linear striped structures [corresponding to (2×1) , (3×1) and (4×1) cells and denoted as “LS”] and the “Chinese checkerboard” structures [corresponding to the (2×2) and $(\sqrt{3} \times \sqrt{3})$ cells denoted as “CB”]. The two different colors of a given symbol (e.g., magenta and orange colors for the down-pointing-triangle) denote these two structures for the given alloy. The stars of a given color correspond to the (2×1) cell for the alloy of the corresponding nonmagnetic element. (a), (b) and (c) denote the surface alloys of the Fe, Co and Ni respectively.



We find (see Fig. 4.3) that some of these pairs (Co-Ag, Fe-Ag, Co-Au) do not quite mix on Rh(111) too. Our finding for Co-Ag is similar to the experimental finding by Thayer *et al.* on Ru(0001) [123] as well as corresponding first-principles calculations [123,179]. In the experiment they found that Ag and Co on Ru(0001) do not show atomic-level mixing. This non-mixing was attributed to the dominant unfavorable chemical interaction between Co and Ag. The energetics of mixing on the two substrates, Rh(111) and Ru(0001), have been found to be very similar [105]. In addition to Co-Ag, our calculations predict that mixing of Ag with Fe and Ni is also not favorable. However, we find that the other bulk-immiscible pairs, when co-deposited on Rh(111) surface, show significant mixing. The high miscibility of Pb-alloys is particularly interesting given the fact that they do not at all fulfill the average size criterion.

In Fig. 4.3, we have plotted ΔH versus composition x as obtained by performing spin-polarized calculations. The symbols are as follows: Ag: circles; Au: squares; Cd: diamonds; Pt: up-pointing-triangles; Pb: down-pointing-triangles. The two different colors for a given symbol correspond to the two types of structures we have considered: (1) linear chain or stripe-phase type (denoted as “LS”) which correspond to the (4×1) and the (3×1) and (2×1) cells and (2) “Chinese checkerboard” type (denoted as “CB”) which correspond to the $(\sqrt{3}\times\sqrt{3})$ and the (2×2) cells. Note that the (2×2) structure for $x = 0.5$ gives rise to same structure as (2×1) . The star symbol stands for the (2×1) cell. The filled and the unfilled symbols [solid and dotted stars for (2×1) cells] correspond to the spin-polarized and the non spin-polarized cases respectively. The enthalpy of mixing for the alloys of the five nonmagnetic

elements is again shown, along with the two interactions contributing to it, in Figs. 4.7-4.11 further below.

First, we note that the magnitudes of the enthalpy of mixing of the surface alloys are quite similar for all the three magnetic elements. The values of ΔH are spread within $40 \text{ meV}/\text{\AA}^2$ for the three magnetic elements. The mixing behavior with respect to nonmagnetic elements shows the following trend: Pb alloys are the most stable while Ag alloys are the least. The mixing enthalpy of the rest of the alloys is roughly of the same order. One can see that the mixing of Co-Ag and Fe-Ag alloys (especially for checkerboard structures) is not favored even on the surface. However, for larger concentrations of Fe and Co, the striped-phase structures display small mixing (more clearly shown in Fig. 4.9 for the Ag alloys). Unlike Fe and Co, all Ni alloys show mixing on the Rh(111) surface.

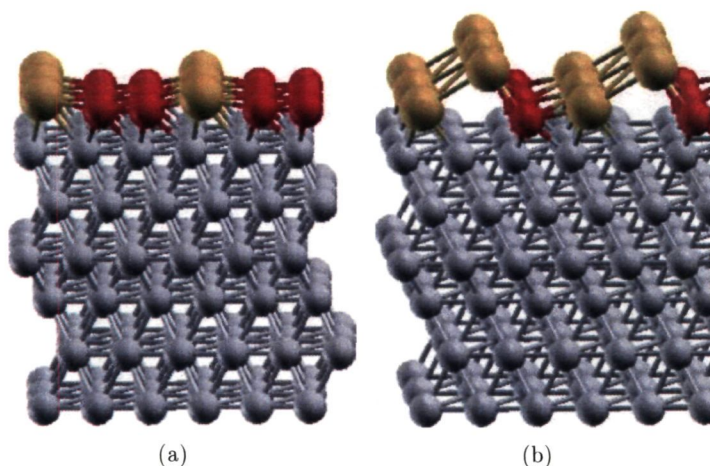
The high miscibility of Pb-alloys is particularly interesting given the fact that they do not fulfill the average size criterion. We remark here that although we have not allowed any reconstruction, owing to its large size, the Pb monolayer on Rh(111) is very much susceptible to reconstruction. This can significantly change the mixing behavior of Pb alloys. In fact we have checked that there is significant buckling in the Pb monolayer (if it is allowed to buckle) making it more stable and thus causing significant changes in the formation energy of its surface alloys. Larger buckling allowed in a (4×1) cell increases the stability of Pb monolayer thereby reducing the mixing enthalpy of Pb-alloys by three to four times when compared to the (1×1) cell, where the buckling is not possible for there is only one Pb atom per unit cell. However, in Fig. 4.3, we have used a (1×1) cell for the monolayer of Pb for calculating ΔH for

the (4×1) alloy structure. The mixing stability of the stripe-phase of Pb alloys (orange down-pointing-triangles in Fig. 4.3) increases as we increase the concentration of Pb. This is due to larger buckling with increased Pb concentration. For the mixed checkerboard type structures, however, the mixing stability is maximum for intermediate concentrations and it decreases for low or high concentrations (magenta down-pointing-triangles in Fig. 4.3). Interestingly, for low concentrations of M ($x = 0.25$ and 0.33), the stripe phases (3×1 and 4×1) of Pb alloys are favored over the checkerboard phases ($\sqrt{3} \times \sqrt{3}$ and 2×2) whereas for high concentrations ($x = 0.67$ and 0.75), the opposite is true (compare the filled orange and magenta down-pointing-triangles). The energy difference between the two phases is also significant. This could be probably because of the large size of Pb which would cause more strain in the stripe phase structures (3×1) and (4×1) compared to the more symmetric checkerboard structures ($\sqrt{3} \times \sqrt{3}$ and 2×2) (see Fig. 4.1). For the $x = 0.25$ and $x = 0.33$ concentrations, the adjacent rows of Pb atoms in the (3×1) and (4×1) structures are highly strained and get buckled (Fig. 4.4) allowing for a larger relaxation than the relaxation achieved in the (2×2) and ($\sqrt{3} \times \sqrt{3}$) structures. For the higher concentrations ($x = 0.67$ and $x = 0.75$), the adjacent rows of Pb are replaced by the rows of magnetic atoms which are comparatively less strained.

Spin Polarized versus Non Spin Polarized Calculation: The Role of Magnetism

The role of magnetism on the mixing property of surface alloys is important, as has been found in a recent work on Fe-Au/Ru(0001) [109]. The

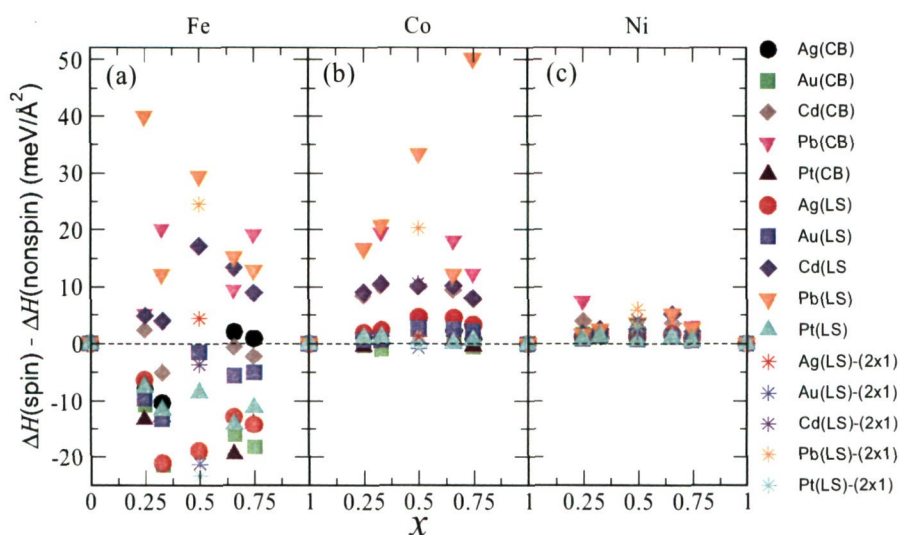
Figure 4.4: Side view of the Fe-Pb alloys structures: (a) for $x=0.67$ and (b) for $x=0.33$ composition. Red, yellow and grey spheres are the Fe, Pb and Rh atoms respectively. See the larger buckling when the concentration of Pb atoms is high.



authors found that magnetism, rather than the (hitherto believed) stress relief, was the principal driving force that stabilized the surface alloy of Fe-Au on Ru(0001).

In Fig. 4.5, we have shown the difference of the enthalpies of mixing between the spin polarized and non spin polarized results. We find that the mixing of different alloy systems and different structures are affected to different degrees by the presence or absence of magnetism. For Fe alloys of Pb, magnetism always disfavors mixing, while of Au and Pt, it always favors mixing. For Co alloys, magnetism always disfavors mixing of striped structures. For the checkerboard structures also, the presence of magnetism disfavors mixing for all the alloy systems except for Co-Au and Co-Pt. For Ni alloys, the effect of spin polarization is relatively small, however, the presence of magnetism is found to always disfavor mixing for all structures. With respect to

Figure 4.5: The difference of the enthalpy of mixing between spin polarized and non spin polarized calculations with respect to composition x : The enthalpy difference is plotted for two different structural patterns: linear striped structures [corresponding to (2×1) , (3×1) and (4×1) cells and denoted as “LS”] and the “Chinese checkerboard” structures [corresponding to the (2×2) and $(\sqrt{3} \times \sqrt{3})$ cells denoted as “CB”]. The two different colors of a given symbol (e.g., magenta and orange colors for the down-pointing-triangle) denote these two structures for the given alloy. The stars of a given color correspond to the (2×1) cell for the alloy of the corresponding nonmagnetic element. (a), (b) and (c) denote the surface alloys of the Fe, Co and Ni respectively.



nonmagnetic elements, the alloys of Pb, for all the considered compositions and structures, show an enhanced mixing when the magnetic interaction is turned off, whereas the alloys of Pt behave in the opposite way.

In the bulk, magnetic and cohesive energies compete with each other: bonding is strong when there is greater overlap between orbitals and that increases bandwidth, while enhancement of ferromagnetism demands narrower bandwidth. But in the case of a two-dimensional structure on a substrate (e.g., surface alloys) the role of surface stress also becomes important. When we constrain the growth to be pseudomorphic, the strain is minimum when the size of surface alloy constituents is the same as that of the substrate. In our case the role of strain seems to play a dominant role for the Pb and Pt alloys. The average NN spacing for Fe-Pb (3.02 Å) is larger than that of the substrate (2.73 Å) while that of Fe-Pt (2.65 Å) is smaller. Since the ferromagnetic interaction tends to increase interatomic spacings, the inclusion of spin polarization expands both the systems (Fe-Pt and Fe-Pb), helping to minimize the stress for Fe-Pt, while further increasing it for Fe-Pb, decreasing its stability. For other systems, this effect is less pronounced as the average sizes are not very far away from that of the substrate's, and depending upon the composition and geometry, magnetism can favor or disfavor stability.

Elastic and Chemical Contributions to the Enthalpy of Mixing

Going by the simple size-based rules only, one would have expected the energetics of Ag and Au alloys to be very similar, as the sizes of Ag and Au atoms are nearly equal (2.89 and 2.88 Å respectively). However, this is not

borne out by our results. This indicates that the size-mismatch (elastic energy) alone can not account for the mixing behavior and one must also take into account the chemical contribution (accounting for the chemical nature of the alloying species). So we separate out the contribution of elastic and chemical effects to ΔH .

The elastic energy is estimated by assuming all the NN atoms in the overlayer interact via a Morse potential of the form:

$$V_{ij}(r) = A_0^{ij} [1 - \exp[-A_1^{ij}(r - b^{ij})]]^2, \quad (4.2)$$

where r is the distance between the NN atoms i and j , b^{ij} is their equilibrium NN distance and A_0^{ij} and A_1^{ij} are parameters of the potential related to the depth and the width of the potential respectively. There are three types of bonds on the surface: the bond between two magnetic atoms (with bond length b^{MM} and potential parameters A_0^{MM} and A_1^{MM}), bond between two nonmagnetic atoms (with the bond length b^{NN} and parameters A_0^{NN} and A_1^{NN}) and the bond between a magnetic atom and a nonmagnetic atom (with bond b^{MN} and parameters A_0^{MN} and A_1^{MN}). For the determination of b^{MM} and b^{NN} , as described the previous section, we make a symmetric slab of Rh containing n number of layers with the magnetic and the nonmagnetic element on the top and the bottom layers and stretch/compress it in the xy direction to an in-plane NN distance l_{xy} keeping the distance along the z direction fixed (at the bulk separation of Rh). The resulting ‘‘surface stress’’ for this configuration can then be written as [179]:

$$\sigma_{xx}^{surf}(l_{xy}) = \frac{1}{2}[\sigma_{xx}^{slab}(l_{xy})L_z - (n-2)\sigma_{xx}^{bulk}(l_{xy})\frac{c}{3} + \sigma_{zz}^{bulk}(l_{xy})\frac{l_{xy}^2}{2c}]. \quad (4.3)$$

Here, $\sigma_{xx}^{slab}(l_{xy})$ is the ‘volume’ stress (as opposed to surface stress) for the whole slab which contains the contributions not only from the outermost surface layers but also from the substrate layers (which need to be subtracted out), σ_{xx}^{bulk} and σ_{zz}^{bulk} are the x and z components of the volume stresses for bulk Rh (which was obtained using a similar set of stretching/compressing calculation on a bulk unit cell consisting of three Rh layers stacked along [111], c is the length of this bulk unit cell along the z direction: $c = \sqrt{6}s$). L_z is the length of the slab unit cell (including the vacuum layers) in z direction: $L_z = 5\sqrt{6}s$. Note that σ^{bulk} will be zero for the Rh bulk equilibrium lattice constant ($l_{xy} = s$). Thus plots of $\sigma_{xx}^{surf}(l_{xy})$ versus l_{xy} (Fig. 4.2) are obtained and the l_{xy} for which the surface stress $\sigma_{xx}^{surf}(l_{xy})$ became zero was identified as b^{MM} or b^{NN} , the preferred NN distance (of magnetic or nonmagnetic atoms, as the case may be) at the substrate. In analogy with the Lorentz-Berthelot mixing rule [184], where the energy and the size parameters of the interaction potential of a ‘‘mixed’’ component are presumed to be geometric and arithmetic means of the pure components, respectively, we approximate b^{MN} by the arithmetic mean of b^{MM} and b^{NN} while A^{MN} s are approximated by the geometric mean of the corresponding A^{MM} and A^{NN} . Table 4.6 shows the parameters obtained in this way for the interatomic potentials between surface atoms.

In this way we can write down the elastic contribution to the enthalpy of

Table 4.6: Values for the parameters of Morse potentials for the monolayers of the overlayer elements.

M/N	A_0 (eV)	A_1 (\AA^{-1})	b (\AA)
Fe	0.8092	1.635	2.47
Co	1.2281	1.650	2.37
Ni	0.4393	1.825	2.56
Pt	1.1438	1.721	2.71
Au	0.5549	1.909	2.81
Ag	0.3835	1.872	2.82
Cd	0.9466	1.638	2.72
Pb	0.6242	1.171	3.33

mixing for different compositions as:

$$\Delta H^{el} = 6E_{MN}^{el} - 3E_{MM}^{el} - 3E_{NN}^{el} \quad (4.4)$$

for the 25% composition of the (2×2) cell,

$$\Delta H^{el} = 4E_{MN}^{el} - 2E_{MM}^{el} - 2E_{NN}^{el} \quad (4.5)$$

for the 33% composition of the (3×1) cell,

$$\Delta H^{el} = 6E_{MN}^{el} - 3E_{MM}^{el} - 3E_{NN}^{el} \quad (4.6)$$

for the 33% composition of the $(\sqrt{3} \times \sqrt{3})$ cell,

$$\Delta H^{el} = 8E_{MN}^{el} - 4E_{MM}^{el} - 4E_{NN}^{el} \quad (4.7)$$

for the 50% composition of the (2×2) cell,

$$\Delta H^{el} = 4E_{MN}^{el} - 2E_{MM}^{el} - 2E_{NN}^{el} \quad (4.8)$$

for the 50% composition of the (2×1) cell,

$$\Delta H^{el} = 4E_{MN}^{el} - 2E_{MM}^{el} - 2E_{NN}^{el} \quad (4.9)$$

for the 67% composition of the (3×1) cell,

$$\Delta H^{el} = 6E_{MN}^{el} - 3E_{MM}^{el} - 3E_{NN}^{el} \quad (4.10)$$

for the 67% composition of the $(\sqrt{3} \times \sqrt{3})$ cell,

$$\Delta H^{el} = 6E_{MN}^{el} - 3E_{MM}^{el} - 3E_{NN}^{el} \quad (4.11)$$

for the 75% composition of the (2×2) cell and,

$$\Delta H^{el} = 4E_{MN}^{el} - 2E_{MM}^{el} - 2E_{NN}^{el} \quad (4.12)$$

for all the three compositions of the (4×1) cell.

It is clear from these expressions that the elastic contribution to ΔH is symmetric about the 50% composition (for we have considered pairwise interactions only). In Fig. 4.6, we have plotted contributions to the elastic energy coming from the three types of bonds (M-M, N-N, and M-N) for $x = 0.5$ (of 2×2 cell). It is clear that the high contribution coming from the Pb-Pb

bonds is responsible for high enthalpy of mixing for Pb alloys. Moreover, the contribution from the M-N bond is always positive (i.e., disfavoring mixing) while from the other two bonds it is always negative. For the monolayers of magnetic elements, the Co monolayer shows the highest negative elastic contribution to ΔH followed by the Fe and Ni monolayers. This is because the effective NN distance of Co on Rh(111) is lowest, making it more strained due to a high size-mismatch on the surface. This results in relatively high contribution of elastic energy for Co alloys compared to Fe and Ni alloys. Ni alloys show the lowest $|\Delta H^{ela}|$. The contribution from the N-N bonds for Ag and Au are similar and for Cd and Pt alloys is very small. We have already seen that the effective size of Cd on Rh(111) is very small (compared to its bulk size) making the elastic energy contribution from Cd-Cd bonds small. The large size mismatch for Pb results in high elastic energy for Pb monolayer on Rh(111). This contributes greatly to the (negative) formation energy of its alloys against the phase segregated form. However, it should be mentioned that the high stability of Pb-alloys could be just an artifact of our assumption of pseudomorphic growth. In actual experimental conditions, this high elastic energy contained in the Pb monolayer on Rh(111) could be released by reconstruction, thereby reducing its contribution to the mixing. Indeed, we see the effect of reconstruction for the linear chain structures (which are rather anisotropic) of the (3×1) and (4×1) cells. The large strain present in these systems for high Pb concentrations causes the adjacent chains of Pb atoms to buckle outward in order to release the strain (see Fig. 4.4). These systems, therefore, show a lower enthalpy of mixing compared to the systems where there is more isotropicity (i.e., the $\sqrt{3} \times \sqrt{3}$ and 2×2 structures)

(compare the filled orange and magenta down-pointing-triangles for $x=0.25$ and 0.33 in Fig. 4.3).

In the second rows of Figs. 4.7-4.11 we have shown the elastic energy contribution to ΔH for the surface alloys. We find that the elastic effects favor surface alloy formation as ΔH^{ela} is negative for nearly all the systems, at all the compositions considered. However, for Pt and Cd alloys, elastic interactions do not contribute much towards mixing. This can be attributed to the smaller surface NN distances on Rh(111) for these two elements. Strain stabilization becomes less favorable as both the components now have smaller surface atomic diameter on the substrate. The large size mismatch for Pb on Rh(111) results in higher mixing of Pb alloys as a result of the highly strained Pb-Pb bonds (in the phase-segregated Pb monolayer). The contribution of the elastic interactions to ΔH for the two 33% and 67% configurations corresponding to (3×1) and $(\sqrt{3} \times \sqrt{3})$ structures are different: the elastic energy contributes more towards the mixing of the surface alloys of $(\sqrt{3} \times \sqrt{3})$ structures compared to that of the (3×1) structures. This is presumably due to the presence of more M-N bonds in the $(\sqrt{3} \times \sqrt{3})$ cell (there are 67% of M-N bonds in the $\sqrt{3} \times \sqrt{3}$) compared to the (3×1) cell (44%).

Figure 4.6: Contribution to the elastic energy ΔH^{ela} from the three types of bonds: M-M, N-N, and M-N for $x=0.5$ of the (2×2) cell.

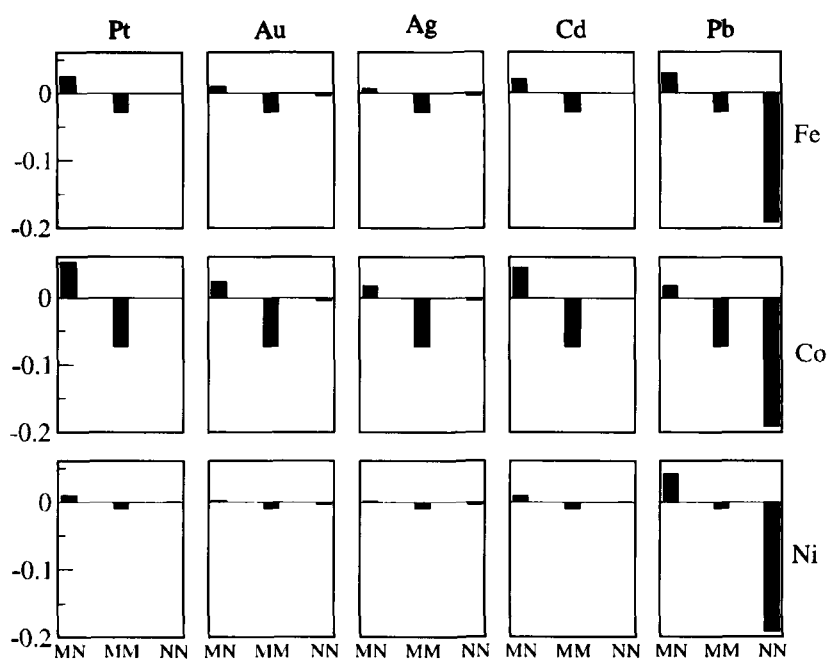


Figure 4.7: Enthalpy of mixing ΔH , together with the elastic and chemical contributions, as a function of x , the fraction of magnetic element, for Pt alloys. The first, second and the third row correspond to the total enthalpy of mixing (ΔH), the elastic contribution (ΔH^{ela}) and the chemical contribution (ΔH^{chem}) respectively. The three columns correspond to the alloys with the three magnetic elements, shown on the top of graph. The filled and the unfilled symbols [solid and dotted stars for (2×1) cells] correspond to the spin-polarized and the non spin-polarized cases respectively. Circles denote the Chinese checkerboard structures and triangles and stars denote the linear striped structures.

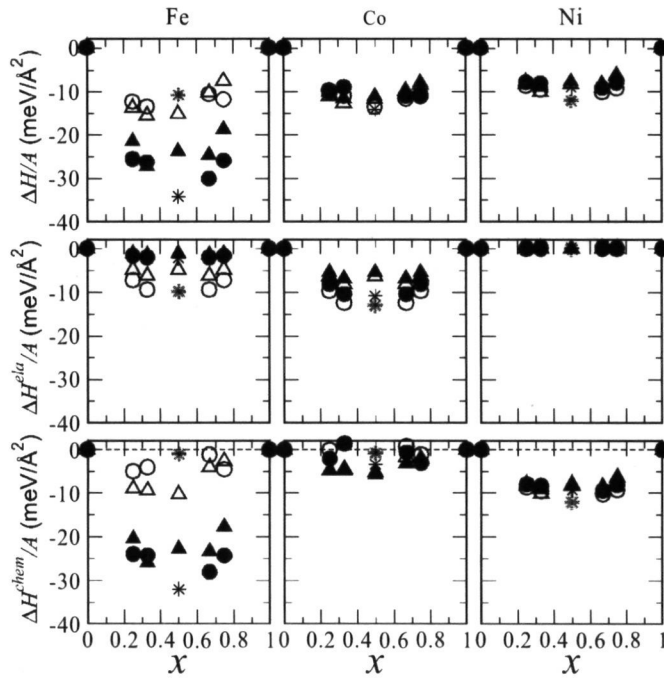


Figure 4.8: Enthalpy of mixing ΔH , together with the elastic and chemical contributions, as a function of x , the fraction of magnetic element, for Au alloys. The first, second and the third row correspond to the total enthalpy of mixing (ΔH), the elastic contribution (ΔH^{ela}) and the chemical contribution (ΔH^{chem}) respectively. The three columns correspond to the alloys with the three magnetic elements, shown on the top of graph. The filled and the unfilled symbols [solid and dotted stars for (2×1) cells] correspond to the spin-polarized and the non spin-polarized cases respectively. Circles denote the Chinese checkerboard structures and triangles and stars denote the striped structures. Note that the plots are not on the same scale.

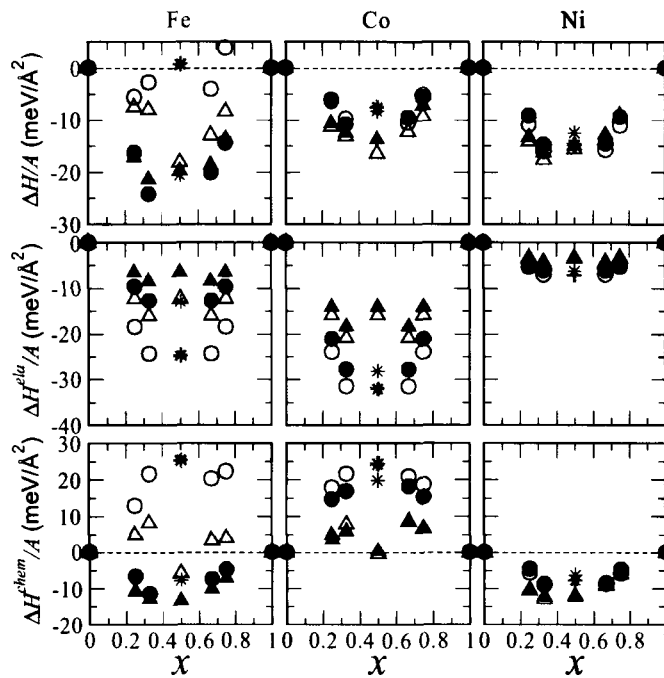


Figure 4.9: Enthalpy of mixing ΔH , together with the elastic and chemical contributions, as a function of x , the fraction of magnetic element, for Ag alloys. The first, second and the third row correspond to the total enthalpy of mixing (ΔH), the elastic contribution (ΔH^{ela}) and the chemical contribution (ΔH^{chem}) respectively. The three columns correspond to the alloys with the three magnetic elements, shown on the top of graph. The filled and the unfilled symbols [solid and dotted stars for (2×1) cells] correspond to the spin-polarized and the non spin-polarized cases respectively. Circles denote the Chinese checkerboard structures and triangles and stars denote the striped structures. Note that the plots are not on the same scale.

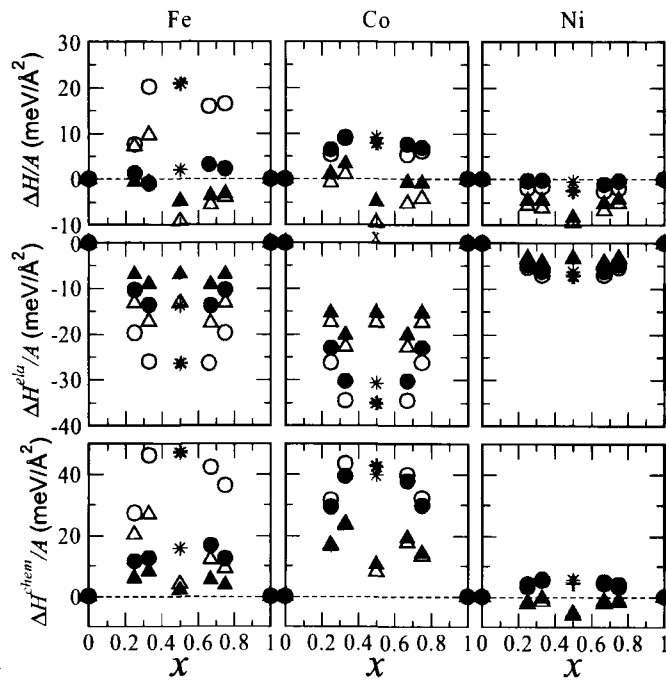


Figure 4.10: Enthalpy of mixing ΔH , together with the elastic and chemical contributions, as a function of x , the fraction of magnetic element, for Cd alloys. The first, second and the third row correspond to the total enthalpy of mixing (ΔH), the elastic contribution (ΔH^{ela}) and the chemical contribution (ΔH^{chem}) respectively. The three columns correspond to the alloys with the three magnetic elements, shown on the top of graph. The filled and the unfilled symbols [solid and dotted stars for (2×1) cells] correspond to the spin-polarized and the non spin-polarized cases respectively. Circles denote the Chinese checkerboard structures and triangles and stars denote the striped structures.

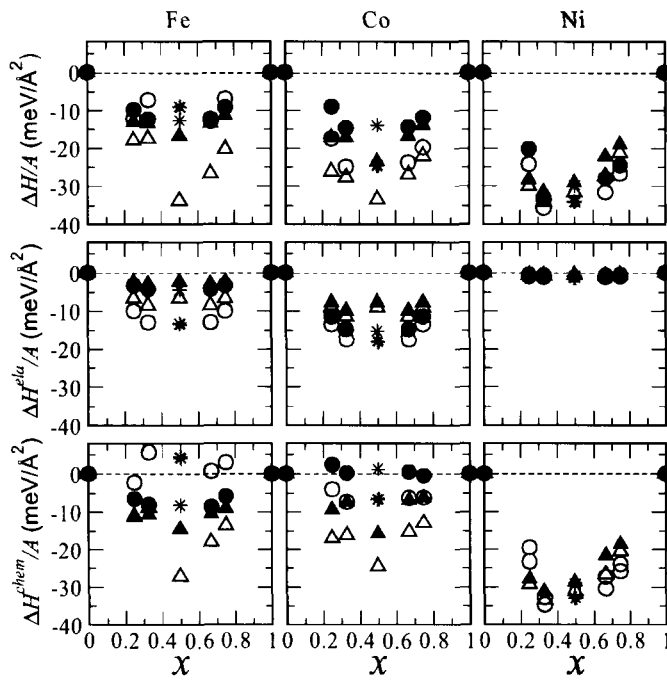
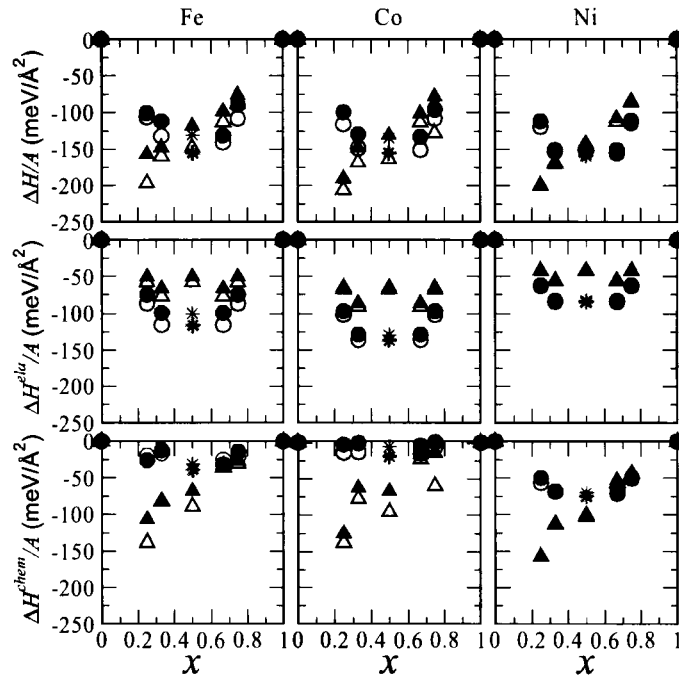


Figure 4.11: Enthalpy of mixing ΔH , together with the elastic and chemical contributions, as a function of x , the fraction of magnetic element, for Pb alloys. The first, second and the third row correspond to the total enthalpy of mixing (ΔH), the elastic contribution (ΔH^{ela}) and the chemical contribution (ΔH^{chem}) respectively. The three columns correspond to the alloys with the three magnetic elements, shown on the top of graph. The filled and the unfilled symbols [solid and dotted stars for (2×1) cells] correspond to the spin-polarized and the non spin-polarized cases respectively. Circles denote the Chinese checkerboard structures and triangles and stars denote the striped structures.



Since the elastic contribution results in mixing, the unfavored mixing of Ag alloys must be due to “chemical” interactions. In these systems, the chemical interactions between the alloy components would be unfavored and would be more dominant. The favored mixing of Pt alloys in general and of Pt-Ni alloy in particular, on the other hand, must be due to the favored and dominant chemical effects. Thus we separate out the two interactions by assuming that the total energy of the system is contributed by two type of interactions: elastic and chemical. So the difference between the *ab initio* ΔH and the ΔH^{ela} will give us the chemical energy contribution. We have thus plotted $\Delta H^{chem} \equiv \Delta H - \Delta H^{ela}$, the chemical energy contribution to the enthalpy of mixing, as a function of composition x , shown in the bottom rows of the Figs. 4.7-4.11. The positive ΔH^{chem} for Ag surface alloys does account for their immiscibility. We notice that the chemical energy contributions for Fe and Co alloys are quite similar for the non spin-polarized case. It is also clear that the mixing of Pt alloys is mainly contributed by the chemical interactions. Interestingly, in contrast to the bulk alloys of Pb-Co, Pb-Fe and Au-Fe which are immiscible in the bulk, their surface alloy counterparts show favorable chemical mixing on Rh(111).

We have also calculated the effect of magnetism on the elastic and chemical interactions. In Figs. 4.7-4.11, the corresponding unfilled symbols denote the interactions when magnetism is switched off (i.e., ΔH^{ela} calculated using b^{MM} 's from non spin-polarized calculations). Interestingly, for all alloys and for all compositions, the elastic contribution to mixing is always favored when systems are non spin-polarized.

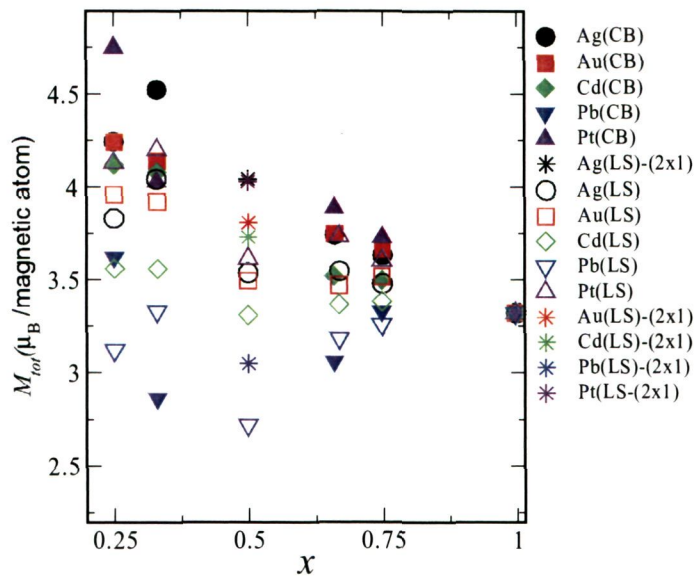
Magnetic Moments

The observation of interesting magnetic behavior as a result of reduced dimensionality and coordination in low-dimensional systems has generated immense interest in recent years. The effect of surface alloying further enriches the subject. While for some systems, the effect of alloying has been found to suppress the magnetism, for others, it has been found to do the opposite [180–183]. The systems we have studied manifest the complexity of both the effects. In a combined experimental and theoretical study done recently, magnetism was found to be a driving force to stabilize the surface alloys of Fe-Au/Ru(0001) [109].

In Figs. 4.12-4.14, we have shown our results for the calculated total magnetic moments, M_{tot} , versus concentration of magnetic element, x , for the alloys of Fe, Co and Ni. M_{tot} is the magnetic moment of the unit cell per magnetic atom (note that these include induced moments on the “nonmagnetic” overlayer and substrate atoms). For a given structure, as x increases, the effective coordination number (i.e., the number of magnetic neighbors) of the magnetic element also increases.

As we checked the stability of surface alloys with respect to the two available low-energy (hcp or fcc) sites, we have plotted here M_{tot} corresponding to the more stable one among the two. Interestingly, we found that the hcp alloys *always* showed higher magnetic moments compared to the corresponding fcc alloys, by about $0.2 \mu_B$. This particular result can be explained as follows: We found that the average distances of the magnetic atoms from the nonmagnetic atoms of the alloys were larger in hcp alloys compared to the

Figure 4.12: Total magnetic moment, M_{tot} (in μ_B), versus composition x for Fe alloys. M_{tot} is the magnetic moment of the whole cell divided by the number of magnetic atoms on the surface. The filled symbols correspond to the (2×2) and $(\sqrt{3} \times \sqrt{3})$ structures and the unfilled symbols correspond to the (4×1) and (3×1) structures. The stars correspond to the (2×1) cell. CB and LS refer to checkerboard and linear stripe structures respectively.



fcc alloys, while the average distances of the magnetic atoms from the first substrate layer were shorter in hcp alloys. Although, the shorter distance from the substrate layer for the hcp alloys would result in a larger hybridization, thereby reducing the magnetic moment of the magnetic atoms, it (the shorter distance) causes a larger polarization of the Rh atoms, thereby increasing their induced moments. So, the larger moments of the hcp alloys are due to the shorter overlayer-substrate distance, which results in a larger magnetization induced on the first substrate layer.

We find (from Figs. 4.12-4.14) that the magnetic moments per magnetic atom of the monolayers (the points corresponding to $x=1$) are enhanced significantly (3.32, 2.67 and $1.28 \mu_B$ for Fe, Co and Ni monolayers respectively) compared to the moments in their bulk phase (2.47, 1.71 and $0.74 \mu_B$ in the same order). This behavior is typical of the effect of reduced dimensionality and coordination.

Comparing the magnitudes of the moments of the surface alloys of Fe (Fig. 4.12), Co (Fig. 4.13) and Ni (Fig. 4.14), we see that the overlayer structures of Fe show larger magnetic moments followed by that of Co and Ni, which is expected owing to the order of magnetic moments in their pure elemental states. However, the variation of magnetic moments of these surface alloys with the composition of the magnetic element is interesting: (1) in general, the magnetic moments of Fe alloys with all the nonmagnetic elements, with the exception of Pb, increase with decreasing Fe concentration; (2) the magnetic moments of Co and Ni alloys also increase with decreasing x , except with the Pb and Cd. That is, in general for Fe alloys, the lower the concentration of Fe, the higher the magnetic moment. The magnetic moments of Co and Ni alloys for Cd and Pb increase as we increase the concentration of these magnetic elements. This is contrary to the fact that a reduction in coordination enhances the magnetic moment. We find that the trend that a lower concentration of magnetic elements giving a higher moment diminishes as one goes from Fe to Co to Ni. In fact, for Ni alloys (Fig. 4.14) this trend gets reversed: with the exception of Pt, the moments of the Ni alloys with all other nonmagnetic elements increase with the concentration of Ni. However, this is strictly true for the Cd and Pb only; for the Ag and Au,

this increase is very small. That is, for the Ni alloys with Ag and Au, the change in magnetic moment with changing the concentration is very small. Co shows an intermediary behavior between the Fe and Ni. Thus, the effect of alloying with a nonmagnetic element on the magnetic moments is different for Fe, Co and Ni. In general, we can say that a lower concentration (also coordination in our case) of Fe in its alloys enhances its magnetic moment while for the Ni, the behavior is opposite. However, we should keep in mind that alloying with different nonmagnetic elements may behave differently.

Interestingly, the $x = 0.33$ composition for the $(\sqrt{3} \times \sqrt{3})$ structure shows a dip in the magnetic moments of the Pt (with all the three magnetic elements) and Pb (with Fe and Co) alloys, whereas this composition corresponds to the highest moment for the Ag alloys (with Fe and Co). The two different structures (i.e., $\sqrt{3} \times \sqrt{3}$ and 3×1) for $x = 0.33$ as well as for $x = 0.67$ show different magnetic moments. For the alloys of Ag, Au and Cd with Fe and Co, the moments corresponding to the (3×1) structure are always lower than the $(\sqrt{3} \times \sqrt{3})$ structure. For the Pb alloys, it is always the opposite: the magnetic moments for the (3×1) structure are higher than for the $(\sqrt{3} \times \sqrt{3})$ structure. For Pt alloys, the moments are composition dependent: $x = 0.33$ composition gives higher moment for (3×1) structure whereas $x = 0.67$ composition gives higher moment for $(\sqrt{3} \times \sqrt{3})$ structure. Comparing the moments for the two structures (2×2 and 4×1) for the $x = 0.25$, $x = 0.50$ and $x = 0.75$, we find the following trends: for the Fe alloys with all the nonmagnetic elements, the magnetic moments are higher for the (2×2) structures than the (4×1) structures, whereas for the Ni alloys, this is true only with the Pt: with all other nonmagnetic elements,

the Ni alloys show higher moments for the (4×1) structure. For Co alloys with Pt, Au and Ag, the (2×2) structures show higher moments whereas for Co-Pb, the (4×1) structures show higher moments. For Co-Cd this is composition dependent. Thus, although the magnetic moments of checkerboard and stripe structures show different behavior depending upon the alloy component and composition, we can say in general that for most of the alloys, the checkerboard structures show higher magnetic moments compared to the stripe phase structures. This is particularly true for Fe and Co alloys (except for some compositions with Pb).

Among the nonmagnetic elements, alloys of Pt, Ag and Au show relatively higher moments than those of Pb and Cd. In fact, for small concentrations of Ni, the two nonmagnetic elements (Pb and Cd) show no magnetic moment. However, the overall trend in magnetic moments with respect to nonmagnetic elements is found to follow the order: $\text{Pt} > \text{Ag}, \text{Au} > \text{Cd} > \text{Pb}$. Alloying with Pb has a significant lowering effect on the magnetic moments. Note that the magnetic behavior of Ag and Au alloys is very similar.

4.7.5 Discussion on Magnetic Behavior

The fact that even the bulk-nonmagnetic transition metals can become magnetic in reduced coordination and dimensionality or in the presence of magnetic impurities around them, led us to investigate the possible existence of this induced moment on the otherwise nonmagnetic components of the surface alloys. Therefore, in order to understand what the sources of this

enhancement or reduction in magnetism are, we first separate out the contribution to the total magnetic moment from the magnetic element and the induced moments on the nonmagnetic elements. This is done by projecting out the spin polarized wavefunctions of the system onto the atomic states of the individual atoms. In Figs. 4.15-4.17, we have shown the contribution to the magnetic moment from the magnetic atoms (Fe, Co and Ni) alone. For Fe alloys (Fig. 4.15) with Pt, Ag and Au, the magnetic moment of Fe ($M(\text{Fe})$) follows the same trend as the total magnetic moment, M_{tot} . However, the variation of the $M(\text{Fe})$ for the Cd alloys is opposite to that of the M_{tot} : it increases with increasing the concentration of Fe atom (green symbols in Fig. 4.15). For Co (Fig. 4.16) and Ni alloys (Fig. 4.17), the magnetic moments on Co ($M(\text{Co})$) and Ni ($M(\text{Ni})$) increase with x . Thus the variation of $M(\text{M})$ with x does not follow the variation of M_{tot} for many alloy systems (e.g., Fe-Cd, Co-Pt, Co-Ag, Co-Au and Ni-Pt). This suggests that there are significant contributions to M_{tot} from the nonmagnetic and substrate atoms as well. In Fig. 4.18, we have shown the difference between the M_{tot} and the $M(\text{M})$ i.e., the contributions to the magnetic moments from the components other than the magnetic ones. We see that there are significant contributions coming from the substrate as well as the nonmagnetic components of the surface alloys. In almost all the alloy systems, the alloys with Pt seem to contribute the maximum towards the total magnetic moment. We further separate out the contribution from the other elements into one coming from the nonmagnetic component of the alloys and one coming from the substrate. In Fig. 4.19 we have shown the variation of induced moments on the nonmagnetic components of the surface alloys. We see that apart from Pt atoms,

there are considerable moments induced on the Pb and Cd atoms also. There seems to be no systematic variation of this induced moment with the concentration x . However, we find that while the induced moments on Pt are coupled ferromagnetically, giving rise to a net high moment in its alloys, the induced moments on the Pb and Cd show an antiferromagnetic coupling with the magnetic atoms, thereby reducing the net magnetic moment of their alloys. We find that in these two elements, a significant contribution to spin polarization comes from the p states which are oppositely polarized to the d states of the magnetic elements.

The magnetic moments induced on M obtained from the two different structures ($\sqrt{3} \times \sqrt{3}$ and 3×1) show more or less the same behavior as M_{tot} . However, the significant drop in the moments (total as well as induced) of Pb alloys for the $x = 0.33$ concentration in the ($\sqrt{3} \times \sqrt{3}$) structure is quite intriguing. The atomic arrangements for the $x = 0.33$ concentration for the two structures are quite different (see Fig. 4.1). The ($\sqrt{3} \times \sqrt{3}$) structure give rise to a pattern where a magnetic atom is surrounded by six nonmagnetic atoms, whereas in the (3×1) cell we have linear chains of magnetic and nonmagnetic atoms. Bonding with Pb diminishes the magnetic moments of Fe [185]. There are more (six) Fe-Pb bonds in the ($\sqrt{3} \times \sqrt{3}$) structure than in (3×1) (four). We find that the $x = 0.33$ composition corresponding to the (3×1) structure is energetically more favored when atoms are placed at hcp sites than when at fcc sites, whereas for the ($\sqrt{3} \times \sqrt{3}$) structure, the fcc site is favored over the hcp site. As the moments corresponding to fcc stacking are always lower than for hcp stacking, we get a lower moment for the $x = 0.33$ composition corresponding to the ($\sqrt{3} \times \sqrt{3}$) structure.

Figure 4.15: The variation of the average magnetic moment of Fe (in μ_B per Fe atom) in Fe alloys, with concentration x . Filled and unfilled symbols refer to checkerboard (CB) and linear stripe (LS) structures respectively. Stars denote the $x=0.5$ composition of the (2×1) cell.

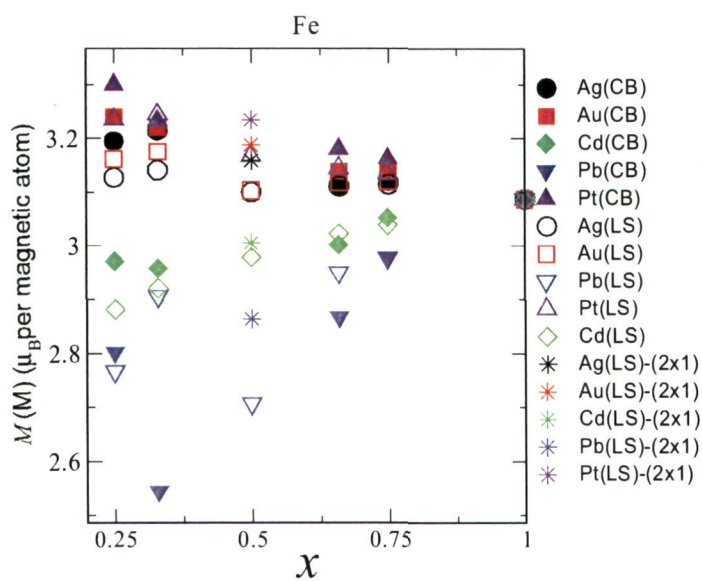


Figure 4.17: The variation of the average magnetic moment of Ni (in μ_B per Ni atom) in Ni alloys, with concentration x . Filled and unfilled symbols refer to checkerboard (CB) and linear stripe (LS) structures respectively. Stars denote the $x=0.5$ composition of the (2×1) cell.

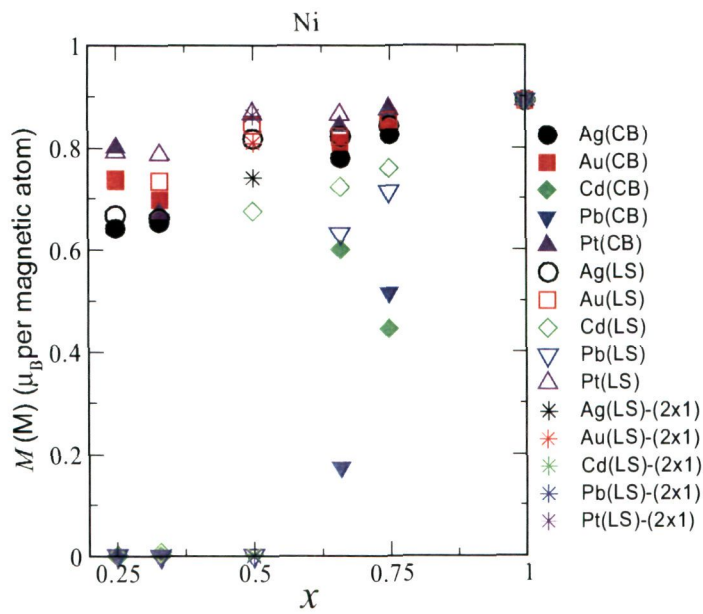


Figure 4.18: The magnetic moments (in μ_B per magnetic atom) plotted as the difference between the total moment (M_{tot}) and the moment on the magnetic atoms ($M(M)$), with respect to the concentration x , for (a) Fe-alloys, (b) Co-alloys and (c) Ni-alloys. Filled and unfilled symbols refer to checkerboard (CB) and linear stripe (LS) structures respectively. Stars denote the $x=0.5$ composition of the (2×1) cell.

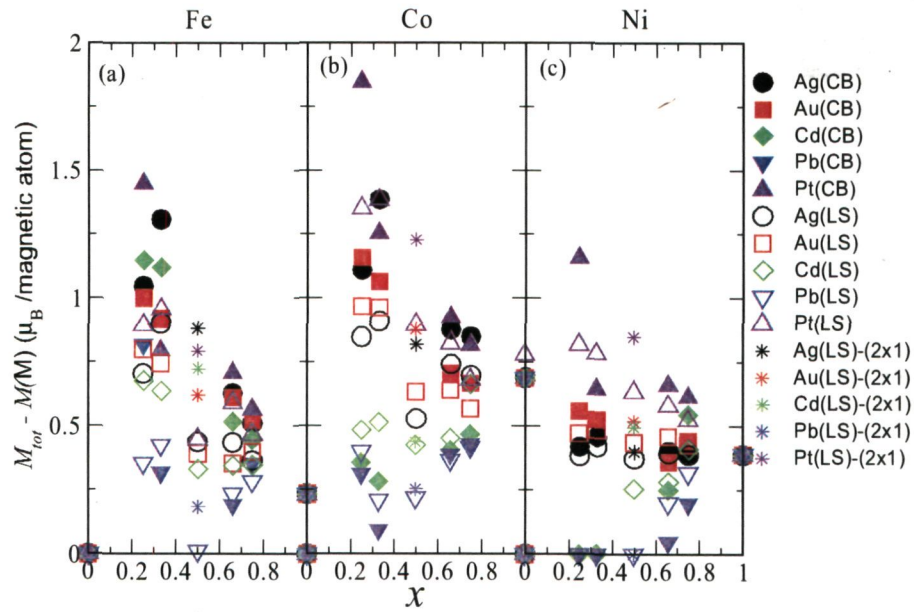


Figure 4.19: The variation of the induced magnetic moments (in μ_B per magnetic atom) of the nonmagnetic surface alloy atoms, $M(N)$, with the concentration x for (a) Fe-alloys, (b) Co-alloys and (c) Ni-alloys. Filled and unfilled symbols refer to checkerboard (CB) and linear stripe (LS) structures respectively. Stars denote the $x=0.5$ composition of the (2×1) cell.

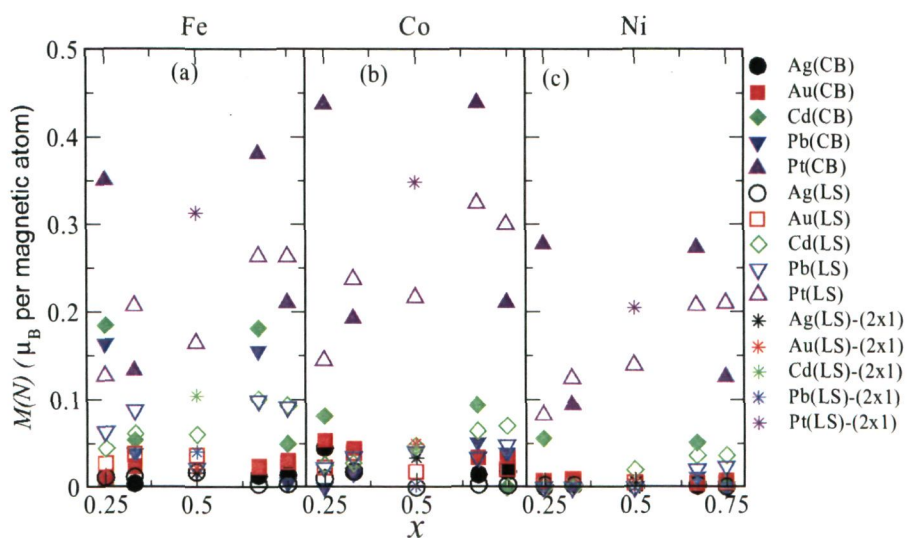
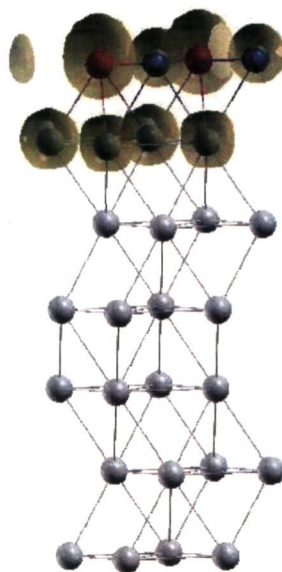


Figure 4.20: Spin-polarized charge density isosurface for $x = 0.5$ Fe-Pt alloys (for the 2×2 cell). The isosurface corresponds to a charge density of 0.07 electrons/ \AA^3 . Red, blue and grey solid spheres denote Fe, Pt and Rh atoms respectively. The spin-polarized charge density around the Fe as well as the Pt and the top substrate layer atoms can be clearly seen.



In Fig. 4.20 we have shown an isosurface of spin polarized charge density (i.e., the difference of the spin-up and spin-down charge densities) for the Fe-Pt system. Besides Fe atoms (red sphere), the large magnetization density around Pt (blue sphere) and the (top layer) substrate atoms (grey spheres) shows significant induced moments on these elements. Among non-magnetic atoms, Pt acquires highest induced magnetic moment (up to $0.4 \mu_B$) and is always ferromagnetically coupled to the magnetic elements. The high moments of Pt alloys can be attributed to the high induced moments on Pt atoms.

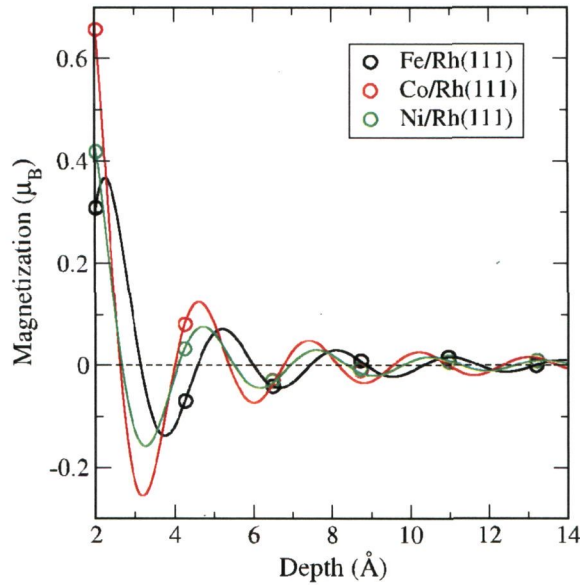
As mentioned earlier in Sec. 4.7.3, there are considerable magnetic moments induced on the substrate atoms also. The variation of the induced moments on the substrate atoms as a function of the distance from the top layer is particularly interesting. Fig. 4.21 shows the variation of induced magnetic moments on the substrate layers for the monolayers of Fe, Co and Ni. The weak oscillatory nature of the magnetization (similar to the Rudermann-Kittel-Kasuya-Yoshida (RKKY) type interactions [186]) is described by fitting the data points with the oscillatory function [104]:

$$\mu(z) = \mu_0 \frac{\sin(2qz + \phi)}{(2qz)^2}. \quad (4.13)$$

In the above equation, μ refers to the induced magnetic moment on an atom at a distance z away from the magnetic atom, and q and ϕ are a wavevector and phase that are determined by fitting. Interestingly, the induced moments on the first substrate layer is highest ($0.66 \mu_B$) when the overlayer is Co rather than Fe. In fact, the moment on the first Rh(111) layer induced by a Fe monolayer ($0.33 \mu_B$) is lower than even the one induced by a Ni monolayer ($0.42 \mu_B$). The first Rh(111) layer is coupled ferromagnetically to the magnetic atom in the top layer; while the second Rh layer is coupled ferromagnetically for the monolayers of Co and Ni; the Fe monolayer induces an antiferromagnetic ordering in this layer. The third layer couples ferromagnetically with all the three monolayers. However, it should be noted that these induced moments become very small beyond the first substrate layer.

We find that in these two elements (Cd and Pb), a significant contribution to

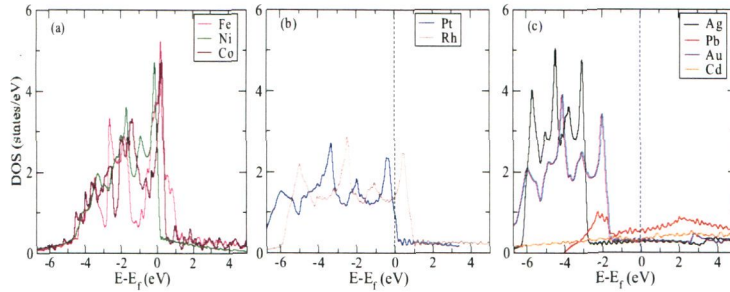
Figure 4.21: Behavior of induced moments for monolayers of $M/\text{Rh}(111)$: the oscillatory decay of the induced magnetization (in μ_B per magnetic atom) of the substrate layers with their distance from the top magnetic monolayer (Fe, Co and Ni). Solid lines are the fits by the expression described in the text (Eq. 4.13). Circles are the data points.



spin polarization comes from the p states which are oppositely polarized to the d states of the magnetic elements. This causes the observed low moments in their alloys.

Now the question is why the induced moments and the moments on the magnetic atoms change with concentration in the observed way. This we would explain below using the density of states analysis and a simple Stoner like argument. We have performed non spin-polarized (NSP) density of states calculations for our surface alloy systems. First, we asked the question whether

Figure 4.22: Non-spin-polarized density of states (DOS) of the (a) magnetic, (b) the substrate and Pt and of (c) Au, Ag, Cd and Pb elements in their bulk phase. Note the high $DOS(E_f)$ for magnetic elements. Among the nonmagnetic elements, Pt shows the highest $DOS(E_f)$.



the trends in magnetism of surface alloys can be understood from the properties of their bulk constituents. We calculated the NSP DOS for all bulk elements and interestingly we got the following trends: the magnetic elements Fe, Co and Ni give high $DOS(E_f)$, Pt and the substrate element Rh give medium $DOS(E_f)$ while Ag, Au, Pb and Cd give relatively low DOS at the Fermi level. These results are shown in Fig. 4.22. This (loosely) suggests that the elements which have high NSP $DOS(E_f)$ in their bulk phase would give rise to high magnetic moment in their low dimensional state. Thus, the high moment of Pt-alloys is a result of its high $DOS(E_f)$.

The NSP $DOS(E_f)$ for surface alloy systems and its correlation with magnetic moment can be seen in Fig. 4.23. For most of the elements, a high NSP $DOS(E_f)$ corresponds to a high magnetic moment. As we already observed, the behavior of magnetic moments of Cd and Pb alloys with Co and Ni is different from the rest of the alloys. In Fig. 4.24 we have shown the DOS of the d -bands of Fe alloys for all compositions. It can be seen that for Fe alloys, d -states are peaked near the Fermi level for $x = 0.25$. As one increases the

Figure 4.23: Total magnetic moment, M_{tot} (in μ_B per magnetic atom), versus the total non spin-polarized density of states (at E_f) per magnetic atom for (a) Fe, (b) Co and (c) Ni alloys for the four compositions ($x=0.25, 0.50, 0.75, 1.0$) of the (2×2) cell. The points where all the curves meet corresponds to $x=1.0$.

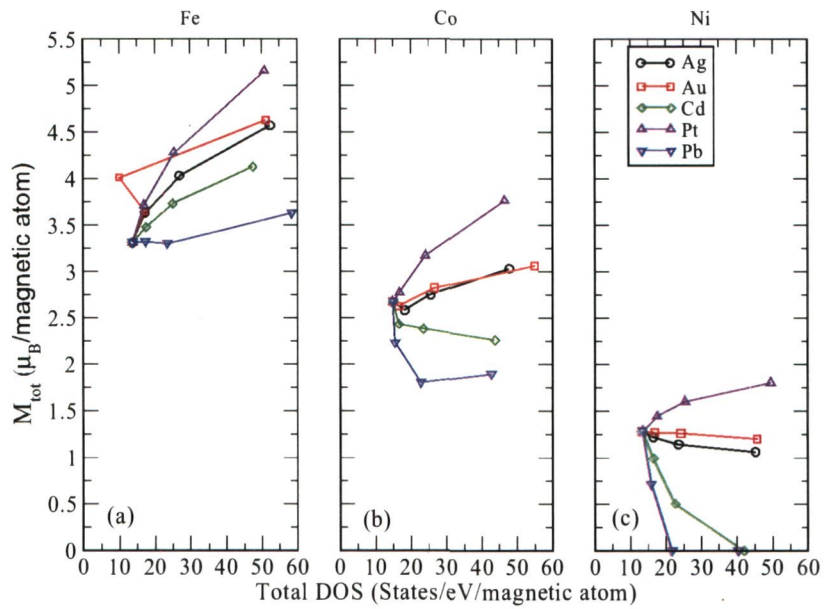
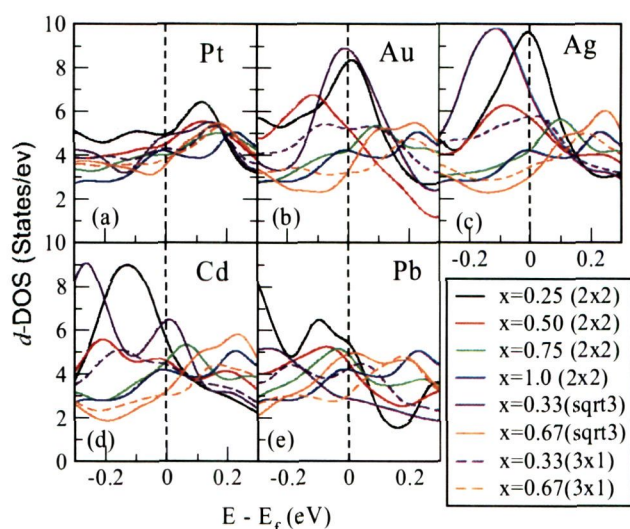


Figure 4.24: d density of states (states/eV) of Fe atom in its surface alloys for different compositions and structures: (a) for Fe-Pt, (b) for Fe-Au, (c) for Fe-Ag, (d) for Fe-Cd and (e) for Fe-Pb. The dashed vertical lines indicate the positions of the Fermi levels.



concentration of Fe atoms, the height of the peak reduces. The single peak splits into two distinct peaks as one goes from $x = 0.25$ to $x = 1.0$, increasing the total width of the d -bands. As can be seen from the projected DOS on atomic d -orbitals (see Fig. 4.25), the main contribution comes from the d_{z^2} orbitals of Fe. The orbitals are more localized for $x = 0.25$, particularly the d_{z^2} orbital, and with increasing the concentration of magnetic element, they get broadened.

While the broadening of the d -band with increasing concentration of magnetic atom is a general feature seen in all the magnetic alloys, it is the position of the Fermi level with respect to the band peaks which determines the

Figure 4.25: Density of states of the five d orbitals of Fe atom in (a) $\text{Fe}_{0.25}\text{Ag}_{0.75}/\text{Rh}(111)$, (b) $\text{Fe}_{0.75}\text{Ag}_{0.25}/\text{Rh}(111)$, (c) $\text{Fe}/\text{Rh}(111)$ (Fe monolayer) and (d) bulk Fe. The dashed vertical lines indicate the positions of the Fermi levels.

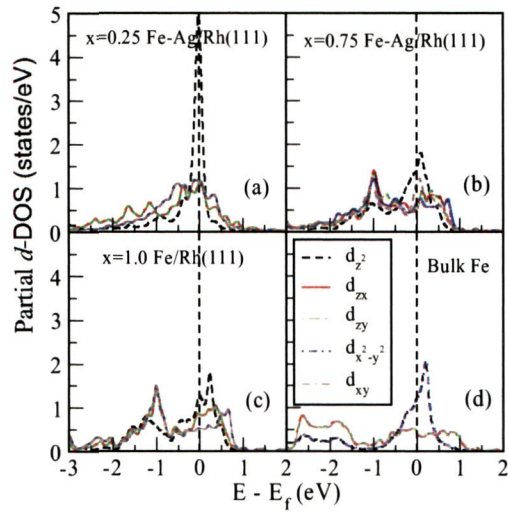
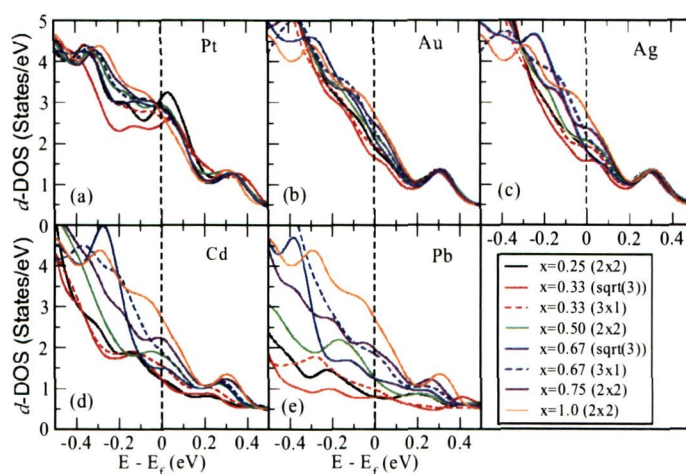
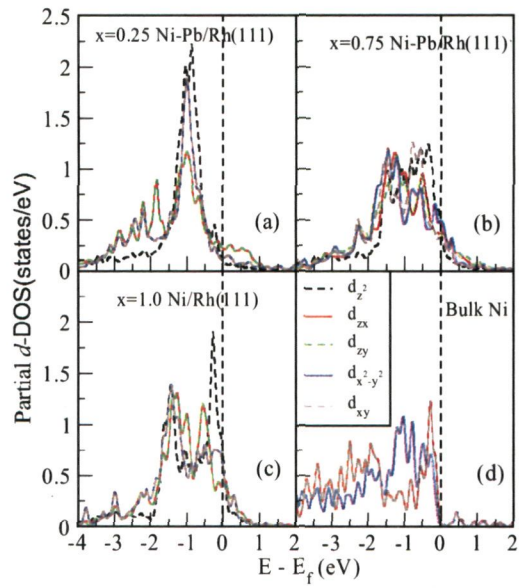


Figure 4.26: d density of states (states/eV) of Ni atom in its surface alloys for different compositions and structures: (a) for Ni-Pt, (b) for Ni-Au, (c) for Ni-Ag, (d) for Ni-Cd and (e) for Ni-Pb. The dashed vertical lines indicate the positions of the Fermi levels.



magnetic moments. If we compare, for example, the DOS structures of Ni-Pt and Ni-Cd surface alloys (see Fig. 4.26), we observe that in the case of Ni-Cd, the Fermi level is shifted more towards the right, making the DOS at E_f smaller. Since the number of valence electrons is more in Cd (12) than Pt (10), addition of Cd would push the Fermi level further away from the peak positions, making the $\text{DOS}(E_f)$ smaller. A similar argument holds for Ni-Pb surface alloys also (see Fig. 4.27) as Pb has even more number of valence electrons (14). The same holds for the Pb and Cd alloys of Co also. Therefore, the opposite behavior of the magnetic moments of Cd and Pb alloys with Co and Ni when compared to the rest of the surface alloys is due to the higher number of valence electrons in them and the position of the Fermi levels in Co and Ni. For Fe alloys, the Fermi level lies well within

Figure 4.27: Density of states of the five d orbitals of Ni atom in (a) $Ni_{0.25}Pb_{0.75}/Rh(111)$, (b) $Ni_{0.75}Pb_{0.25}/Rh(111)$, (c) $Ni/Rh(111)$ (Ni monolayer) and (d) bulk Ni. The dashed vertical lines indicate the position of the Fermi level.



the d -band and falls on the DOS peaks (see Fig. 4.25). Since Fe has less valence electrons than Ni, the shift in the Fermi level caused by the addition of even Cd or Pb does not cause it to lie outside the d -band peak. Thus, the $\text{DOS}(E_f)$ in the case of Fe alloys is mainly affected by the change in the band broadening.

So, the change in the magnetic moment with changing concentration is affected by two factors: (1) the broadening of the d -band and (2) the position of the Fermi level. Increasing the concentration of a magnetic atom (replacing a nonmagnetic atom) results in broadening of the d -band and thus reducing the peak height and consequently lowering the $\text{DOS}(E_f)$, while the accompanying change in the number of electrons shifts the Fermi level. For a given change in the concentration, if the resulting change in the band broadening is dominated by the change in the total number of valence electrons, giving rise to a larger shift in the position of the Fermi level, the $\text{DOS}(E_f)$ and hence the magnetic moment is affected more by this shift than by the d -band broadening.

As we have seen, with a given magnetic element and for a given concentration, the magnetic moment of the surface alloys decreases in the order $\text{Pt} > \text{Ag}$, $\text{Au} > \text{Cd} > \text{Pb}$. We find that this order correlates with the number of valence electrons in them. There are 10, 11, 11, 12 and 14 valence electrons in Pt, Ag, Au, Cd and Pb respectively. If we look at the number of valence electrons in these nonmagnetic elements, we find exactly the same order: as the number of electrons increases the moments decreases. We believe this is because as the number of electrons increases, for a given M and x , the Fermi level moves towards higher energy values, away from the non-spin-polarized DOS peaks,

thereby reducing the $\text{DOS}(E_f)$.

Effective Coordination Number

It would be interesting to know how these trends in magnetic moments relate with the coordination number of magnetic atoms in the alloy. As is known, a reduced coordination enhances moment as a result of increased $\text{DOS}(E_f)$ [187, 188]. To the simplest approximation, the $\text{DOS}(E_f)$ is inversely proportional to the bandwidth. A smaller coordination number means a smaller d - d hybridization and that in turn gives rise to a narrower bandwidth thus favoring the tendency towards ferromagnetism. The enhanced magnetism at surfaces compared to bulk is thus attributed to the reduction of coordination number at the surfaces. In the same way the magnetism of ultrathin films and one-dimensional nanowires is further enhanced compared to its value at surfaces [189].

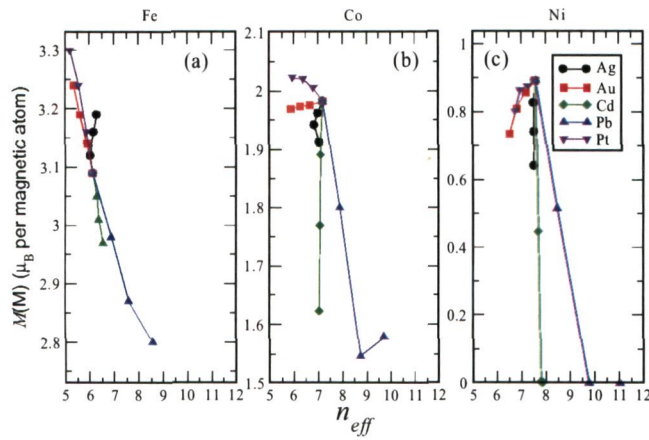
The coordination number of an atom in its bulk environment is the number of its NNs. For example, in Fe and Ni, which have the body-centered cubic and face-centered cubic structures respectively, the number of first NNs is eight and twelve respectively. However, in a different structural and chemical environment, such as in the surface of a two-dimensional structure on a different substrate, the definition of the coordination number needs to be modified. In any system, the equilibrium interatomic distances of atoms are determined by electronic and ionic interactions that set an optimum charge density profile around each atom consistent with the minimum energy configuration. In the bulk, the presence of high symmetry leads to a simple charge density variation in the sense that all the neighboring atoms are of the same

type and hence the total charge density around a given atom can be taken as a multiple of the charge density contributed by a single neighboring atom alone. However, in a complex system of reduced symmetry like surface alloys, the total charge density around an atom is contributed by different types of neighbors placed at different distances. In such a case, one can define what is called the *effective* coordination number, n_{eff} , given by [190]:

$$n_{eff}(i) = \sum_j \rho_j^{at}(\mathbf{r}_{ij}) / \rho_i^{at}(\mathbf{r}_{bulk}). \quad (4.14)$$

The n_{eff} of a given atom i , in an alloy is the total charge density on that atom relative to the charge density in its bulk. The sum is calculated over all the neighbors j of atom i , $\rho_j^{at}(\mathbf{r})$ is the calculated spherical charge density distribution of an isolated atom j as a function of the distance r from the origin (nucleus), \mathbf{r}_{ij} is the distance of the j NN from the i atom and \mathbf{r}_{bulk} is the bulk interatomic distance. A n_{eff} of an atom greater (lower) than its bulk value indicates that charge density on that particular atom in the given alloy composition is more (less) compared to what it had in its equilibrium bulk structure. In this calculation we have used charge densities of pseudo atoms. Since pseudo wavefunctions (and hence the charge densities) near interatomic distances are identical to the corresponding all-electron values, calculation of n_{eff} using pseudo charge densities is not affected by this (pseudo) approximation. In Fig. 4.28 we have plotted the n_{eff} of all the three magnetic atoms in surface alloys for all the compositions of (2×2) cell versus their magnetic moment. As can be seen from Fig. 4.28, the effective coordination number of Fe atoms correlates well with its magnetic moment:

Figure 4.28: Magnetic moment of magnetic elements, $M(M)$, versus the effective coordination number, n_{eff} , for (a) Fe, (b) Co and (c) Ni alloys, for the four compositions of a (2×2) cell: $x = 0.25, 0.5, 0.75, 1.0$. The point where all curves meet corresponds to $x = 1.0$.



the lower the n_{eff} , higher the moment. But it is not very well correlated with the moments of Co and Ni alloys. However this need not be true in all cases, as the calculation of this effective coordination number is based on the simple assumption that the charge density in the solid is the sum of atomic charge densities.

4.8 Summary

The mixing behavior of various two-dimensional binary magnetic alloys of the type $M_x N_{1-x}$ ($M = \text{Fe, Co, Ni}$; $N = \text{Pt, Au, Ag, Cd, Pb}$; and the concentration $x = 0.0, 0.25, 0.33, 0.5, 0.67, 0.75, 1.0$) on Rh(111) substrate has been studied. We have considered two types of structures for each composition:

(1) linear stripe type (corresponding to 2×1 , 3×1 and 4×1 cells) and (2) mixed checkerboard type (corresponding to 2×2 and $\sqrt{3}\times\sqrt{3}$ cells). Some of these pairs are immiscible in their bulk phase. We find that the mixing if allowed only in two dimensions can be different from that in the usual three dimensions. Except the alloys of Ag, all other bulk immiscible pairs show significant mixing on the Rh(111) surface. An important contribution to this enhanced mixing comes from the elastic interactions brought about by the surface confinement. Consequently, the alloys of Pb, which in spite of having a large size mismatch and hence predicted by the first Hume-Rothery rule to be bulk immiscible, show a rather large enthalpy of mixing.

However, we find that the “effective sizes” on the surface can be different enough to alter the mixing. Alloys of Cd, for example, show little contribution to the mixing from the elastic interactions in spite of having large size mismatch (if the bulk-phase sizes are taken). The effective atomic size of Cd on Rh(111) surface is found to be so different from its bulk value that the Cd monolayer is actually under tensile stress instead of compressive stress, and the energy minimization achieved through the stress relaxation becomes small. The disfavored mixing of Ag alloys is dominated by the unfavored chemical interaction between Ag and the magnetic constituents of the alloys. The presence of magnetism also affects mixing. This effect is most pronounced in Fe alloys due to its larger magnetic moment. While the presence of magnetism lowers the mixing of Pt alloys, it helps the mixing of Pb alloys. This could be due to the reason that the magnetic interactions in a way try to expand the system. This we confirm by our finding that the surface NN distance of magnetic elements is lower when spin polarization

is turned off. Different structures (linear stripe versus mixed checkerboard type) are affected differently by the presence of magnetism. This is due to the possibility of different ways of relaxation in these two types of structures. Apart from studying the effect of magnetism on the mixing, we have also calculated magnetic moments of the surface alloys, their contributions from the local moments and from the induced moments on the substrate and the nonmagnetic elements. We find that in general for Pt, Au and Ag alloys, the total magnetic moment per magnetic atom goes up as one decreases the concentration of magnetic element. This behavior is more pronounced with Fe and Co but less with Ni alloys. The total moments (per magnetic atom) of Cd and Pb alloys on the other hand in general decrease as one decreases the concentration of magnetic elements. This trend also is affected by the alloy structures (linear chain vs mixed checkerboard type).

In general, for a given composition and with a given magnetic element, we find that the magnitude of the magnetic moments of the surface alloys with different nonmagnetic elements follow the order: Pt > Ag, Au > Cd > Pb. However, the high moment of Pt-alloys are contributed significantly from the induced moments on Pt atoms. We find that this order of moments directly follows from the number of electrons treated as valence electrons in these nonmagnetic elements: greater the number of valence electrons, the lower the moment. Ag and Au have the same number of valence electrons and their moments are also quite the same.

It should be mentioned that this work is only a preliminary step towards understanding the electronic and magnetic properties of the corresponding real systems. We have considered only a small number of simple phases; the

real experimental structures, affected by various other parameters such as synthesis mode and temperature, need not be one of these. Though we still lack a complete understanding of the observed behavior, our findings would indeed guide the experimentalists to narrow down their hunt for systems with enhanced properties. Based on our calculations we predict that the surface alloys of Fe and Au on Rh(111) are promising candidates for magnetic data storage materials and thus worth experimental investigation. We also caution that although the magnetic surface alloys of Pt show desirably large magnetic moments, they might not be suitable for magnetic data storage. In Chapter 7, we have listed further open questions relevant to the work presented in this chapter.

Chapter 5

Structural and Magnetic Anisotropy of Self-Assembled Monolayers (Methanethiolate) on Co/Au(111)

5.1 Introduction

Self-assembled monolayers (SAMs) of amphiphilic organic molecules on metal or non-metal surfaces have become an area of intense research in material science due to their properties that are useful in diverse fields ranging from surface chemistry to optics to electronics [191–193]. The molecule generally has a chain like structure that consists of a hydrophilic “head group” at one end that shows a special affinity for a substrate, and a hydrophobic functional

(tail) group at the other end connected by a backbone of alkyl chain. The hydrophobic tail groups assemble away from the substrate while the hydrophilic head groups assemble together on the substrate, resulting in a close-packed area covering the substrate with a single monolayer (see Fig 5.1). SAMs are particularly stable due to the strong chemisorption of head groups. The possibility to introduce a wide range of terminal functional groups provides a versatility of surface properties. Alkanethiols (R-SH, where R = aliphatic chain), the most commonly used molecules for SAMs, are molecules with an alkyl chain (R-) as tail group, and thiol (-SH) as head group. Since the first finding of disulfides and thiols self-assembling on gold [194] and subsequent pioneer work of Brust *et al.* [195], alkanethiols have been widely used to prepare nanocrystals by controlled self-assembly of nanoparticles. Self-assembly of thiols on gold has, during the last decades, shown great promise in the creation of functional nanomaterials, such as sensors and catalysts. Magnetic nanocrystals such as PtFe and PdNi have also been assembled using long chain alkanethiols [196,197].

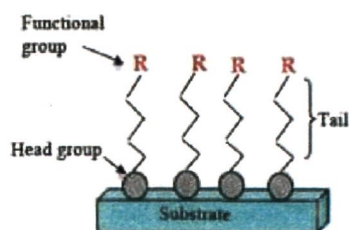
Thiol-metal bonds are particularly strong making these SAMs stable over a wide range of temperature, and in a wide variety of solvents and electromagnetic fields [198]. A large amount of experimental as well as theoretical work has been devoted to understanding the adsorption phase structure and interface bonding of these molecules on metal substrates. Alkanethiols on Au(111) have been extensively studied due to the desirable features of gold as a substrate: it is inert, easy to pattern via lithographic techniques, biocompatible and can withstand harsh chemical cleaning treatments. Also, the sulfur in thiols has a strong affinity for noble metals.

Although gold has been the most popular substrate for thiol SAMs, ferromagnetic substrates have also been studied for their potential spintronics applications [199–201]. Xiong *et al.* [199] observed a large magnetoresistance for a spin-valve system consisting of an organic semiconducting layer sandwiched between two ferromagnets, generating huge interest in organic spintronics. The magnetoresistance was shown to be tunable by mixing the organic polymer with a large spin-orbit-coupling molecule [202].

One of the most interesting features of the thiol capped Au nanoparticles and thin-films is the appearance of room temperature ferromagnetism. This ferromagnetism is somewhat unconventional as the magnetization remains almost temperature independent up to room temperature. Although the appearance of magnetism has been largely associated with spin of $5d$ localized holes as a result of the charge transfer from gold to sulfur of thiol molecule [203,204], its complete understanding is still lacking.

The appearance of stable ferromagnetism even at room temperature has been observed in thiol–semiconductor systems also [204–206]. The fabrication of dilute ferromagnetic semiconductors, which is traditionally done through doping ferromagnetic elements into semiconductors, is also being replaced

Figure 5.1: Schematic representation of a self-assembled monolayer (SAM) on a substrate (from wikipedia).



by the fabrication of thiol-semiconductor systems which are much easier to synthesize.

Co/Au(111) multilayers were the first system where giant magneto resistance (GMR) was found with perpendicular magnetic anisotropy [207]. The magnetic anisotropy of Co films on Au(111) has been found to be dependent on the Co thickness [208–210]: a reorientation of magnetization direction from out-of-plane (at small Co thickness) to in-plane (at large thickness) has been observed for film thickness between 3–5 monolayers. The effect of capping Co/Au(111) with Au layers has been found to delay this thickness dependent easy axis switching as well as to increase the MAE value [211]. It would be interesting to study the magnetic anisotropy properties of Co/Au(111) with organic molecular layers as cappings.

Our work has been motivated by experiments done in the group of Sylvie Rousset where they found a switch of the easy axis from in-plane to out-of-plane after putting dodecanethiols ($C_{12}SH$) on 4.5 monolayer (ML) of Co films on Au(111) [212]. 4.5 ML thick Co films on Au(111) are just above the critical thickness (of ~ 4 ML) where a spin reorientation transition (SRT) from out-of-plane to in-plane takes place. Although there have been a number of studies of the changes in the geometry, and a few studies on magnetism [213] induced by alkanethiols in gold surfaces and clusters, to our knowledge no theoretical studies have yet focused on the magnetic anisotropy of thiol/Co/Au(111) system.

The experimental studies of thiols or thiolates on Au surfaces are typically done using long-chain molecules. However, calculations become increasingly expensive the longer the aliphatic chain, and so calculations are often done on

truncated chains. Previous calculations have shown that the binding energy changes very little upon changing the length of the chain [214], though at least one carbon atom is necessary in order to describe the sulfur-gold binding correctly [215].

The rupture processes of single alkanethiols and alkanethiolates (R-S) from gold surfaces measured by means of atomic force microscopy experiments [216] suggest a covalent nature of the sulfur-gold bonds. Therefore, semi-empirical atomistic calculations based on simple potential models will be unable to correctly describe these molecule/metal systems and hence a first-principles quantum mechanical (electronic structure) calculation is required. In this chapter we have studied the structural and magnetic properties and magnetic anisotropy energies of methanethiolate on Co/Au(111) using density functional theory (DFT) within the fully-relativistic ultrasoft pseudopotential and plane wave basis formalism, as implemented in the Quantum ESPRESSO distribution [175]. We have done a detailed study of the structure of the Co/Au(111) and methanethiolate adsorbed Co/Au(111) systems. We have calculated the change in MAE of the Co/Au(111) system after putting methanethiolate on it. We might hope, due to the anisotropic structure of the molecule, to see a considerable enhancement in the magnetic anisotropy energy of the thiolated Co/Au(111) compared to the clean Co/Au(111) substrate.

5.2 Further Details of Previous Work

5.2.1 Co/Au(111)

Since the first observation of perpendicular magnetization anisotropy in Au/Co/Au(111) sandwiches by Chappert *et al.* [217], and the subsequent investigation of structure using scanning tunneling microscopy on the growth of Co on Au(111) [218], this system has been extensively studied. Thin Co films on Au(111) exhibit perpendicular magnetic anisotropy [217] and a switching of the magnetization from out-of-plane to in-plane occurs at a critical thickness between 14 and 19 Å [208, 219]. However, this spin-reorientation transition has been found to depend on the growth mode also: at high deposition rates of cobalt, out-of-plane magnetization is found to be stabilized in the thickness range from 2 to 8 atomic layers while low deposition rates were observed to favor in-plane magnetization at any thickness [220]. It has been observed experimentally that on the Au(111) surface, the stacking of the cobalt films for thicknesses above 4 ML is hexagonal closed packed (hcp) with the c axis perpendicular to the Au(111) plane, and the Co does not grow pseudomorphically, presumably due to the large lattice mismatch (14%) between the two materials [221]. The x-ray absorption spectroscopy studies [221] suggest a hexagonal stacking for Co films thicker than 4 ML, and the analysis of the first-nearest-neighbor shell shows that this hexagonal structure is very close to that of the bulk Co. This leads to an incoherent epitaxy at the interface with a wide radial distribution of Co-Au bonds [221]. Since the Co thin-film structure on Au(111) is very much bulk-like and the $\langle 0001 \rangle$ axis is perpendicular to the Au(111) surface, the easy-axis of magnetization may

be expected to be perpendicular to the surface (along the $\langle 0001 \rangle$ direction), as for the bulk Co. However, the anisotropy of a Co(0001) surface has been experimentally found to be in-plane [222].

The MAE of the Au capped pseudomorphic Co monolayer on Au(111) was first calculated by Szunyog *et al.* [211] using the KKR Green's function method and employing the so-called force theorem. For the bare Co monolayer (i.e., uncapped) on Au(111), they obtained an in-plane easy axis and only the spin-orbit contribution to the MAE was about 0.58 meV per Co atom. Capping Co/Au(111) with one monolayer of Au switched the easy axis to normal to the surface and increased the MAE to 1.58 meV per Co atom.

The phenomenological understanding of MAE and the easy axis is based upon models that relate the MAE to the atomic orbital moment [227]: the easy axis lies in the direction of the largest orbital moment. The spin reorientation transition has been understood in terms of the above model wherein the spin reorientation temperature (SRT) is associated with an increase in the orbital moment upon reorientation to the new easy axis. Although many experimental observations have been found to be consistent with this description, there are cases (e.g., Au/Co/Au trilayer system) where it has not been found so [228].

5.2.2 Thiols on Co(0001) and Au(111) and Au Nanoparticles

Self-assembled monolayers of alkanethiolates on gold are one of the most studied metal surface-adsorbate molecular systems. Extensive experimental investigations of the adsorption and desorption process of thiols of different chain lengths on several gold surfaces have been performed [191, 229–233]. A charge transfer from the metal to the thiol has been observed, showing the anionic nature of the adsorbate. When the adsorbate molecules are normal to the surface, the bonding between the adsorbate and the metal was found to be independent of the chain length [234].

Many studies have been carried out for thiols on Au clusters to model the thiol capped Au nanoparticles (see [214] and references therein). DFT studies on methanethiol and dimethyl disulfide on Au(111) surface have been performed by Grönbeck *et al.* [235] using gradient-corrected exchange-correlation functionals and a comparison of the structures, binding energy and type of bonding with local density functionals has been done. Structural and electronic properties of methanethiolate molecule on Au(111) and Co(0001) surfaces were studied [236–238] by employing DFT calculations. It was found that the bonding of CH₃S is stronger on the Co(0001) surface compared to the Au(111) surface, probably due to a greater charge transfer from Co to the molecule; the adsorption energy of CH₃S on Co(0001) is 2.5 eV higher than on Au(111). The charge transfer from Co to S is 0.22 e compared to 0.09 e for Au, while the S-Co bond length is shorter (2.22 Å) compared to the S-Au bond length (2.52 Å). The subsurface layers were found to be

nearly unaffected by the CH_3S adsorption for both the substrates. The three-fold hollow sites (fcc and hcp) were found to be the most stable for the CH_3S adsorption and the low coverage geometries [the $(\sqrt{3} \times \sqrt{3})$, (2×2) and (2×3)] were more stable and the S-C bond was normal to the surface. In another study, the adsorption of S atoms on the Co(0001) surface was investigated and a preference for the fcc hollow site was found [239]. Experimentally, the alkanethiols on Au(111) and Co(0001) are found to adopt a $(\sqrt{3} \times \sqrt{3})R30^\circ$ and (2×2) geometry respectively. Interestingly, the first-principles calculations of methanethiolate/Co(0001) [237] show nearly the same stability for the $(\sqrt{3} \times \sqrt{3})R30^\circ$ and (2×2) structures. However, for the adsorption of sulfur adatom on Co(0001), the (2×2) structure has been experimentally observed with LEED [240] and theoretically predicted to be the most stable [239].

Experimentally, the Co films show an out-of-plane magnetization up to a thickness of around 4 ML. For thicker films, a reorientation of magnetization from out-of-plane to in-plane occurs. Reorientation of the easy axis and the change in the MAE value for the Co/Au(111) system upon capping with organic layers (e.g., thiols) has not been studied theoretically to our knowledge. Although bulk Au as well as uncapped Au films and Au nanoparticles (NPs) are shown to be diamagnetic, permanent magnetism has been observed for Au films and NPs capped with self-assembled layers of alkanethiols [241–243]. The appearance of magnetic properties has been associated with the charge transfer from gold to sulfur of thiol molecules. The anisotropic (surface) structure resulting from the self-assembly of organic layers on the Au surface is supposed to be responsible for the large anisotropy in moments, giving rise

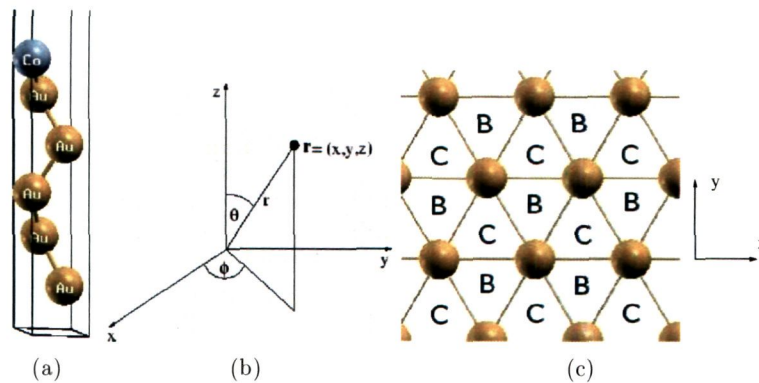
to a permanent magnetic moment and thus a ferromagnetic nature. Although the local anisotropy (in magnetic moments) is detected to be large for both alkanethiol capped films [242] as well as nanoparticles [244], the values of magnetic moments show different behavior: for films it reaches up to giant values of ~ 10 (or even ~ 100) μ_B per Au surface atom whereas for NPs, it is extremely low ($0.01 \mu_B$ per atom) [245]. The high magnetic moments observed in SAM/metal systems have been attributed to the existence of large orbital momenta [245] formed in the observed large size domains [233, 247, 248]. Electron circular dichroism measurements carried out on thiolated organic layers on Au show a uniform orbital momentum direction within each domain [249]. This long range orbital ferromagnetism could be responsible for the observed giant atomic magnetic moments, and can give rise to giant magnetic anisotropy in these systems [245].

To the best of our knowledge, there has been no previous theoretical study of the magnetic anisotropy of SAMs on magnetic surfaces on Au(111). All electron DFT calculations (using GGA) on small Au clusters by Ayuela *et al.* [213] on CH_3S adsorbed on small Au-clusters show a large MAE value of 1.43 and 0.98 meV per CH_3S molecule for Au_4 and Au_6 clusters respectively. While previously, the charge transfer was understood to be from the Au substrate to the sulfur, the authors [213] attribute the presence of magnetic moment to the transfer of sp^3 electrons from the sulfur to the Au atoms.

5.3 Our Calculations: System

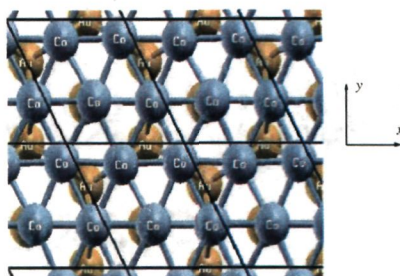
We started with the $\text{Co}_n/\text{Au}(111)$ system ($n=1$ to 5) considering a pseudomorphic geometry in a (1×1) surface unit cell at the calculated lattice constant of bulk Au (2.87 Å). The number of Au(111) layers was taken to be five. Fig. 5.2 shows the side view of the unit cell (truncated in the z -direction) for the 1 ML Co/Au(111) system and the three-fold hollow sites available at the (111) surface. If the atoms (yellow spheres) in Fig. 5.2 (b) are assumed to be occupying the “A” sites (not shown in the figure), there are two types of three-fold hollow sites, labeled as “B” (inside the down-pointing-triangles) and “C” (inside the up-pointing-triangles), available for the next layer atoms. If the atoms in the first two layers of any substrate occupy the A and B sites, the third layer atoms will have to be put either at A sites (and this will be called hcp site) or C sites (called fcc site). The structure of bulk Au and Co respectively are fcc and hcp, giving rise to a stacking sequence of atomic layers as ABCABC... in the $[111]$ direction of the fcc crystal and ABAB... in the $[0001]$ direction of the hcp crystal. We have considered two stacking sequences for the five layers of Au: (1) pure fcc stacking (i.e., ABCAB) and (2) four layers as fcc and the fifth (top) layer at hcp (i.e., ABCAC) stacking. The Co overlayers are considered in various stacking sequences possible for a given n (we have not considered *all* the possible stackings for a given n). Next, we considered non-pseudomorphic (i.e., reconstructed) Co layers on Au(111). As found experimentally, the thin-films of Co on Au(111) reconstruct: they assume their bulk structure (hcp) and interatomic distances due

Figure 5.2: (a) Side view of the 1 ML Co/Au(111) in (1×1) surface unit cell (the vacuum region above the Co atoms is truncated). (b) coordinate system defining the θ (polar angle) and ϕ (azimuthal angle). (c) The three-fold hollow sites on the fcc (111) surface. The two hollow sites labeled as “B” (inside the down-pointing-triangles) and “C” (inside the up-pointing-triangles) are shown with the atoms (yellow spheres) occupying the “A” sites (not mentioned in the figure).



to large size mismatch between Au and Co. Therefore, to study the real (experimental) structural properties, one would need to model Co/Au(111) in a much bigger unit cell, making it computationally very expensive for the *ab initio* calculations. However, one can make a clever choice of a smaller unit cell and achieve one aspect of the structure (the surface atomic densities) correctly, while sacrificing the correct interface structure. We have modeled Co/Au(111) using a $(\sqrt{3} \times \sqrt{3})$ surface unit cell consisting of five layers of Au(111) with three atoms per layer and three layers of Co with four atoms per layer (i.e., a 2×2 cell for Co), resulting in a density of Co atoms which are close to the experimental value. The right interatomic Co distance of about 2.49 Å came out naturally out of our choice of the unit cells as the distance between two atoms in a (2×2) cell inside a $(\sqrt{3} \times \sqrt{3})$ cell of Au(111)

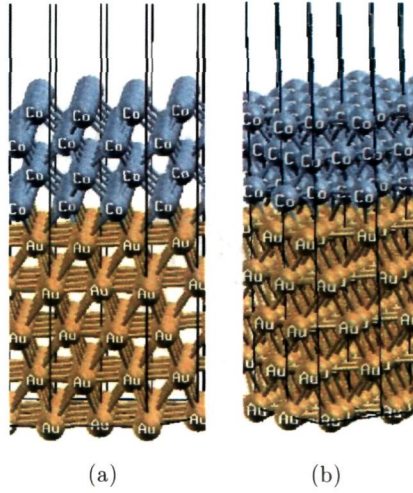
Figure 5.3: Top view of the interface structure of the reconstructed Co/Au(111) system showing Co (blue color spheres) and Au atoms (yellow color spheres). The black lines mark the surface unit cells. Note that the same surface unit cell serves as a $(\sqrt{3} \times \sqrt{3})$ cell for the Au layers and (2×2) cell for the Co layers. Also the Co overlayer is rotated by 30° with respect to the Au layer.



is $2.87 \times \sqrt{3}/2 = 2.485 \text{ \AA}$. The resulting structure, however, gives rise to a hexagonal Co layer rotated 30° with respect to the Au layer (see Fig. 5.3) (they are not rotated in the experimental structure).

Fig. 5.4 shows the optimized structures of the reconstructed and the pseudomorphic Co/Au(111). In the pseudomorphic Co/Au(111), there are four Co layers with three atoms per layer and in the reconstructed Co/Au(111), there are three Co layers with four Co atoms per layer. As is clear from Fig. 5.4, the Co layers in the reconstructed structure are more dense and correspond to an atomic number density which is very close to the experimental structure. Finally, we put methanethiolate on the reconstructed 3 ML Co/Au(111). We considered both the pseudomorphic and the reconstructed Co/Au(111) for the thiol deposition. We considered Co layers in both fcc as well as hcp stackings and found the hcp stacked structure to be energetically favorable over the fcc stacked one. The molecule was initially placed vertically such that the sulfur atom occupies the three-fold hollow site and carbon atom sits

Figure 5.4: Structures (side view) of (a) 4 ML pseudomorphic and (b) 3ML reconstructed $\text{Co}/\text{Au}(111)$ in $(\sqrt{3} \times \sqrt{3})$ cell. Blue and yellow spheres represent cobalt and gold atoms respectively. Vertical black lines mark the unit cells; z -axis is along the vertical direction.

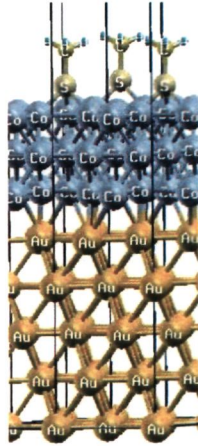


directly above the sulfur atom, and the three hydrogen atoms projecting out symmetrically around carbon atom, 120° apart from each other (Fig. 5.5). Positions of all the Co and the CH_3S atoms were allowed to relax to get the optimized geometry of the systems.

5.4 Our Calculations: Method

All the energetics and structures are calculated using the plane wave pseudopotential density functional theory as implemented in the Quantum ESPRESSO distribution [175]. Since our main goal is to calculate the magnetic anisotropy energies of quasi-two-dimensional systems where Au is taken as the substrate material, the determination of its correct lattice constant becomes crucial as

Figure 5.5: *The side view of the 3 ML reconstructed $\text{CH}_3\text{S}/\text{Co}/\text{Au}(111)$ in the hcp stacking of Co. The atoms are shown as spheres with their atomic symbols written on them. The vertical black lines mark the unit cells; z-axis is in vertical direction. In each unit cell, there are three Co layers with four atoms per layer and five Au layers with three atoms per layer.*



the MAE is very sensitive to the lattice spacing. Therefore, we chose the local density approximation (LDA) as it reproduces very well the correct lattice constant of Au. The interaction of electrons with the nuclear charge was approximated by an ultrasoft pseudopotential (USPP) [39] for all the atoms. The calculated lattice constant of bulk Au of 2.87 \AA , which is in very good agreement with the experimental value of 2.88 \AA , was used as a lattice parameter of the simulation cell.

For the (1×1) cell of the clean $\text{Co}_n/\text{Au}(111)$ substrate, all the Co layers and the top two Au layers were allowed to relax. A $14 \times 14 \times 1$ uniform k -point mesh in the two-dimensional Brillouin zone was used for the (1×1) cell. A kinetic energy and charge density cutoff of 30 Ry and 300 Ry respectively,

and a smearing value of 0.01 Ry was used.

For the methanethiolate adsorbed substrate, we used a ($\sqrt{3} \times \sqrt{3}$) R30° cell. The same parameters as for the clean substrate except for a lower mesh of k -points of $6 \times 6 \times 1$ (as taken by Wang *et al.* [237]) was used in this (adsorbed substrate) case. All the Au layers were kept fixed while all the Co layers and the thiol molecule were relaxed.

The MAE calculations were done using fully relativistic pseudopotentials for all the elements. USPPs were used for all the elements except sulfur, for which a norm-conserving pseudopotential was used. A high kinetic energy cutoff of 40 Ry and a charge density cutoff of 500 Ry was used to ensure high accuracy of MAE calculations. MAE convergence with respect to the k -points was checked carefully. A low smearing parameter of 0.0007 Ry was used. The convergence of total energies was ensured with a high convergence threshold of 10^{-8} Ry.

5.5 Results and Discussion

5.5.1 Pseudomorphic Co Films on (1×1) Au(111)

We first did a comparative study of the energetics and magnetic moments of the $\text{Co}_n/\text{Au}(111)$ system for $n=1, 2, 3, 4, 5$ using a (1×1) surface unit cell. Although this pseudomorphic cell would not allow us to consider reconstruction of the Co films, it might give us some clues about why Co reconstructs by studying, e.g., the interlayer relaxations. Also, for small n (~ 2), this is the correct structure as the Co grows pseudomorphically on Au(111) at

early growth stages. Although in the bulk, Au layers have a fcc stacking (ABCABC...) along the [111] direction, for the (111) surface, it has been observed that there are regions where the top layer atoms alternately occupy fcc and hcp sites, separated by regions of misfit dislocations (the famous herringbone reconstruction [246]). Therefore, we have considered these two stacking possibilities for the top Au layer, i.e., the top Au layer atoms are considered to occupy both the hcp and the fcc sites. Now, Co also can be put on two available low-energy sites (hcp and fcc) on the Au(111) surface. These choices (of the two available low-energy sites) are there for every layer that is subsequently put.

For the 1 ML Co/Au(111) ($n = 1$), as for the Fe/A(111), we have considered four cases of overlayer and sub-overlayer stackings: case (i) (ABCABC stacking), case (ii) (ABCACB stacking), case (iii) (ABCABA stacking) and case(iv) (ABCACA stacking). The first five letters denote the Au(111) layers and the sixth one is for Co. The interlayer relaxations, magnetic moments and relative stabilities of the four configurations considered are tabulated in Table 5.1. We find the ABCABC stacking (case(i)) to be the most stable giving the order of stability is as : case(i) > case(ii) > case(iii) > case(iv). We also checked the order of stability of these stackings by allowing three Au layers (in the earlier case, it was just two Au layers) to relax and we found the same order as above. For the Co overlayers, the fcc site at the Au(111) surface is more favorable than the hcp site even when the top Au layer atoms are placed on the hcp sites (case(i) and case(ii)). The interlayer relaxations and magnetic moments seem to be very little affected by different stackings, nevertheless, there seems to be a trend: the lesser stable stackings show

Table 5.1: Results for pseudomorphic $\text{Co}_1/\text{Au}(111)$: interlayer relaxed distances d (in \AA), average magnetic moment μ (in μ_B/Co atom) and the stability ΔE (meV per (1×1) cell) of the four configurations (for $n = 1$) relative to the most stable one (case(i)), for pseudomorphic $\text{Co}/\text{Au}(111)$.

	Case(i)	Case(ii)	Case(iii)	Case(iv)
$d_{\text{Co}_1-\text{Au}_1}$	1.97	1.97	1.98	1.98
$d_{\text{Au}_1-\text{Au}_2}$	2.33	2.35	2.35	2.36
$d_{\text{Au}_2-\text{Au}_3}$	2.32	2.34	2.32	2.33
μ	1.80	1.81	1.82	1.82
ΔE	0.0	14.12	42.30	53.38

higher moments. This is later found to be true for $n > 1$ cases as well.

For the 2 ML $\text{Co}/\text{Au}(111)$ ($n = 2$), we have considered eight possible stacking sequences for the top three layers (two of Co and one of Au) (see Table 5.2). Here, the most stable stacking is the one in which the top Au layer and the next Co layer atoms occupy the fcc sites (as in the 1 ML system) and the top Co layer atoms sit on the hcp sites with respect to the atomic layers below it (i.e., ...ABCB stacking). This preference of the top Co layer to occupy hcp sites is there even if the top Au layer atoms occupy hcp sites (i.e., ...ACBC stacking) (Note that in the reconstructed $\text{Au}(111)$ surface, there are regions where the Au atoms in the topmost layer occupy hcp sites). From these observations, one can infer that the favorable stacking is the one in which (1) the $\text{Au}(111)$ substrate maintains its perfect fcc stacking, (2) the first Co layer occupies fcc sites on the $\text{Au}(111)$ and (3) the top Co layer occupies the hcp sites with respect to the Co layers below it. Thus, the stacking ...ACAB for the 2 ML Co on $\text{Au}(111)$ is the least stable as this is just opposite to all the three preferences. Surprisingly, the magnetic moments per Co atom are

Table 5.2: Results for pseudomorphic $\text{Co}_2/\text{Au}(111)$: interlayer relaxed distances d (in \AA), average magnetic moment μ (in μ_B/Co atom) and the stability ΔE (meV per (1×1) cell) of the eight configurations (for $n = 2$) relative to the most stable one (in order of stability). The stacking sequence of the top three layers (two of Co and one of Au) is shown.

	BCB	CBC	BAB	BCA	CAC	CBA	BAC	CAB
$d_{\text{Co}_1-\text{Co}_2}$	1.54	1.54	1.53	1.52	1.54	1.52	1.51	1.51
$d_{\text{Co}_2-\text{Au}_1}$	2.07	2.05	2.06	2.07	2.06	2.07	2.09	2.08
$d_{\text{Au}_1-\text{Au}_2}$	2.35	2.35	2.36	2.33	2.37	2.35	2.36	2.37
$d_{\text{Au}_2-\text{Au}_3}$	2.32	2.33	2.32	2.32	2.33	2.33	2.32	2.33
μ	1.87	1.89	1.90	1.88	1.92	1.90	1.91	1.92
ΔE	0.0	13.32	27.00	28.52	38.55	43.71	59.27	72.27

slightly higher compared to the 1 ML systems. Putting more layers of Co on the 1 ML Co/Au(111), the average Co-Au inter-layer distance has increased. For the 3 ML Co/Au(111) ($n = 3$), we have considered nine different stacking configurations of Co and Au layers, including pure hcp, fcc and mixed ones (see Table 5.3). We find that the configurations in which the Co layers are in hcp stackings (the first five cases in Table 5.3) are more stable than the ones in which they are in fcc stackings (the last four cases in Table 5.3). The most stable stacking (i.e., ...BCBC) is the one in which the top Co layer atoms of the 3 ML Co are put at the hcp sites of the most stable 2 ML configuration (i.e., BCB in Table 5.2). An equivalent hcp stacking of three Co layers, keeping the top Au layer and the next Co layer atoms at the fcc sites (i.e., satisfying conditions (1) and (2)), can be achieved by the sequence ...BCAC (although the second (from the Au surface) Co layer atoms have to occupy fcc sites with respect to the top Au layer). The least stable stacking

Table 5.3: Results for pseudomorphic $\text{Co}_3/\text{Au}(111)$: interlayer relaxed distances d (in \AA), average magnetic moment μ (in μ_B/Co atom) and the stability ΔE (meV per (1×1) cell) of the nine configurations considered (for $n = 3$) relative to the most stable one (in order of stability). The stacking sequence of the top four layers (three of Co and one of Au) is shown.

	BCBC	BCAC	CBCB	CBAB	BABA	BCBA	BCAB	CBCA	CBAC
$d_{\text{Co}_1-\text{Co}_2}$	1.59	1.59	1.60	1.59	1.59	1.58	1.57	1.58	1.57
$d_{\text{Co}_2-\text{Co}_3}$	1.64	1.64	1.65	1.64	1.64	1.65	1.66	1.66	1.65
$d_{\text{Co}_3-\text{Au}_1}$	2.06	2.06	2.04	2.05	2.05	2.05	2.04	2.04	2.06
$d_{\text{Au}_1-\text{Au}_2}$	2.34	2.34	2.35	2.35	2.36	2.34	2.35	2.35	2.35
$d_{\text{Au}_2-\text{Au}_3}$	2.32	2.32	2.33	2.33	2.32	2.32	2.32	2.33	2.33
μ	1.80	1.80	1.81	1.80	1.82	1.82	1.82	1.83	1.82
ΔE	0.0	0.001	1.96	12.93	17.46	42.01	48.18	54.36	61.80

(...CBAC) has the topmost Au layer on the hcp site and each of the three Co layers occupying the fcc sites on the layer beneath it. From the stabilities of different stackings, it can be inferred that the determining factors for the stability of the $\text{Co}/\text{Au}(111)$ are the following: Co wants to be stacked in the hcp stacking rather than the fcc, and the topmost Au layer wants to remain in the fcc stacking. Note, however, that in the reconstructed $\text{Au}(111)$ surface, one may expect to find regions where Au atoms in the topmost layer occupy hcp sites. The dominant role in deciding the stability is played by the stacking of Co. Since we did not allow for the reconstruction of the Co layers for the (1×1) cell, we could not verify the in-plane lattice constant of the Co films found in experiments but even with these simple calculations we could verify the preferred hcp stackings of the Co layers.

For $n = 4$ and $n = 5$ also, we see the same trends: the pure hcp stacking of Co gives rise to the most stable system while the pure fcc is the least stable (see Tables 5.4 and 5.5).

In Fig. 5.6 we have plotted the magnetic moments per Co atom for the

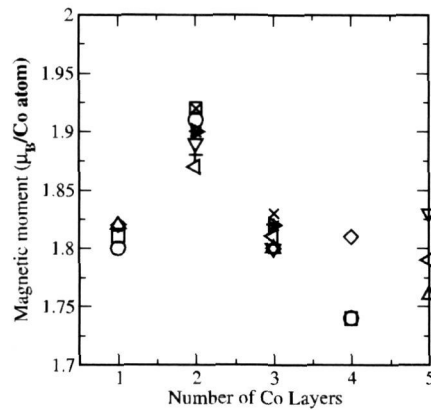
Table 5.4: Results for pseudomorphic $Co_4/Au(111)$: interlayer relaxed distances d (in \AA), average magnetic moment μ (in μ_B/Co atom) and the stability ΔE (meV per (1×1) cell) of the three configurations (for $n = 4$) relative to the most stable one (in order of stability). The stacking sequence of the four Co layers is shown.

	CBCB	CACA	CABC
$d_{Co_1-Co_2}$	1.56	1.56	1.58
$d_{Co_2-Co_3}$	1.71	1.70	1.75
$d_{Co_3-Co_4}$	1.61	1.61	1.63
$d_{Co_4-Au_1}$	2.04	2.06	2.06
$d_{Au_1-Au_2}$	2.34	2.34	2.33
$d_{Au_2-Au_3}$	2.32	2.32	2.32
μ	1.74	1.74	1.81
ΔE	0.0	23.56	115.17

Table 5.5: Results for pseudomorphic $Co_5/Au(111)$: interlayer relaxed distances d (in \AA), average magnetic moment μ (in μ_B/Co atom) and the stability ΔE (meV per (1×1) cell) of the three configurations (for $n = 5$) relative to the most stable one (in order of stability). The stacking sequence of the five Co layers is shown.

	CBCBC	CBABA	CABCA
$d_{Co_1-Co_2}$	1.56	1.57	1.57
$d_{Co_2-Co_3}$	1.69	1.69	1.73
$d_{Co_3-Co_4}$	1.68	1.70	1.70
$d_{Co_4-Co_5}$	1.61	1.63	1.62
$d_{Co_5-Au_1}$	2.04	2.04	2.06
$d_{Au_1-Au_2}$	2.34	2.33	2.34
$d_{Au_2-Au_3}$	2.32	2.32	2.32
μ	1.76	1.79	1.83
ΔE	0.0	57.88	123.87

Figure 5.6: *Magnetic moment per Co atom for different thicknesses of Co layers in Co/Au(111) for considered stackings. The symbols, for a given n , in the decreasing order of stability are : circle, square, up-pointing-triangle, left-pointing-triangle, down-pointing-triangle, right-pointing-triangle, plus, cross and star signs.*



pseudomorphic $\text{Co}_n/\text{Au}(111)$ systems. Moments are enhanced compared to the hcp bulk Co value of $1.71 \mu_B/\text{Co atom}$. Comparing the 1 ML $\text{Co}/\text{Au}(111)$ with the $\text{Co}/\text{Rh}(111)$ in the previous chapter, the moments are smaller for the $\text{Co}/\text{Au}(111)$ (it was $2.67 \mu_B/\text{Co atom}$ for the $\text{Co}/\text{Rh}(111)$) due to the very low magnetic polarizability of the Au substrate. Surprisingly, the 2 ML Co gives highest moment rather than 1 ML. This could be due to the smaller Co-Au distance for the 1 ML case compared to the other cases. The average magnetic moment is roughly the same for the 1 ML, 3 ML, 4 ML and 5 ML $\text{Co}/\text{Au}(111)$ systems. However, which is in general true for all the n considered, the magnetic moments for the more stable stackings are lower compared to the ones for the less stable stackings.

Table 5.6: Comparison of stability ΔE (meV/Co atom), relaxed interlayer distances d (in \AA) and magnetic moments μ (in μ_B /Co atom) for the pseudomorphic (PM) and the reconstructed (Rec) Co/Au(111) for fcc and hcp stackings of Co.

	ΔE	d_{12}	d_{23}	d_{34}	d_{45}	d_{56}	μ
PM(fcc)	424.0	1.6	1.7	1.6	2.1	2.3	1.8
PM(hcp)	395.1	1.6	1.7	1.6	2.0	2.3	1.8
Rec(fcc)	11.8	1.9	1.9	2.3	2.3		1.7
Rec(hcp)	0.0	1.9	1.9	2.3	2.3		1.6

5.5.2 Co Films on $(\sqrt{3} \times \sqrt{3})$ Au(111)

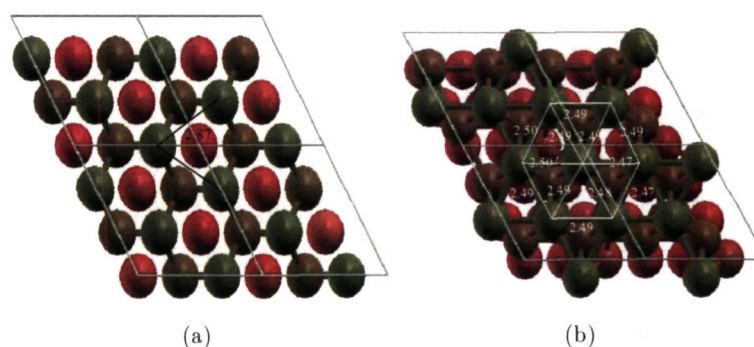
We have considered pseudomorphic as well as reconstructed Co thin-films on Au(111) with Co in both hcp and fcc stackings, in a $(\sqrt{3} \times \sqrt{3})$ cell of Au(111). The $(\sqrt{3} \times \sqrt{3})$ cell enables us to consider reconstructed as well as pseudomorphic Co films. We have considered three layers of Co with four Co atoms per layer (making it a total of twelve Co atoms in the cell) for the reconstructed film. For the pseudomorphic film, we took a slab with four Co layers (with three atoms per layer at the Au in-plane distance) so that we can compare it with the reconstructed case. The interplanar relaxations in the Co layers, relative stability of the pseudomorphic and the reconstructed structures in both the fcc and hcp stackings of Co and the total magnetic moment per Co atom, are given in Table 5.6. Note that there is one less Co layer in the reconstructed Co/Au(111).

By comparing the numbers in the first column of Table 5.6 (which is possible since all the structures considered contain the same number of atoms), we find that the reconstructed film structures are more stable than the pseudomorphic structures. Interplanar distances and magnetic moments are slightly

smaller in the hcp case compared to the corresponding fcc case. Comparing the interlayer relaxations, magnetic moments and the relative stability for the pseudomorphic structures with those of the corresponding (1×1) cell for $n = 4$ (Table 5.4), we see that they are almost identical. Our *ab initio* results for the structural properties are in excellent agreement with the experimental findings. Experimental investigations [218, 221, 223] show that Co layer stacking on Au(111) is usually hcp; the average in-plane distance of 2.49 Å (see Fig 5.7) fixed by the choice of our unit cell structure is very close to the experimental value of 2.51 Å [221]. In Ref [223], the authors have found an interplanar Co distance of about 2.07 Å on the Au(233) vicinal surface. For the bilayer Co islands on Au(111), the STM measurements give a value of 2.05 Å for the interlayer distance [218]. Our interlayer distances for the reconstructed Co/Au(111) (Table 5.6) give rise to a mean value of 2.03 Å which is in good agreement with the experimental values. However, the huge interplanar relaxations in the case of pseudomorphic films lead to an average interplanar distance of about 1.63 Å, in contrast to 2.03 Å for the reconstructed case (see the pseudomorphic and reconstructed hcp cases in Table 5.6), indicate that the pseudomorphic structures are not stable and would want to densify.

The total magnetic moments/Co atom of the $(\sqrt{3} \times \sqrt{3})$ Co/Au(111) structures for the four systems are also given in Table 5.6. A slightly higher moment in the case of fcc stacking compared to the hcp one is due to a slightly higher interlayer distances in the fcc case. In the case of reconstructed substrates, however, the reduced in-plane distances have brought the magnetic moment down, although the interlayer distances are larger compared

Figure 5.7: Top view of the (a) pseudomorphic and the (b) reconstructed Co/Au(111) (hcp) system in $(\sqrt{3} \times \sqrt{3})$ cell showing the in-plane Co distances. The green spheres are the top Co layer atoms, while the brown spheres represent the Co atoms below the top Co layer. The red spheres are the Au atoms. The numbers are the in-plane interatomic distances (in Å) marked by the white lines in (b) and black lines in (a); and rhombi mark the surface unit cells used in our calculations.



to the pseudomorphic cases. However, this trend in magnetic moment for the $(\sqrt{3} \times \sqrt{3})$ cell is similar to the (1×1) cell where more stable stackings showed lower moments.

5.5.3 Methanethiolate on Reconstructed Co/Au(111)

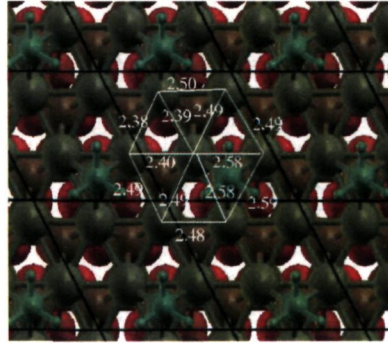
Substrate

Next, we considered CH_3S molecules on the reconstructed Co/Au(111) substrate. We considered the adsorption of methanethiolate (CH_3S) instead of methanethiol (CH_3SH) because in a previous study [237] it was found that methanethiol does not adsorb molecularly (i.e., as a whole molecule) on the Co(0001) surface. Experiments also show that CH_3SH deprotonates when

adsorbed on the substrates at low temperatures [224–226, 235]. In a previous study [236], the authors found the $(\sqrt{3} \times \sqrt{3})$ and the (2×2) structures to be energetically close and were favored over other structures considered (1×1 , 2×1 , and 2×3). We considered both fcc and hcp stacked Co and found that the $\text{CH}_3\text{S}/\text{Co}/\text{Au}(111)$ system with hcp stacking of Co (and the CH_3S molecule sitting at the hcp site on the Co surface) is more stable compared to the fcc stacking (with the CH_3S molecule sitting at the fcc site) by 0.17 eV. In Table 5.7 we have tabulated the relaxed distances and the adsorption energies of the reconstructed $\text{CH}_3\text{S}/\text{Co}/\text{Au}(111)$ for both fcc and hcp stackings of Co layers. The bond-lengths of the carbon-sulfur bond, $\text{C-S}(d)$, the vertical distance from the sulfur atom to the top Co layer, $\text{S-Co}(d_z)$, the average sulfur-cobalt bond-length, $\text{S-Co}(d)$, the Co interlayer distances, the total magnetic moments/Co atom and the adsorption energies, E_{ads} , are given in Table 5.7 for the fcc and the hcp reconstructed $\text{CH}_3\text{S}/\text{Co}/\text{Au}(111)$. In Fig. 5.8 we have shown the relaxed in-plane geometry of the hcp reconstructed $\text{CH}_3\text{S}/\text{Co}/\text{Au}(111)$ system.

We see (in Table 5.7) that the distances are slightly shorter for the hcp stacked Co compared to the fcc one. Comparing with the $\text{CH}_3\text{S}/\text{Co}(0001)$ system studied by Wang *et al.* [237], the values of the distances of our $\text{CH}_3\text{S}/\text{Co}/\text{Au}(111)$ system are in very good agreement with theirs, albeit ours are consistently a little shorter. This could be attributed to the use of GGA functional in their study. The vertical S-Co distance of 1.46 \AA is relatively shorter in our case compared to their value of 1.68 \AA . Our adsorption energy of 4.80 eV is also higher compared to their value of 2.92 eV. This somewhat higher adsorption energy is due to relatively shorter $\text{S-Co}(d_z)$ distance

Figure 5.8: Top view of the the reconstructed hcp $\text{CH}_3\text{S}/\text{Co}/\text{Au}(111)$ system in $(\sqrt{3} \times \sqrt{3})$ cell showing the in-plane Co distances. The green spheres are the top Co layer atoms, the brown spheres represent the Co atoms below the top Co layer while the red spheres are the Au atoms. The numbers are the in-plane interatomic distances (in \AA) marked by the white lines; the rhombi (black lines) mark the surface unit cells used in our calculations.



(i.e., more stable binding) in our case. It is also possible that the presence of the Au layers (which are absent in their study) can lead to differences, though it is perhaps unlikely that they will lead to such strong effects.

Very interestingly, when we considered CH_3S on a hcp 5 ML pseudomorphic $\text{Co}/\text{Au}(111)$ (in $\sqrt{3} \times \sqrt{3}$ cell), we found a huge structural rearrangement of the Co layers which lead to the geometry very close to the one as in the

Table 5.7: Comparison of C-S bond-length, S-Co bond-length (three S-Co bonds) (d), S-Co vertical distance (d_z), subsequent interlayer relaxations of Co layers (all in \AA) and the adsorption energy E_{ads} (in eV) for the fcc and the hcp stackings of the reconstructed $\text{CH}_3\text{S}/\text{Co}/\text{Au}(111)$. The total magnetic moment μ (in μ_B/Co atom) is also given.

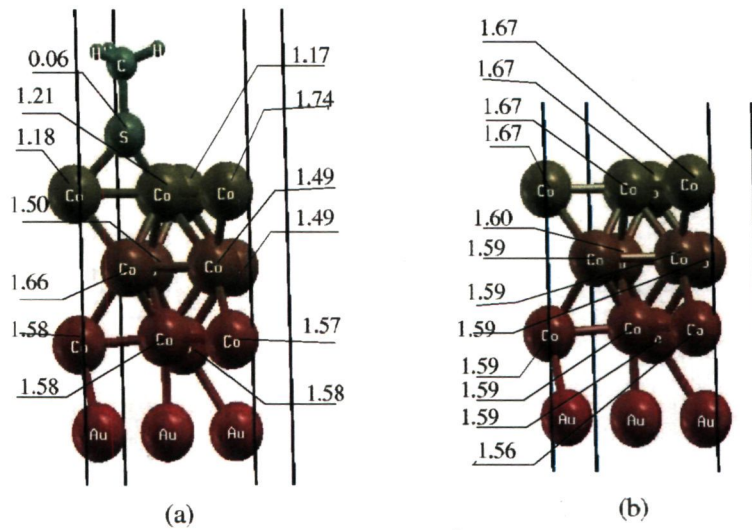
	C-S(d)	S-Co(d_z)	S-Co(d)			d_{12}	d_{23}	d_{34}	μ	E_{ads}
Rec(hcp)	1.81	1.46	2.09	2.09	2.09	1.90	1.89	2.29	1.48	4.80
Rec(fcc)	1.81	1.48	2.11	2.11	2.11	1.93	1.90	2.29	1.59	4.77

reconstructed Co/Au(111). There remained only four Co layers (out of initial five) with an increased density of Co atoms in the bottom three layers (from the initial three atoms per layer to four atoms per layer now) while the top Co layer contained a “hole” in the Co layer. Co atoms in the bottom three layers with increased atomic density seemed to get stacked in the fcc stacking with the average in-plane atomic distance very close to the bulk Co value. However, this reconstruction of Co layers happened only in the presence of CH₃S, for the clean pseudomorphic Co films on Au(111), no such structural rearrangement of Co atoms took place.

5.5.4 Magnetic Moments and Density of States

In Fig. 5.9 we have shown the magnetic moments on the individual Co atoms of the reconstructed hcp CH₃S/Co/Au(111) and the clean Co/Au(111) substrate. First, we see that the surface Co atom of the clean Co/Au(111) has a very slightly larger magnetic moment ($1.67 \mu_B$) compared to the bulk value of $1.63 \mu_B$. There are two types of surface Co atoms for the CH₃S/Co/Au(111): those directly bonded to the sulfur, having lower magnetic moments of $\sim 1.20 \mu_B$, and those unbonded to sulfur having a larger magnetic moment of $1.74 \mu_B$. These trends in the magnetic moments are also in good agreement (given the discrepancy between LDA and GGA) with those of Wang *et al.* [237]. The authors [237] found these values of magnetic moments as $\sim 1.66 \mu_B$ and $\sim 1.85 \mu_B$ respectively for the Co atoms bonded directly to S and the one not bonded. However, the magnetic moments of the surface Co atoms which are directly bonded to the S atom have reduced much more in our case (from

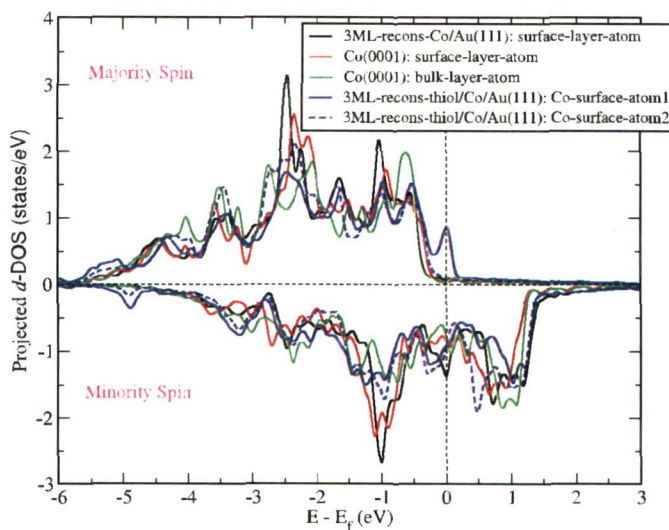
Figure 5.9: Projected magnetic moments (in μ_B) on the individual atoms of the reconstructed (a) $\text{CH}_3\text{S}/\text{Co}/\text{Au}(111)$ and (b) $\text{Co}/\text{Au}(111)$ systems are shown (labelled against the atoms). The moments on the Au, C and H atoms are negligible and not shown here. Only part of the side view of the full unit cell is shown.



$1.67 \mu_B$ for the clean substrate to $\sim 1.20 \mu_B$ for the methanethiolate adsorbed substrate) compared to Wang *et al.*'s (from $1.76 \mu_B$ for the clean substrate to $\sim 1.66 \mu_B$ for the methanethiolate adsorbed substrate). This again could be attributed to the use of LDA and the shorter S-Co distance in our case. Although the exchange splitting of the Co $3d$ bands has induced a small magnetic moment of about $0.06 \mu_B$ on the sulfur atom, the interface magnetism has reduced considerably due to the thiol adsorption (unlike the finding of a previous study [237] where the authors did not find any net reduction in the surface magnetic moment). The moments on the other Co layers also have decreased after putting the methanethiolate on $\text{Co}/\text{Au}(111)$.

Fig. 5.10 shows the projected d -density of states of the top layer Co atoms of

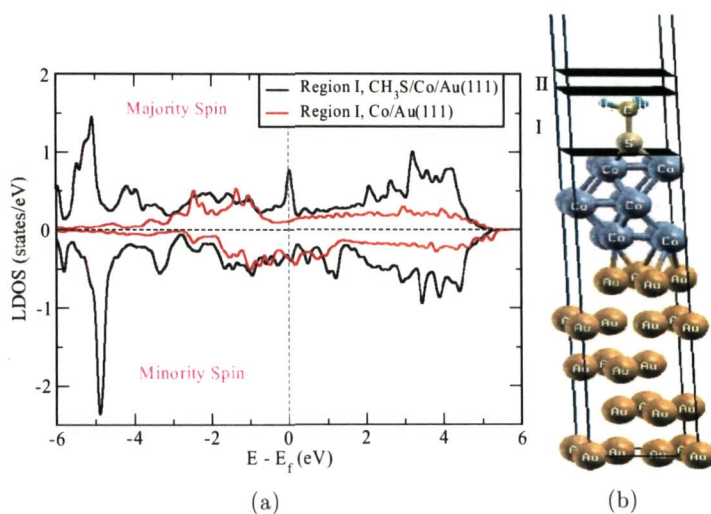
Figure 5.10: Spin polarized, projected d -density of states of the top Co layer/Co atom for the 3 ML reconstructed Co/Au(111), the Co(0001) and the methanethiolate/Co/Au(111) systems. For the methanethiolate/Co/Au(111) system, three out of four surface layer atoms in the unit cell are equivalent (those bonded directly to thiol) and one is different.



the 3 ML reconstructed Co/Au(111) and the methanethiolate/Co/Au(111) systems along with that of the surface and bulk-like layer of the hcp Co(0001) slab for comparison. In the methanethiolate/Co/Au(111) system studied by us, out of four surface Co atoms, three of them show the same DOS and magnetic moments (those bonded directly to the sulfur of methanethiolate and labeled as Co-surface-atom1 in the figure) and the other one shows somewhat different behavior (labeled as Co-surface-atom2 in the figure). This one Co atom has a higher magnetic moment ($\sim 1.7 \mu_B$) compared to the other three Co atoms ($\sim 1.2 \mu_B$) (see Fig. 5.9).

Fig. 5.11 shows the local density of states (LDOS) resolved in space (along the z -direction) between the Co surface and the CH_3S molecule spanning a

Figure 5.11: (a) Local density of states (LDOS) integrated over the volume of region I (shown in (b)) of the reconstructed hcp $\text{CH}_3\text{S}/\text{Co}/\text{Au}(111)$ and $\text{Co}/\text{Au}(111)$. The dashed vertical line shows the position of the Fermi level. (b) side view of (part of) the unit cell of the reconstructed hcp $\text{CH}_3\text{S}/\text{Co}/\text{Au}(111)$ showing the planes (in black color) forming the boundary of regions I and II along the z direction.



region of around 3.5 \AA above the Co surface (region I in Fig. 5.11). The DOS gets modified due to the presence of the CH_3S molecule and a prominent peak appears at the Fermi level in the majority spin channel.

5.5.5 Charge Transfer

We have done charge transfer analysis of the CH_3S adsorbed $\text{Co}/\text{Au}(111)$ system. Fig. 5.12 shows the planar integral of the charge difference along the z -axis. This was obtained by subtracting the charge densities of the $\text{Co}/\text{Au}(111)$ and the CH_3S from the $\text{CH}_3\text{S}/\text{Co}/\text{Au}(111)$ system and then

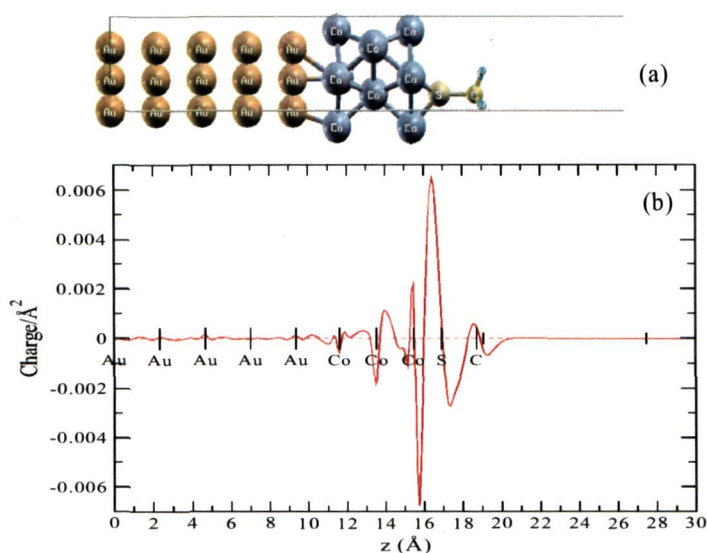
taking a planar integral (in the xy plane) of this charge density difference along the z axis. One can see that there is a dip in the charge density at the Co surface and an increase in the charge density at the sulfur site, showing the transfer of charge from Co surface to the CH_3S molecule. However, the value of this charge is small, about 0.04 e. Comparing this value of the charge transfer with the values obtained for the $\text{CH}_3\text{S}/\text{Co}(0001)$ (0.22 e) and $\text{CH}_3\text{S}/\text{Au}(111)$ (0.09 e) [236], we see that it is even smaller than the charge transfer of 0.09 e for the $\text{CH}_3\text{S}/\text{Au}(111)$. This shows that the charge transfer from the Co to methanethiolate is reduced by supporting the $\text{Co}(0001)$ with a $\text{Au}(111)$ substrate. However, it should be noted that the authors [236] used the GGA functional whereas we used the LDA.

5.5.6 Magnetic Anisotropy Energy

For the calculation of MAE, we used more stringent numerical parameters to ensure accuracy. We used a high kinetic energy cutoff of 40 Ry and a charge density cutoff of 500 Ry. We chose a small smearing value of 0.0007 Ry. We checked the convergence of MAE with respect to k -points. The convergence threshold for the total energy was set to 10^{-8} Ry.

We find that the pseudomorphic Co monolayer on $\text{Au}(111)$ shows a strong tendency towards in-plane orientation of magnetization. We did total energy calculations for the Co monolayer stacked on $\text{Au}(111)$ at fcc sites (case(i)) with the initial three orientations of magnetization—one out-of-plane and two in-plane (along x and y axes) but found that the initial out-of-plane direction started drifting towards the in-plane and finally got aligned along the y -axis,

Figure 5.12: *The planar average of the charge difference along the z axis (in units of electronic charge per \AA^2) for the 3 ML reconstructed hcp $\text{CH}_3\text{S}/\text{Co}/\text{Au}(111)$. (a) Side view of the unit cell of $\text{CH}_3\text{S}/\text{Co}/\text{Au}(111)$ system along the z-direction, (b) the variation of the planar average of the charge transfer as a function of distance (in \AA) along the z-axis. A decrease in charge density near the Co surface and an increase near the sulfur is clearly visible.*



showing a strong instability of magnetization along the perpendicular direction. This is consistent with a previous calculation [211]. We also checked the preference of the easy axis for the free standing Co monolayer at the lattice constant of Au and found that this too showed an in-plane easy axis. Interestingly, the perpendicular direction in this (free standing) case seemed to be a local minimum as, unlike the Au(111) supported Co monolayer case, the magnetization did not drift away from the initial (perpendicular) direction. We did not, however, carry out a detailed study of the MAE for this hypothetical system.

We have also done MAE calculations on the clean and CH_3S adsorbed Co/Au(111)

substrates having hcp stacking of Co. Table 5.8 shows the difference of the total energies between the two directions of magnetization for the 3 ML reconstructed clean and the methanethiolate adsorbed Co/Au(111) at various k -point mesh values. These values show that the energies corresponding to the magnetization direction perpendicular to the plane are lower for both the clean substrate and the methanethiolate adsorbed substrate, making the easy axis lie out-of-plane. This is in contrast to the pseudomorphic Co/Au(111) as well as the free-standing Co monolayer where an in-plane easy axis was found. As mentioned earlier, in the literature, all the theoretical studies of MAE of the Co/Au(111) system have been performed on the simple pseudomorphic systems which are far from the actual experimental structure. Szunyogh *et al.* [211], for example, found an in-plane easy axis for the pseudomorphic Co monolayer on Au(111) which was in disagreement with the experimental finding (extrapolated to monolayer) reported in their paper. Our prediction of the out-of-plane easy axis for the 3 ML reconstructed Co/Au(111) is in agreement with the experimental findings.

Although, the adsorption of methanethiolate has decreased the MAE of the Co/Au(111), the easy axis remains perpendicular to the plane. Thus, the adsorption of methanethiolate results in the reduction of both, the magnetic moment and the MAE. Our preliminary results for the 5 ML clean as well as adsorbed Co/Au(111) show that the MAE did not change after methanethiolate deposition on this 5 ML Co/Au(111) (it was 0.07 meV per Co atom for both the clean and methanethiolate adsorbed Co/Au(111)) and the easy axis remains out-of-plane. This is in contrast to some experimental findings, where the easy axis switched to in-plane beyond 4 ML Co thickness. However, it

Table 5.8: Convergence of the magnetic anisotropy energy (MAE), $E_{tot}(90, 0) - E_{tot}(0, 0)$ (in meV per Co atom), with respect to the k -point mesh for the clean and the CH_3S adsorbed $\text{Co}/\text{Au}(111)$ for the 3 ML thick Co films. The $(90, 0)$ direction (i.e., the x -axis) is in the direction of the horizontal nearest-neighbor (in xy plane) (see Fig. 5.3) and the $(0, 0)$ direction is along the z -axis (perpendicular to the plane). A positive value of MAE shows that the easy-axis is out-of-plane.

k -point mesh	$E_{tot}(90, 0) - E_{tot}(0, 0)$	
	Co/Au(111)	$\text{CH}_3\text{S}/\text{Co}/\text{Au}(111)$
$10 \times 10 \times 1$	0.23	0.10
$20 \times 20 \times 1$	0.18	0.12
$30 \times 30 \times 1$	0.16	0.12
$40 \times 40 \times 1$	0.17	0.12

should be remarked that the dipolar interaction may be responsible for this switch of the easy axis for thicker films.

From the above results it seems that the electronic contribution alone favors an out-of-plane orientation of magnetization for Co films thicker than 1 ML. However, for 1 ML free-standing as well as supported (both reconstructed and pseudomorphic) Co on Au(111), the electronic contribution to the MAE gives rise to an in-plane easy axis.

5.6 Summary

In this chapter we studied structural and magnetic properties of methanethiolate adsorbed on cobalt on gold: $\text{CH}_3\text{S}/\text{Co}/\text{Au}(111)$. $\text{Co}/\text{Au}(111)$ is an interesting substrate as it exhibits many interesting magnetic properties such as giant magnetoresistance and switching of magnetic easy-axis from in-plane

to out-of-plane as one decreases the Co thickness below 4 monolayers. However, before studying $\text{CH}_3\text{S}/\text{Co}/\text{Au}(111)$, we examined the structural relaxations and magnetic moments of the pseudomorphic Co films on $\text{Au}(111)$ with varying thickness, n , of Co ($n = 1$ to 5). Although the pseudomorphic structure in a (1×1) cell does not allow us to consider the experimentally observed reconstruction of thick Co films (more than two monolayers thick) on $\text{Au}(111)$, it does enable us to study the evolution of morphological parameters such as interplanar relaxations, as a function of Co thickness. However, for low Co thickness (up to two monolayers), Co growth is actually known to be pseudomorphic. We considered all the possible stackings of Co layers for $n=1$ and 2, including the possibility for the top Au layer atoms to occupy the low-energy hcp sites. For $n > 2$, however, we considered only some regular ordered stackings including fcc and hcp. We infer from our findings for all the n considered, that in general, the most favorable stacking for the pseudomorphic $\text{Co}_n/\text{Au}(111)$ is the one in which the Co layers are stacked in the hcp stacking while the top Au layer atoms occupy the fcc sites. Since we restricted the in-plane relaxations (due to pseudomorphic cell), there are huge out-of-plane relaxations of Co layers indicating that the Co layers are under tensile stress and would want to get compressed in the corresponding real systems.

To simulate the real experimental structure of $\text{Co}/\text{Au}(111)$ in which the Co films (beyond two ML thick) on $\text{Au}(111)$ are reconstructed to form a close-packed stacking resembling the structure (in $[0001]$ direction) in bulk Co, we took a $(\sqrt{3} \times \sqrt{3})$ cell of $\text{Au}(111)$ which simultaneously is a (2×2) cell

for the Co, giving rise to the correct number density of Co atoms. However, this hexagonal (2×2) cell for the Co is rotated 30° with respect to the ($\sqrt{3} \times \sqrt{3}$) cell for Au(111) (in experiments, the Co and Au lattices are not rotated with respect to one another). Nevertheless, our choice of this small unit cell enabled us to mimic one aspect of the experimental structure (i.e., the number density) rather correctly, given that the simulation of the real structure requires a huge unit cell which would be prohibitively expensive for the *ab initio* calculations.

The adsorption geometry and relaxed structure of CH_3S on this reconstructed Co/Au(111) was studied. We found that the favored stacking of Co is hcp for both the reconstructed clean Co/Au(111) and CH_3S adsorbed Co/Au(111). However, we found that the magnetic moments corresponding to the fcc stacked Co systems are somewhat larger compared to the hcp cases as well as the various distances (i.e., the Co interlayer distances, the S-Co bond lengths etc.) are also slightly larger in the fcc case. The CH_3S molecule stays vertical on the Co surface (i.e., the C-S bond is perpendicular to the surface). The magnetic moments of the surface and subsurface layers of Co got reduced after methanethiolate adsorption. We also find a small charge transfer from the Co surface to the sulfur which is responsible for the strong chemisorption of the thiols on the Co surface.

We also calculated the magnetic anisotropy energy of the 3 ML and 5 ML reconstructed Co/Au(111) as well as methanethiolate adsorbed Co/Au(111), and determined the easy and hard axes for the two systems. For the 3 ML Co film, we found that the easy axis lies perpendicular to the surface for both the clean Co/Au(111) and the $\text{CH}_3\text{S}/\text{Co}/\text{Au}(111)$. The magnitude of

the MAE, however, is less for the $\text{CH}_3\text{S}/\text{Co}/\text{Au}(111)$ compared to the clean $\text{Co}/\text{Au}(111)$. Experimentally, the Co film of thickness 3 ML on $\text{Au}(111)$ is below the critical thickness of spin-reorientation transition and the easy axis remains out-of-plane. For 5 ML Co film also, we found the out-of-plane easy axis even though in experiments, the easy axis switches to in-plane at this thickness. This switching occurs due to the dipolar interaction which becomes dominant with increasing thickness and it always favors an in-plane orientation of magnetization. As we did not include the dipolar contributions to the MAE but only the contribution from the spin-orbit coupling, our results for the direction of the easy axis at high thickness (5 ML) do not match with the experiment. But our results points to the fact that the spin-orbit contribution to the MAE gives rise to a perpendicular anisotropy even for films as thick as 5 ML. In Chapter 7, we discuss open questions that remain, and discuss future prospects.

Chapter 6

Magnetic Anisotropy of Fe in Low Dimensions: 1D Chain, 2D Square and Triangular Lattices, Fe/Au(111)

6.1 Introduction

The ever growing demand of electronic data storage has generated immense interest in research on non-conventional devices that offer high storage density. With ever increasing size constraints for devices, unconventional materials are now been explored. Magnetic data storage is among the oldest and the most widely used form of electronic data storage. It offers high storage capacity, compactness, high reliability and cost effectiveness at the same time. It finds applications in areas ranging from computer hard disks

to magnetic stripe cards (credit/debit cards).

At present there are mainly three types of digital data storage media: magnetic, optical and solid state. The high cost of manufacturing solid state memory devices limits their use to small scales and mainly to temporary storage (e.g., random access memories). For permanent data storage, magnetic and optical storage media are the main device forms in use. Although optical storage devices have a higher storage density, they are not as fast as magnetic ones. Also, the cost effectiveness of magnetic storage devices makes them more desirable. Therefore, considerable attempts have been directed towards increasing the storage density of magnetic data storage devices as the demand of higher and higher storage density continues to drive the data storage industry.

Magnetic thin films are promising candidates in this regard. Thin film magnetism is an active area of research. Indeed, thin film magnetism has brought important contributions to our fundamental understanding of the physics of magnetism [250] in tandem with critical applications in information technology and computer read-head technology [251].

Magnetic anisotropies are of great technological importance since they define the easy and hard magnetization axes. One of the major tasks in applied research is to find a way to manipulate them. In particular, the reorientation of magnetization may be relevant to developments such as the tilted media approach for data storage applications [252].

The reduction of film thickness gives rise to increased surface and interface effects, which strongly influence the magnetic anisotropy, while the loss of translational invariance perpendicular to the surface and the reduction of

in-plane symmetry may introduce new magnetic anisotropy terms. Many investigations have been directed towards finding the correlation between morphology and magnetism of nanostructures and hoping to be able to induce “controlled” anisotropies in thin films.

In this chapter, we have calculated magnetic anisotropy energies of low dimensional Fe based systems such as free-standing Fe-wires, two-dimensional square and triangular lattices, and a pseudomorphic monolayer of Fe deposited on a clean Au(111) substrate. In this way one can hope to perhaps systematically study the effect of dimensionality and coordination as well as the effect of substrates on the magnetic anisotropy. We have also studied the effect of interatomic spacing on the magnetic anisotropy energy for the Fe-chain, square and triangular lattices.

6.2 Previous work

The MAE of low-dimensional systems has been found to get enhanced hugely compared that to of bulk systems. The easy axis in Fe bulk is along the [001] direction and the MAE is about $4 \mu\text{eV}$ [253]. However, the magnitude of the MAE and the direction of the easy axis of the three bulk ferromagnetic elements (Fe, Co and Ni) has still not been completely settled theoretically. Nowadays, research has moved in to the area of low dimensional systems, instead of the bulk, largely due to the novelty and richness that the field offers but also because the investigations in the bulk MAE has been disappointing. Below we present a short literature review of the MAEs of Fe related systems.

6.2.1 One-dimensional Fe chain

Although, spin-lattice models predict a long-range ferromagnetic or antiferromagnetic order to be non-existent in a perfectly one-dimensional (1D) infinite chain of localized moments at any finite temperature [254, 255], long as well as short range ferromagnetic order has been observed in quasi 1D systems such as monoatomic wires on weakly interacting or nonmagnetic substrates or symmetry broken 1D systems [149, 256–258]. Zero temperature DFT calculations, however, predict an enhanced ferromagnetism for bulk magnetic elements in 1D. The MAE of a 1D monoatomic Fe wire was calculated to be around 2.0 meV/atom [259] which is three orders of magnitude larger than the MAE of bulk Fe. The direction of the easy axis was found to change with the application of stress along the wire [259–261]. The easy axis was calculated to be along the wire at its equilibrium distance (2.27 Å) but a transition of easy axis from along the wire direction to perpendicular to the wire direction was found when the interatomic separation was reduced (to 2.00 Å with the tight-binding method, and 2.08 Å with the *ab initio* DFT method) [259]. In a more advanced tight-binding study using a larger basis set which includes, in addition to *d*, *s* and *p* orbitals also, and by treating intra-atomic electronic interaction in the full Hartree-Fock scheme, the authors [262] found much enhanced values of MAE (and orbital moments) for the free-standing Fe chain. They found that the MAE increases with increasing interatomic separation (from 1.9 to 2.4 Å). Tung *et al.* [261] employing DFT calculations with the GGA, calculated the MAE of an Fe chain up to

an interatomic distance of 2.8 Å. They found that the MAE kept increasing (as high as about 6.0 meV/atom) with the interatomic separation up to about 2.7 Å and thereafter it got decreased. They did not probe its behavior beyond 2.8 Å. Mazzarello *et al.* [263] also did a DFT GGA calculation on the free-standing Fe monoatomic chain as well as a Fe double chain on the Ir(100) surface and found a MAE of 1.9 meV for the free-standing monoatomic chain at an interatomic distance of 2.758 Å.

The MAEs of free-standing Fe monoatomic chains calculated by Mokrousov *et al.* [264] using FP-LAPW method at its equilibrium interatomic distances of 2.19 (with LDA) and 2.26 Å (with GGA) were 1.4 and 5.5 meV per Fe atom respectively. At the interatomic distance of 2.34 Å (corresponding to the Au wire), the MAE values were 5.1 and 7.6 meV per Fe atom for LDA and GGA respectively, while the easy axis was along the wire-axis in all the cases. This shows that the MAE of the free-standing Fe chain increases with increasing the interatomic distance, for both LDA and GGA, in this range of interatomic separations.

Experimentally, Fe wires on different substrates have been studied, showing that the magnetic properties are dependent on the substrate used: Fe wires on Au(111) [265], Cu(111) [257, 266] and Pt(997) [267] have been observed to exhibit out-of-plane anisotropy whereas on W(110), Fe stripes indicate an in-plane magnetic anisotropy [149, 258].

6.2.2 Two-dimensional Fe Systems

For isotropic two-dimensional (2D) systems also, the Heisenberg model predicts the absence of any long range magnetic order at finite temperatures [255]. Nevertheless, long range magnetic ordering has been observed for some quasi-2D systems due to the presence of structural anisotropies. DFT calculations again show an enhanced magnetism for some $3d$ and $4d$ metallic systems in reduced dimensions.

The MAE of a square lattice of Fe at the Ag and Au lattice constants (2.89 and 2.88 Å respectively) calculated by Li *et al.* [268] using the LAPW method, was about 0.04 meV/atom and 0.03 meV/atom respectively and an in-plane easy axis was obtained. In contrast, at the Ag lattice constant, Gay *et al.* [253] performing the self-consistent local orbital (SCLO) calculations obtained a MAE of 0.38 meV/atom, and the easy axis perpendicular to the plane, and Nakamura *et al.* [269] performing FLAPW (LDA) calculations obtained a MAE of 0.28 meV/atom (noncollinear treatment) and 0.24 meV/atom (collinear treatment) and an out-of-plane easy axis. The same authors [269] also calculated MAE at the lattice constant of Cu(001) (2.56 Å) and found an out-of-plane easy axis and larger values of MAE: 0.36 meV/atom (noncollinear treatment) and 0.30 meV/atom (collinear treatment), indicating an increase in MAE with the decrease in interatomic distance. At the equilibrium nearest-neighbor distance of bulk Fe (2.50 Å), the MAEs calculated using *ab initio* DFT with LDA functional for the free-standing Fe (100) and (110) monolayers were 0.23 and 0.22 meV per unit cell, respectively, with an out-of-plane easy axis [259].

The behavior of the Fe monolayer on some weakly interacting metal surfaces is also similar. Guo *et al.* [271] studied a square Fe monolayer embedded in noble metals (Cu, Ag, Au) (100) surfaces using LMTO (LDA) method and found an out-of-plane easy axis with MAE values of 0.428, 0.796 and 0.743 meV/Fe atom for Cu/Fe/Cu, Ag/Fe/Ag and Au/Fe/Au systems respectively, showing, in contrast to the free-standing case of Nakamura *et al.* [269], that MAE increases with lattice spacing. However, Li *et al.* [268] found quite different values of MAE for similar systems of Fe/Ag(100) and Fe/Au(100): 0.06 meV/atom for Fe/Ag(100) and 0.56 meV/atom for Fe/Au(100) with an out-of-plane easy axis for both the systems. Fe layers on Au(001) studied by Szunyogh *et al.* [270] using the screened Korringa-Kohn-Rostoker (KKR) method led to an out-of-plane easy axis when considering only the band energies. The band energy contribution to the MAE was around 0.6 meV for the one-monolayer-thick Fe on Au(001).

It seems from the above studies that except for the earlier calculation by Li *et al.* [268], there has been agreement about the direction of the easy axis of the Fe square lattice (free-standing as well as on (001) surface of noble metals) to be out-of-plane. The magnitude of the MAE, however, differs, depending upon the method and approximations used.

The easy axis in ultrathin Fe films on W(110) has been found to be in-plane (parallel to $[1\bar{1}0]$ direction). For a similar system of $\text{Co}_n/\text{Cu}(111)$, an in-plane MAE is found for one monolayer ($n = 1$) thickness [272]. However, Co/Au(111) multilayers have been found to exhibit perpendicular magnetization with a large magnetocrystalline anisotropy [207].

6.2.3 Fe/Au system

The growth behavior and structural properties of Fe/Au systems have been studied extensively both experimentally and theoretically. Over the last two decades, considerable amount of magnetic studies measuring, e.g., the magnetic ordering as well as magnetic anisotropy, have also been carried out. In spite of a considerable difference in the surface energies of Fe (2.94 Jm^{-2}) and Au (1.63 Jm^{-2}), the Fe monolayer has been reported to grow pseudomorphically on Au(111) [265,273,274]. In our study, therefore, we have considered a pseudomorphic Fe layer on Au(111). The Au(111) surface shows the famous herringbone reconstruction [246] that has been exploited as a template for the growth of a number of metals.

In general, it has been observed that below a critical thickness, Fe grows pseudomorphically and with fcc stacking on Au(111), and the easy axis is perpendicular to the plane [274,278–280]. With increasing thickness of Fe (above ~ 3 ML), there is a structural transition from fcc(111) to bcc(110), accompanied by a transition of the easy axis from out-of-plane to in-plane [273,274,281,282]. Studies show that this out-of-plane easy axis is actually not strictly perpendicular but its direction is distributed in a cone with its axis perpendicular to the plane [279]. However, Ohresser *et al.* [265] observed an in-plane magnetization below a very low coverage of 0.3 ML which corresponds to zero-dimensional islands formed at the point defects of the herringbone reconstruction. Ohresser *et al.* also observed, in contrast to previous studies, an in-plane easy-axis for 1ML coverage of Fe on Au(111). So, there seems to be a disagreement in the literature about the easy axis

of the monolayer of Fe on Au(111). The calculation of MAE of Fe monolayer at Au(111) has not been done to our knowledge. However, Fe/Au(111) multilayers with one Fe and two Au layers using LMTO, LDA have been studied [283], and an MAE of 1.025 meV/unit cell with the easy axis perpendicular to the plane has been found.

6.3 Method

All calculations are performed using the *ab initio* density functional theory [23] as implemented in the Quantum ESPRESSO package [67, 175]. The Fe/Au(111) system was modeled by a (1x1) surface unit cell consisting of six layers of the substrate and a monolayer of Fe on top of it. The (111) surface of Au has two types of sites available: hcp and fcc. We tried putting Fe atoms on both of these sites. It has been found for the Au(111) substrate that it reconstructs [246] and there are regions where the top surface Au atoms selectively occupy fcc or hcp sites. Keeping this in view, we have considered the top substrate atomic layer put first on hcp sites (giving the stacking sequence for the six substrate layers from the bottom as ABCABA). The two available sites on this substrate viz. B and C were checked for the energetics preference for the Fe monolayer and the C site was found to be favored over the B site. Therefore, we have in total considered four cases for the Fe/Au(111) system according to different stackings: case (i) (ABCABCA stacking), case (ii) (ABCABAC stacking), case (iii) (ABCABCB stacking) and case(iv) (ABCABAB stacking). All geometry optimizations were done with scalar relativistic calculations. Atoms were placed at the calculated

equilibrium bulk NN distance of Au (2.86 Å) calculated with the local density approximation (LDA) [27]. We note that the question of whether to use the LDA or GGA in the calculation is not clearcut. The top four layers in the slab were relaxed. We used the scalar-relativistic LDA pseudopotentials, and a plane wave basis with a lower cut off (26 Ry) and k-points sampling ($12 \times 12 \times 1$) for the geometry optimization. The MAE calculations were done on these optimized structures with higher plane wave cutoff.

For the MAE calculations, the interaction between the electrons and ions are described by fully relativistic ultrasoft pseudopotentials [39, 64] accounting for the SOC. We have done a set of self-consistent total energy calculations for various directions of magnetization and obtained the MAE as the difference between the energies corresponding to the easy and the hard directions, as introduced by Conte *et al.* [66]. A higher plane wave cut off of 40 Ry for the expansion of wavefunctions and 400 Ry for charge density is used to ensure accurate convergence of the MAE. A very fine sampling of the Brillouin zone (BZ) is required as the typical error due to insufficient BZ sampling can otherwise be of the same order as the MAE. We use a Monkhorst-pack grid of k-points [40]. Also, the value of smearing [44] is taken to be small, 0.0007 Ry. The exchange-correlation functional is approximated by the LDA [27]. The MAE is obtained by sampling the energy landscape for fixed directions of magnetization and is taken as the difference between the highest and the lowest total energies. The direction of magnetization is specified in the spherical polar coordinate frame with θ and ϕ as the polar and azimuthal angles, respectively.

Free-standing monoatomic wire and two-dimensional (square and triangular)

lattices are considered at various lattice spacings ranging from 1.5 Å to 3.5 Å. The convergence of the MAE with respect to k-points is carefully checked for all the structures.

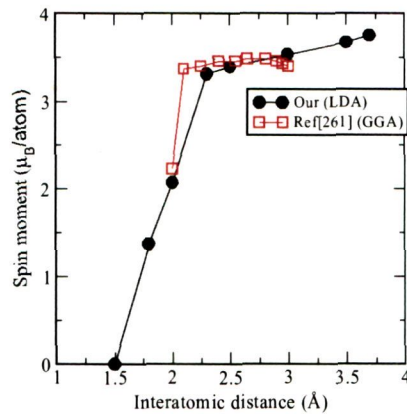
6.4 Results and Discussion

6.4.1 Fe Monoatomic Chain

Although an infinitely long free-standing monoatomic chain is an unrealistic system from the experimental view-point, it does provide insights about the underlying interactions and useful trends, when studied together with other systems, as a function of coordination and dimensionality. However, monoatomic chains of finite length have been observed in break-junctions for Au [275], Ir [276] and Pt [277]. To understand the evolution of MAE and the easy axis, we have considered Fe chain at various interatomic distances (from 1.5 Å to 3.7 Å).

To see how magnetic properties evolve with interatomic distance, we have plotted the spin moment of the Fe chain as a function of bond length in Fig. 6.1, comparing with the corresponding result from Ref [261]. Clearly, the spin magnetic moment calculated using LDA approaches its atomic value at much higher interatomic distance compared to the one calculated by the GGA.

Figure 6.1: Spin magnetic moments as a function of interatomic distance of Fe chain.



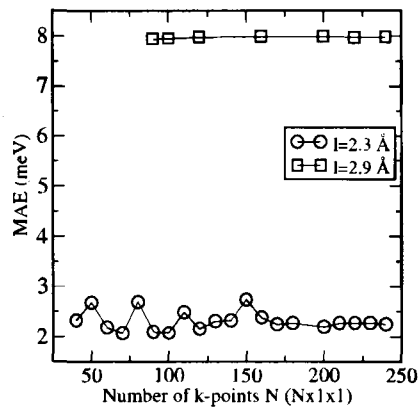
MAE: Convergence

Convergence of MAE of the wire with respect to k-points is shown in Fig. 6.2 for two interatomic distances (2.30 and 2.87 Å). The MAE of the chain with interatomic distance of 2.30 Å is well converged at 200 k-points in the BZ. For the wire at 2.87 Å, the MAE is already converged at even 100 k-points. We took a cautious choice of 250 k-points for further calculations of MAE at various interatomic distances.

MAE: Size Dependence

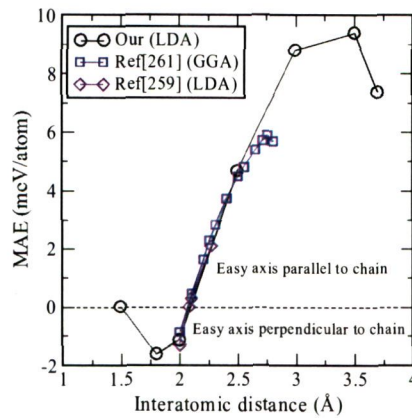
In Fig. 6.3 we show the MAE of monoatomic Fe chain calculated at various interatomic distances with the LDA, along with comparison from two references. For very short interatomic distance (1.5 Å), the Fe chain loses ferromagnetism and the MAE becomes zero. Beyond 1.5 Å, the Fe chain

Figure 6.2: Magnetic anisotropy energy (in meV per Fe atom) of isolated Fe chain at the interatomic distances of 2.3 and 2.87 Å with respect to the number of k-points in the one-dimensional Brillouin-zone.



acquires ferromagnetism (the moment is small though, about $1.3 \mu_B$ for the interatomic distance up to 2.0 \AA) and at about 1.8 \AA the easy axis is perpendicular to the chain. For distances larger than 2.0 \AA the easy axis switches to along the chain direction and the magnetic moment becomes large (about $3.0 \mu_B$). These behaviors agree with the literature [259, 261]. It can also be seen from Fig. 6.3 that the variation of MAE with interatomic distance is nearly unaffected by the exchange functional used (LDA or GGA). The MAE keeps increasing until 3.5 \AA , and the easy axis remains along the wire. The MAE starts decreasing beyond 3.5 \AA . Tung *et al.* [261] have also found this behavior but at a smaller value of interatomic distance: the MAE peaks at around 2.75 \AA and shows a decrease at a higher interatomic distance of 2.8 \AA .

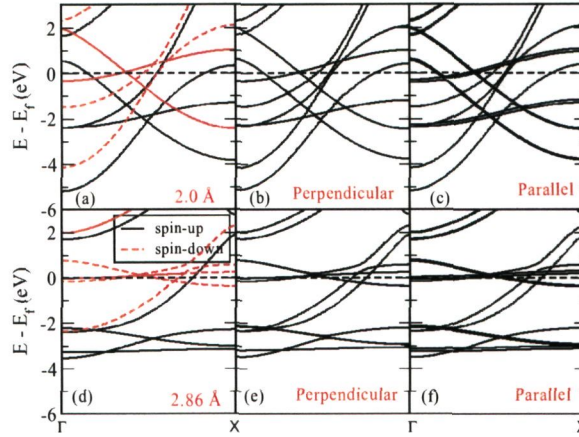
Figure 6.3: Variation of the magnetic anisotropy energy as a function of interatomic distance for the monoatomic Fe chain. Comparison with two previous references (employing different exchange-correlation functional, LDA (Ref [259]) and GGA (Ref [261])) is also made.



Band Structure and Density of States

We have done electronic band structure calculations for the Fe chain at two interatomic distances (2.0 and 2.86 Å) for two directions (perpendicular and along the chain axis) (Fig. 6.4). The scalar relativistic bands near the Fermi level can be grouped into three sets: the d_{z^2} and d_{zy} bands, the $d_{x^2-y^2}$ band and the degenerate (d_{xy} , d_{xz}) bands. The (d_{z^2} and d_{zy}) bands are narrow because they are perpendicular to the chain and hence do not overlap much. The other two sets of bands are formed from the overlapping orbitals which have a component of their lobes along the chain direction and hence are dispersive. The (d_{xy} , d_{xz}) bands are symmetric along the chain direction (hence degenerate) and are most dispersive. This can also be seen from the d -density of states shown in Fig. 6.5.

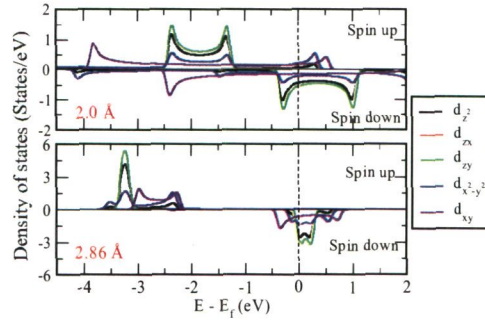
Figure 6.4: Electronic band structures of the monoatomic Fe chain at the interatomic distances of 2.0 Å (upper panel) and 2.86 Å (lower panel). (a) and (d) with scalar relativistic calculation; (b), (c), (e) and (f) with spin-orbit interaction taken into account. “Parallel and “Perpendicular denote the results from fully relativistic calculations with the magnetization parallel and perpendicular to the chain axis, respectively.



6.4.2 Free Standing Square Lattice of Fe atoms

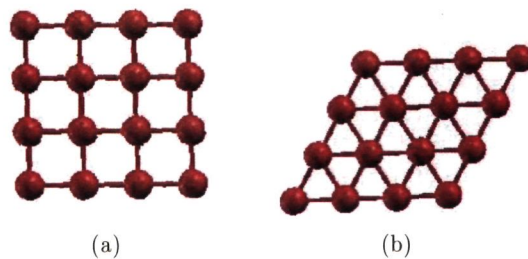
We considered unsupported two-dimensional triangular as well as simple square lattices (Fig. 6.6) of Fe at different NN separations. In Fig. 6.7, we have shown the convergence of MAE with respect to k-point sampling for the square lattice of Fe at its equilibrium NN distance (2.33 Å). We found that the MAE converges for about $90 \times 90 \times 1$ k-point mesh at this lattice constant. The easy axis is perpendicular to the plane and the MAE is 0.51 meV/atom. We also did an MAE calculation at a very slightly lower lattice constant of 2.31 Å and the MAE was found to be increased (0.59 meV/atom), showing the high sensitivity of the MAE with the NN distance.

Figure 6.5: Projected spin polarized density of states of Fe chains at two inter-atomic distances.



In Fig. 6.8 we show MAE values at different lattice constants. We observe that the MAE oscillates with the lattice constant. At 1.5 \AA the Fe square lattice, like the Fe chain, remains nonmagnetic. However, at 2.0 \AA unlike the chain, the square lattice remains almost nonmagnetic with an almost zero MAE (0.02 meV/atom). The MAE increases beyond 2.0 \AA and the easy axis becomes perpendicular to the plane. For larger lattice constants, although the easy axis remains perpendicular, we do not find a monotonic behavior of the MAE with lattice constant. In early calculations by Li *et al.* [268] using the LAPW method, the MAE was found to be about 0.04 meV and 0.03 meV/atom at Ag and Au lattice constants (2.89 and 2.88 \AA) respectively, and an in-plane easy axis was obtained. However, later calculations by Nakamura *et al.* [269] using FLAPW (LDA) calculations obtained a MAE of 0.24 meV/atom and an out-of-plane easy axis at the Ag lattice constant and 0.30 meV/atom , and an out-of-plane easy axis at the Cu(001) lattice

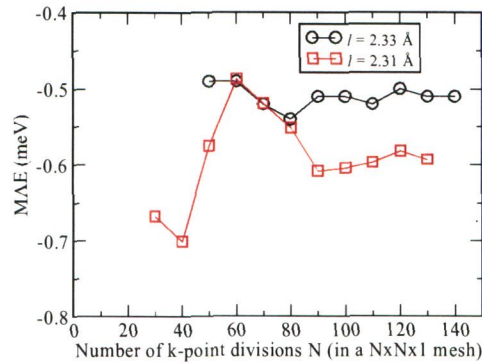
Figure 6.6: *Two-dimensional unsupported lattices of Fe. (a) square (b) triangular.*



constant (2.56 \AA). Our MAE values at the lattice constants of 2.5 and 2.88 \AA are 0.61 meV/atom and 0.25 meV/atom respectively. Our MAE value of 0.25 meV/atom at 2.88 \AA is in good agreement with that of Nakamura *et al.*'s value of 0.24 meV/atom .

We have also studied the change in MAE and the direction of easy axis as one goes from the square lattice to the 1D chain (Fig. 6.9). For this, we gradually increased one of the sides of the square. We see in Fig. 6.9 that as one of the lateral sides of the 2D lattice increases and consequently the 2D lattice approaches the 1D chain, the easy axis changes from out-of-plane to in-plane (along the chain axis). Interestingly, the value of MAE changes monotonically. At the perfect square of side 2.31 \AA the MAE is maximum (0.59 meV/atom); it decreases with increasing one of the sides and crosses zero when this side becomes about 1.35 times larger. Then apparently the geometry becomes more like a 1D than a 2D system, and the system behaves like a monoatomic chain with the direction of the easy axis along the chain axis.

Figure 6.7: Magnetic anisotropy energy (MAE) (in meV per Fe atom) of simple square lattice (for two values of nearest-neighbor distances: 2.33 and 2.31 Å) with respect to the size of the two-dimensional k-point mesh.



Electronic Band Structure

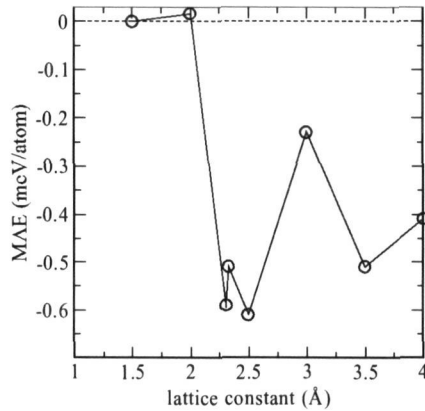
Fig. 6.10 shows the band structure of the square lattice at 2.33 Å and 2.86 Å for the two directions, perpendicular and parallel to the plane along with the scalar relativistic spin-polarized band structures. The band structures calculated with the spin-orbit interaction taken into account do not show any perceptible difference for the two directions of magnetization for a given value of the lattice constant. Fig. 6.11 shows the d -decomposed density of states for the two lattice constants.

6.4.3 Free Standing Triangular Lattice

MAE: Convergence

We also considered a triangular lattice at two lattice constants. Fig. 6.12 shows convergence of the MAE for the triangular lattice at 2.31 and 2.86 Å.

Figure 6.8: Change in MAE as a function of interatomic distance for the monoatomic Fe square lattice.



The easy axis is found to be out-of-plane, as for the square lattice. Here also one can see that the convergence of the MAE is achieved at lower number of k-points for a lattice at larger NN distance compared to the one at smaller NN distance. The converged values of the MAE for the triangular lattice are 0.97 and 0.18 meV/atom respectively at NN distances of 2.31 and 2.86 Å.

MAE: Size Dependence

In Table 6.1 we show the MAE of the triangular lattice for three NN distances. Like the square lattice, the triangular lattice also shows a non-monotonic behavior of the MAE with respect to the lattice constant. The easy axis is always out-of-plane, as found for the square lattice. This is in contrast to a free-standing Co monolayer which shows an in-plane anisotropy. In Table 6.1 we have shown also a comparison of the MAE for the free-standing triangular, square and monoatomic chain at these lattice constants. This can illustrate

Figure 6.9: Change in MAE and the direction of easy axis when one of the lateral sides of the square lattice is increased such that the 2D square lattice effectively becomes a 1D chain.

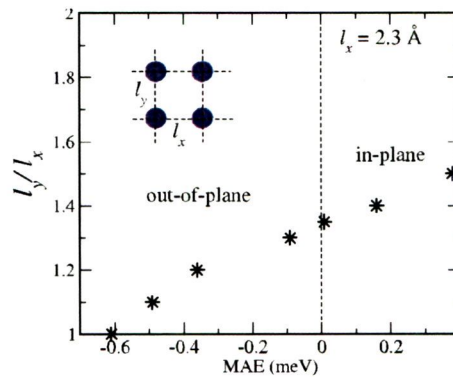
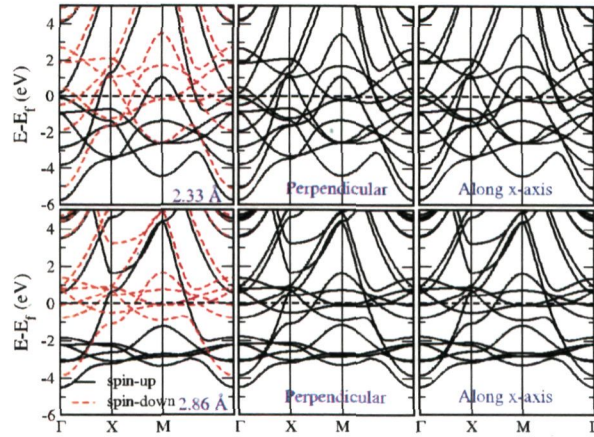


Table 6.1: Comparison of MAEs of chain, square and triangular lattices at three lattice constants.

a (Å)	MAE (meV/atom)		
	Triangular	Square	Chain
2.31	1.0	0.6	2.3
2.33	1.0	0.5	2.6
2.86	0.2	0.3	8.0

the effect of coordination number on the MAE. The coordination numbers of the triangular, square and chain are six, four and two respectively. Only at a large NN distance of 2.86 Å do we find a trend in the MAE with respect to the coordination number: the lower the coordination, the larger the MAE. The MAE of the chain is always the largest among the three. Comparing to the square lattice, the MAE values for the triangular lattice at the smaller NN distances (2.31 and 2.33 Å) have increased.

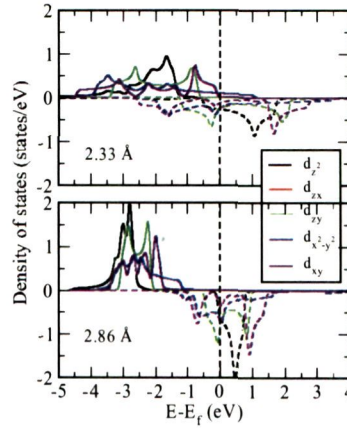
Figure 6.10: Electronic band structure of the square lattice at the lattice constant of 2.33 \AA (upper panel) and 2.86 \AA (lower panel). In the left column we show the scalar relativistic, spin polarized band structure. In the middle and the right columns, the band structure for the perpendicular and the in-plane (along the x axis) magnetization directions are respectively shown.



Electronic Band Structure and Density of States

We also have calculated the electronic band structure of the triangular lattice at lattice constants of 2.31 and 2.86 \AA (Fig. 6.13) for the in-plane (along the x -axis) and out-of-plane directions. The bands can be grouped into three sets in this case also: d_{z^2} band, the degenerate (d_{zx}, d_{zx}) bands and the degenerate ($d_{x^2-y^2}, d_{xy}$) type bands. The d_{z^2} band is the least dispersive due to less overlap (it is perpendicular to the plane of the lattice). The degenerate ($d_{x^2-y^2}, d_{xy}$) bands are the most dispersive due to their entirely planar overlap. In Fig. 6.14, we have plotted the spin polarized density of states for this system. In this case also, the band structures for the in-plane and the out-of-plane directions of magnetization do not show any noticeable

Figure 6.11: Projected partial spin polarized density of states of Fe square lattice at two lattice constants.

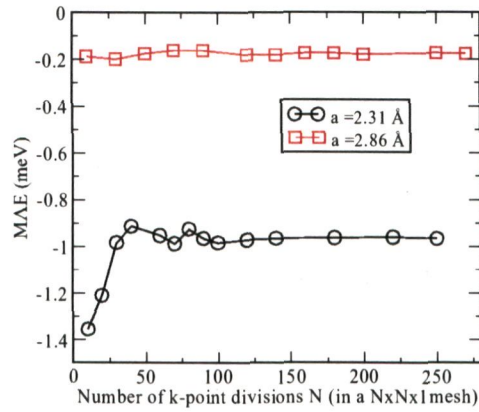


difference.

6.4.4 Fe/Au(111) System

After studying the magnetic anisotropy of the free-standing monolayer of Fe, we deposited it on the Au(111) substrate to study the effect of the substrate. We have taken six layers of Au(111) and one layer of Fe (Fig. 6.15) and considered various stacking possibilities, as for the pseudomorphic Co/Au(111) system. The top surface of Au(111) has been observed to have regions where surface atoms sit on the fcc site as well as regions where atoms sit on the hcp sites. Keeping this in view, we considered in addition to the normal fcc (111) stacking (denoted as ABCABC), a hcp stacking, where only the top layer atoms of the substrate occupy hcp sites (ABCABA). On both types of the

Figure 6.12: Magnetic anisotropy energy (MAE) (in meV per Fe atom) of triangular lattice at lattice constant $a = 2.31$ and 2.86 Å with respect to the size of the two-dimensional k-points mesh.

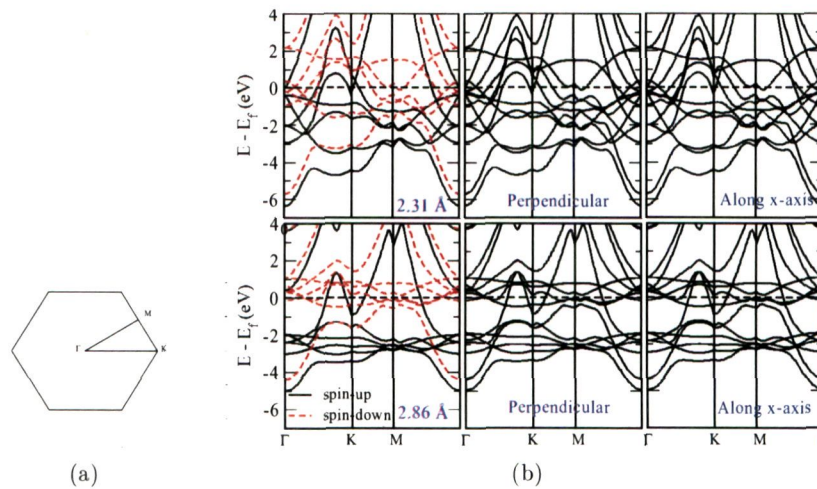


substrate stacking, the Fe overlayer can be put on either of the two available sites. Thus we have in total four types of stackings of Fe/Au(111) system denoted as case(i) (ABCABCA), case(ii) (ABCABAC), case(iii) (ABCABCB) and case(iv) (ABCABAB). In the next section we describe and compare the energetics and the magnetic moments for the four cases.

Stability and Magnetism: Scalar Relativistic Calculation

The intralayer NN distance is 2.86 Å. The interlayer relaxations, magnetic moments and relative stabilities of the four configurations considered are tabulated in Table 6.2. The hcp site is found to be only slightly higher (1 mRy) in energy than the fcc site [284]. We see that the case(i) is the most stable which corresponds to the fcc stacking of both the Au(111) and the overlayer Fe. The order of stability of Fe/A(111) is the same as that of the

Figure 6.13: (a) The Brillouin zone of a triangular lattice. (b) the scalar relativistic (first column) and the spin-orbit split electronic band structures (second and third columns) of the triangular lattice at the lattice constants of 2.31 Å (upper panel) and 2.86 Å (lower panel). The scalar relativistic bands are calculated for both the spin up and spin down channels. The spin-orbit split bands are calculated for two directions, one in-plane (along the x-axis) and the other perpendicular to the plane (along the z axis).



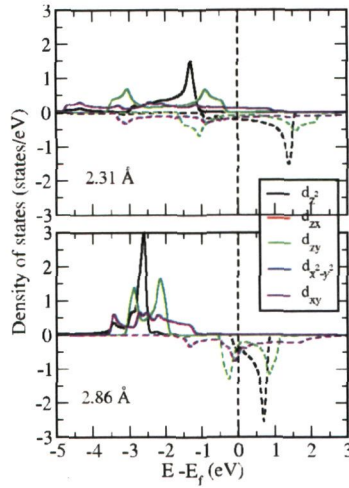
1 ML pseudomorphic Co/Au(111): case(i) > case(ii) > case(iii) > case(iv).

The Fe-Au distance, however, is slightly larger (2.03 Å) compared to the Co-Au distance (1.97 Å).

MAE: Convergence with respect to Brillouin zone sampling

The convergence of the MAE with respect to the number of k-points for the case(i), case(ii) and case(iii) are shown in Figs. 6.16 - 6.18. The variations of the total energy difference taken for the magnetization along two directions: $(\theta, \phi) = (0^\circ, 0^\circ)$ and $(90^\circ, 90^\circ)$ for the case(i) and $(0^\circ, 0^\circ)$, $(90^\circ, 0^\circ)$ for the

Figure 6.14: Projected spin polarized density of states of triangular Fe lattice calculated at lattice constants of 2.31 and 2.86 Å.



case(ii) and case(iii) respectively with respect to the size of the k-point mesh for the Brillouin zone integration are shown in Fig. 6.16 (for case(i)), Fig. 6.17 (for case(ii)) and Fig. 6.18 (for case(iii)). It is clear from Fig. 6.16 that there are large fluctuations in the energy difference when it is calculated at lower number of k-points in the Brillouin zone. It should be noted that although the anisotropy energy fluctuates, a change in sign does not happen. For the k-point convergence, as given in Fig. 6.16 and Fig. 6.18, we considered different in-plane directions for the case(i) and case(iii): y -axis for case(i) and x -axis for case(iii). The three cases show that the stable direction of magnetization is in-plane for the case(i) while it is out-of-plane for the case(ii) and case(iii). However, the final knowledge about the direction of easy and hard axes can only be ascertained after we do a sampling of total energy with respect to possible orientations of magnetization. The anisotropy energy starts

Figure 6.15: Side view of the Fe/Au(111) system. The spheres of red and yellow colors correspond respectively to Fe and Au atoms.

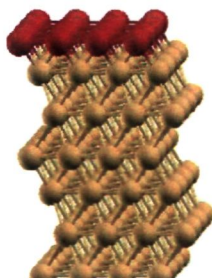


Table 6.2: Interlayer relaxed distance d (in \AA), magnetic moment (in μ_B/Fe atom) and the stability ΔE (meV) of the four configurations relative to the most stable one (case(i)).

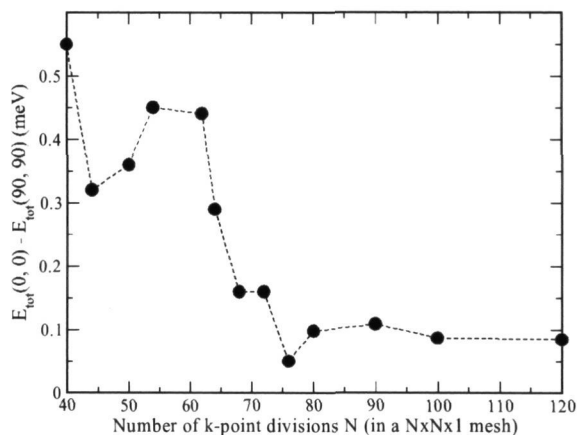
	Case(i)	Case(ii)	Case(iii)	Case(iv)
$d_{\text{Fe}_1-\text{Au}_1}$	2.03	2.02	2.05	2.04
$d_{\text{Au}_1-\text{Au}_2}$	2.36	2.36	2.38	2.39
$d_{\text{Au}_2-\text{Au}_3}$	2.33	2.34	2.35	2.36
Moment	3.15	3.14	3.15	3.05
ΔE	0.0	10.07	25.77	34.16

converging only beyond a k-point mesh of $(80 \times 80 \times 1)$ for cases (i) and (iii) but it has not converged for case(iii) even at a k-point mesh of $(130 \times 130 \times 1)$. We have taken for further calculations, a mesh value of $(84 \times 84 \times 1)$, which corresponds to 1830 k-points in the irreducible Brillouin zone.

Angular Dependence of MAE

As mentioned before, to know the direction of easy and hard axes, one needs to sample the total energy at many directions of magnetization and the lowest and the highest energies among the sampled set will correspond to the easy

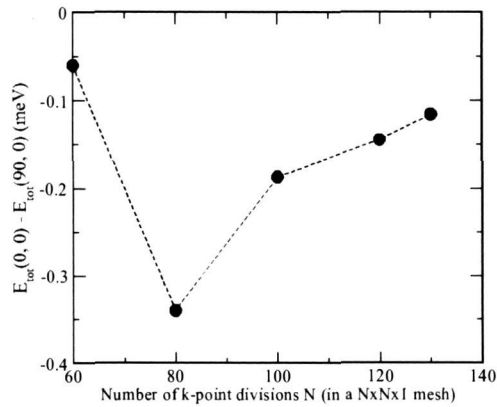
Figure 6.16: MAE convergence with respect to k-points for monolayer Fe/Au(111) for case(i) (fcc stacking of Fe). The MAE value is in meV per Fe atom.



and hard axes respectively. We have studied the MAE as a function of magnetization direction for two cases (i and iii) (Fig. 6.19-6.20). We have considered seven directions including one normal to the plane (i.e., along the z axis, $(0^\circ, 0^\circ)$) and two in the plane (along the x and y axes) $(90^\circ, 0^\circ)$ and $(90^\circ, 90^\circ)$. The other four directions correspond to the tilted axis of magnetization: tilted 30° and 60° from the normal with projection on the x - y plane along the x and y directions. We took the converged k-point mesh of $(84 \times 84 \times 1)$ for these calculations.

The results (Figs. 6.19-6.20) are interesting: for the fcc case (case(i)), the easy axis is tilted 30° from the normal while for the hcp case (case(iii)) the easy axis is along the normal. Even for the hcp case, the total energy remains very close to the energy corresponding to the easy axis direction, for angular tilt of around 30° from the normal (Fig. 6.20). The hard axis, however, lies

Figure 6.17: MAE convergence with respect to k -points for monolayer Fe/Au(111) for case(ii) (fcc stacking of Fe, hcp stacking of the topmost Au). The MAE value is in meV per Fe atom.

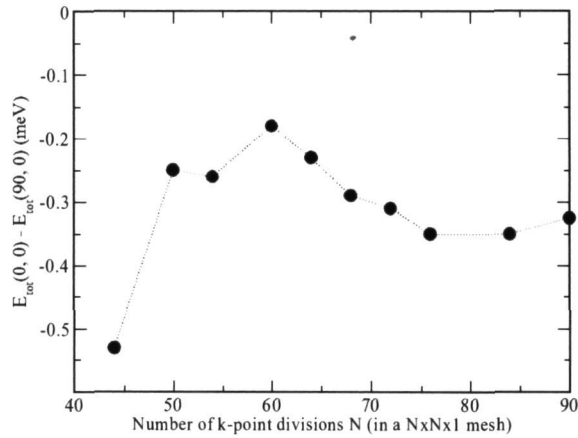


in-plane (along the y axis) for both the cases.

The value of the MAE for case(i) is 0.15 meV/Fe atom and for case(iii) is 0.35 meV/Fe atom. Comparing these values with that of the free-standing triangular lattice at the Au lattice constant (2.86 \AA), we find that the MAE is extremely sensitive to the site occupancy and the layer stacking of the substrate: For case(i), the MAE has slightly decreased from the free-standing value of 0.18 meV while it has become enhanced for case(iii).

Also, the results show that the direction of the easy axis depends on the site occupancy (fcc versus hcp) and layer stacking. As pointed out earlier, it has been observed in some experiments [279] that the easy axis was not strictly perpendicular but actually distributed in a cone about the normal direction. As in the experimental samples, there are always some variations in the film morphology with respect to the site occupancy and layer stackings,

Figure 6.18: MAE convergence with respect to k -points for monolayer Fe/Au(111) for case(iii) (hcp stacking of Fe). The MAE value is in meV per Fe atom.

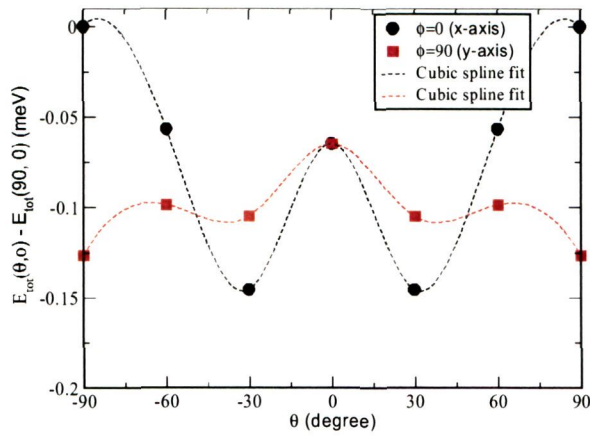


our results can explain the distributed easy axis found in the experiments.

6.5 Summary

We have studied magnetic anisotropy energy of Fe systems in low dimensions, namely, the monoatomic chain (1D), free-standing square and triangular lattices (2D) and pseudomorphic Fe monolayer on Au(111). We carefully checked the convergence of MAE with respect to the number of k -points in the Brillouin zone for all the systems. For the free-standing chain, the triangular and square lattices, we also studied the effect of interatomic spacing on MAE and the direction of easy axis. The Fe chain shows a nonmagnetic state at very small interatomic spacing of 1.5 \AA . Increasing the interatomic distance, the chain acquires small spin magnetic moments and the easy axis

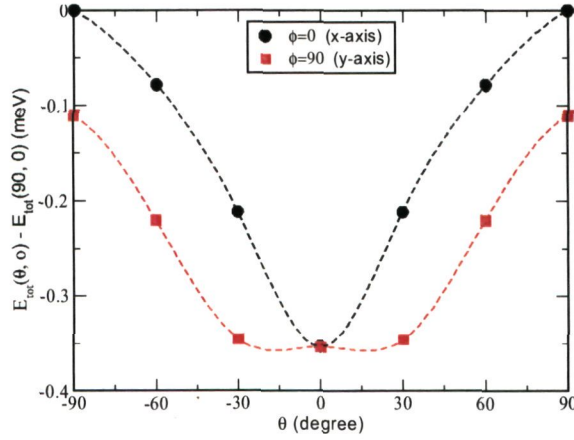
Figure 6.19: Magnetic anisotropy energy (MAE) (in meV per Fe atom) for the Fe/Au(111) for the case(i) (fcc) with the hard direction of magnetization (90° , 0°) taken as the reference energy. The dashed lines are spline fits as a guide to the eye, and should not be taken to represent mathematical functions. For example, the true maximum presumably occurs at $\theta=90^\circ$.



gets perpendicular to the chain axis. For interatomic distances larger than 2.0 \AA the easy axis switches to along the chain axis and magnetic moment also increases. The MAE keeps on increasing with interatomic distance up to 3.5 \AA and thereafter starts decreasing.

For the free-standing simple square lattice, we find an out-of-plane orientation of the easy axis at all the considered distances. For very small nearest-neighbor distances ($\leq 2.0 \text{ \AA}$), however, the square lattice becomes nonmagnetic. We do not find a monotonic relation of MAE with lattice constant for the square lattice. We also studied the evolution of MAE and the easy axis as one goes from the 2D square lattice to effectively 1D chain. Interestingly we find that the MAE monotonically decreases as we increase one of the sides

Figure 6.20: Magnetic anisotropy energy (MAE) (in meV per Fe atom) for the Fe/Au(111) for the case(iii) (hcp) with the hard direction of magnetization ($\theta=90^\circ$, $\phi=0^\circ$) taken as the reference energy. The dashed lines are spline fits.



(l_y) of the square, crosses zero at about $l_y/l_x = 1.35$, and again increases (and the easy axis becomes along the chain axis) as we enter the 1D regime. For the free-standing triangular Fe lattice also, we find an out-of-plane easy axis and a non-monotonic behavior of MAE with lattice constant (we considered just three interatomic distances for this lattice).

The free-standing triangular lattice, square lattice and monoatomic chain respectively have a coordination number of six, four and two. We compared the MAEs for these three structure at fixed interatomic distances to see if there is any trend in MAE with respect to the coordination number (which is generally observed in magnetic moments, i.e., magnetic moments increase with decreasing coordination). However, we do not find any such trend in the MAE (possibly due to the non-monotonic behavior of MAE with respect to interatomic distance, in the case of square and triangular lattices).

For the Fe/Au(111) system, we considered four stacking sequences involving the six-layer Au substrate and a monolayer of Fe over Au(111). We compared stability, interlayer relaxations and magnetic moments for the four cases of stacking and found that the stacking in which all the Au layers are arranged in fcc stacking and the Fe monolayer is put on the fcc site on the Au(111), is the most stable. After ensuring the MAF convergence, we sampled the total energies in different orientations of magnetization and determined the easy and the hard axis for the Fe/Au(111) corresponding to two stackings, case(i) and case(iii), the latter corresponds to a stacking in which the overlayer Fe atoms occupy the hep sites on the fcc stacked Au(111). The easy axis is out-of-plane for the case(i) and tilted 30° from the normal for case(iii), while the hard axis is in-plane (along the y axis) for both the systems. This particular finding is very interesting as experiments on Fe/Au(111) system indeed reveal an easy direction of magnetization which is not just out of plane but rather distributed in a cone around the out-of-plane direction.

Chapter 7

Summary and Conclusions

The main motive of this thesis has been to understand the effect of reduced dimensionality and reduced coordination on the structural and magnetic properties of transition metal systems. In addition to studying the changes in the magnetic moments, we also investigated the behavior of another important magnetic property called the magnetic anisotropy energy, in reduced dimensions. All these properties crucially depend on the electronic structure, a detailed and accurate description of which becomes necessary in order to obtain the correct picture. The quantum mechanical calculations from first-principles are the most accurate way of doing studies of structures and magnetic interactions at atomic length-scale. We used state-of-the-art density functional theory (DFT) in all our calculations. The DFT is currently the most accurate approach of dealing with extended materials at the electronic level.

The first-principles studies provide a useful tool to assist and complement

the experimental findings. Many issues which remain unresolved in experiments can be resolved in theory by a systematic study of the influences of various factors involved. In this way, we could resolve the experimental uncertainty regarding the sources of enhanced magnetic coercivity in the thiol/Co/Au(111) system. We predicted that the increased coercivity after thiol adsorption on the Co/Au(111) is not due to the increased magnetic anisotropy energy, but may rather be due to the morphological changes in the Co/Au(111) film. We also resolved the experimental discrepancy regarding the easy axis of the Fe/Au(111) system. We showed that how, for a given system, a change in the layer stacking and the site occupancy can result in a change in the MAE and the direction of the easy axis.

The magnetic and structural properties depend on the dimensionality and coordination. Whereas for some properties such as magnetic moment, a clear trend with respect to the dimensionality and coordination is shown, for the properties such as the magnetic anisotropy, which are very sensitive to the details of the band structure, it is very hard to make a general statement about any trend. Specifically, we find that bond lengths in general decrease in low dimensions and in reduced coordinations while the magnetic moments show an increase. For the magnetic anisotropy, however, it is difficult to find any such trend.

In the case of surface alloys, although we do not have a direct experimental comparison for our systems, we indeed find for the Co-Ag alloys on a very similar substrate, viz. Ru(0001), that it did not show atomic level mixing. Also, the trend in the magnetic moments of the alloys whose components not only differ in size but also belong to different rows and columns of the periodic

table, we could finally find a nice trend as a function of the number of valence electrons. This also highlights the fact that a seemingly complex looking pattern (of magnetic moments of surface alloys) can find its explanation in something as simple as the number of valence electrons.

Although our study provides some basic understanding of the structural and magnetic properties of systems which are of technological relevance, there are still some questions that need to be addressed before one could arrive at a final conclusion about the properties predicted by our work. We did a preliminary study of only small systems in idealized structures. For example, in the study of surface alloys we considered only the pseudomorphic structures. In real experimental systems, the presence of a finite temperature and structural reconstruction may lead to altered stability compared to the stability predicted by us. This may particularly be the case for the Pb alloys. Also, we considered only small unit cells consisting of a maximum of four surface atoms. Taking a larger unit cell may also result in some different preferences for structure and magnetism. Also, we studied only the ferromagnetic states and did not consider antiferromagnetic or any noncollinear magnetic states for our surface alloys. The consideration of these noncollinear states may also alter the observed trends in the stability and magnetic moments.

For the study of methanethiolate adsorbed Co/Au(111) system, we did not take into account the van der Waals interaction to relax the geometry. The inclusion of this interaction may lead to a different geometry, which in turn might modify the magnetic anisotropy results. However, we must note that with the current theoretical framework, it was not possible to include this

dispersive interaction in our calculations: the current formulations (semi-empirical dispersion correction, DFT-D [285], and van der Waals density functionals, vdW-DF [286]) work only for the nonmagnetic systems. Nevertheless, van der Waals interaction with spin polarization has been implemented in some codes such as VASP, but such calculations carry no theoretical justification. It is not implemented in Quantum ESPRESSO. Therefore, currently it is not possible to see the effect of van der Waals interaction on magnetic anisotropy.

Nevertheless, it is known [287] that this interaction becomes important for longer chain molecules and at higher surface coverages. Since we considered only a small molecule (containing just one carbon atom) and the surface coverage is also not very high, we believe that the inclusion of van der Waals interaction would not be very important in our system.

In the study of magnetic anisotropy energy, we have considered only the spin-orbit contribution. The dipolar magnetic interaction responsible for the shape anisotropy, which becomes important for thicker films, is not considered by us. We also have not studied the correlation of the magnetic anisotropy with the orbital moment. It would also be interesting to determine more precisely the role of the Au(111) substrate in the determination of easy axis and the magnetic anisotropy energy. The change in the magnetic anisotropy should be also studied for thicker Co and Fe films on Au(111).

In future work we would like to study the magnetic anisotropy properties of some suitable surface alloys e.g., Fe-Au/Rh(111). Since the MAE calculations become prohibitively expensive due to the requirement of a very fine sampling of the Brillouin zone and a full self-consistent calculation at each point in the

irreducible Brillouin zone, some interpolation schemes (such as the Wannier interpolation) which would reduce the cost of these calculation are desirable to implement for any future calculation of the magnetic anisotropy energy.

Bibliography

- [1] H. Dreyseé and C. Demangeat, *Surf. Sci. Rep.* **28**, 65 (1997).
- [2] E. Dagotto, *Rev. Mod. Phys.* **66**, 763 (1994).
- [3] W. A. de Heer, P. Milani, and A. Chatelain, *Phys. Rev. Lett.* **65**, 488 (1990).
- [4] J. P. Bucher, D. C. Douglass, and L. A. Bloomfield, *Phys. Rev. Lett.* **66**, 3052 (1991).
- [5] I. M. L. Billas, J. A. Becker, A. Chatelain and W. A. de Heer, *Science* **265**, 1682 (1994).
- [6] A. N. Andriotis, and M. Menon, *Phys. Rev. B* **59**, 15942 (1999).
- [7] C. Barreteau, R. Guirado-López, D. Spanjaard, M. C. Desjonquères, and A. M. Oleś, *Phys. Rev. B* **61**, 7781 (2000).
- [8] F. Aguilera-Granja, J. L. Rodríguez-López, K. Michaelian, E. O. Berlanga-Ramírez, and A. Vega, *Phys. Rev. B* **66**, 224410 (2002).
- [9] M. Albrecht, U. Gradmann, T. Furubayashi, W. A. Harrison, *Europhys. Lett.* **20**, 65 (1992).

-
- [10] A. J. Freeman, and R. Wu, *J. Magn. Magn. Mater.* **100**, 497 (1991).
- [11] A. J. Freeman, and R. Wu, *J. Magn. Magn. Mater.* **200**, 498 (1999).
- [12] O. Hjortstam, J. Tyregg, J. M. Willis, B. Johansson, and O. Eriksson, *Phys. Rev. B* **53**, 9204 (1996).
- [13] B. T. Jonker, K. -H. Walker, E. Kisker, G. A. Prinz, and C. Carbonc, *Phys. Rev. Lett.* **57**, 142 (1986) .
- [14] B. Heinrich, K. B. Urquhart, A. S. Arrott, J. F. Cochran, K. Myrtle, and S. T. Purcell, *Phys. Rev. Lett.* **59**, 1756 (1987).
- [15] A. Lehnert, S. Dennler, P. Błoński, S. Rusponi, M. Etzkorn, G. Moulas, P. Bencok, P. Gambardella, H. Brune, and J. Hafner, *Phys. Rev. B* **82**, 094409 (2010).
- [16] J. C. Lodder, *Hand Book of Magnetic Materials*, Vol 11, North Holand, 297 (1998).
- [17] C. F. Hirjibchedin, Chiung-Yuan Lin, A. F. Otte, M. Ternes, C. P. Lutz, B. A. Jones, and A. J. Heinrich, *Science* **317**, 1199 (2007).
- [18] S. Loth, S. Baumann, C. P. Lutz, D. M. Eigler, and A. J. Heinrich, *Science* **335**, 196 (2012).
- [19] C. L. Kane and E. J. Mele, *Phys. Rev. Lett.* **95**, 226801 (2005)
- [20] J. E. Moore and L. Balents, *Phys. Rev. B* **75**, 121306 (2007).
- [21] B. A. Bernevig, T. L. Hughes, S. -C. Zhang, *Science* **314**, 1757 (2006).

-
- [22] M. König, S. Wiedmann, C. Brüne, A. Roth, H. Buhmann, L. W. Molenkamp, X. -L. Qi and S. -C. Zhang, *Science* **318**, 766 (2007).
- [23] P. Hohenberg and W. Kohn, *Phys. Rev.* **136**, B864 (1964).
- [24] W. Kohn and L. J. Sham, *Phys. Rev.* **140**, A1133 (1965).
- [25] J. L. Balduz, *Phys. Rev. Lett.* **49**, 1691 (1982).
- [26] M. Levy and J. P. Perdew, V. Sahni *Phys. Rev. B* **30**, 2745 (1984).
- [27] R. O. Jones and O. Gunnarsson, *Rev. Mod. Phys.* **61**, 689 (1989).
- [28] J. P. Perdew and Y. Wang, *Phys. Rev. B* **46**, 12947 (1992).
- [29] P. A. M. Dirac, *Proc. Cambridge Phil. Soc.* **26**, 376 (1930).
- [30] D. M. Ceperley and B. J. Alder *Phys. Rev. Lett.* **45**, 566 (1980).
- [31] D. D. Johnson, *Phys. Rev. B* **38**, 12807 (1988).
- [32] A. D. Becke, *J. Chem. Phys.* **38**, 3098 (1988).
- [33] J. P. Perdew, K. Burke, and M. Ernzerhof, *Phys. Rev. Lett.* **77**, 3865 (1996).
- [34] J. P. Perdew, K. Burke, and M. Ernzerhof, *Phys. Rev. Lett. (E)* **78**, 1396 (1997).
- [35] J. C. Phillips, *Phys. Rev.* **112**, 685 (1958).
- [36] J. C. Phillips and L. Kleinman, *Phys. Rev.* **116**, 287 (1959).
- [37] M. L. Cohen and V. Heine, *Solid State Physics* **24**, 37 (1970).

-
- [38] G. B. Bachelet, D. R. Hamann, and M. Schluter, *Phys. Rev. B* **26**, 4199 (1982).
- [39] D. Vanderbilt, *Phys. Rev. B* **41**, 8412 (1990).
- [40] H. J. Monkhorst and J. D. Pack, *Phys. Rev. B* **13**, 5188 (1976).
- [41] D. J. Chadi and M. L. Cohen, *Phys. Rev. B* **8**, 5747 (1973).
- [42] N. Mermin, *Phys. Rev.* **137**, A1441 (1965).
- [43] C. L. Fu and K. M. Ho, *Phys. Rev. B* **28**, 5480 (1983).
- [44] M. Methfessel and A. T. Paxton, *Phys. Rev. B* **40**, 3616 (1989).
- [45] N. Marzari, D. Vanderbilt, A. D. Vita, and M. C. Payne, *Phys. Rev. Lett.* **82**, 3296 (1999).
- [46] R. P. Feynman, *Phys. Rev.* **56**, 340 (1939).
- [47] P. Pulay, *Mol. Phys.* **17**, 197 (1969).
- [48] M. Scheffler, J.-P. Vigneron and G. B. Bachelet, *Phys. Rev. B* **31**, 6541 (1985).
- [49] S. Baroni, S. de Gironcoli and A. Dal Corso, *Rev. Mod. Phys.* **73**, 515 (2001).
- [50] O. H. Nielsen and R. M. Martin, *Phys. Rev. Lett.* **50**, 697 (1983).
- [51] M. Bernasconi, G. L. Chiarotti, P. Focher, S. Scandolo, E. Tosatti and M. Parrinello, *J. Phys. Chem. Solids* **56**, 501 (1995).

-
- [52] U. von Barth and L. Hedin, *J. Phys. C* **5**, 1629 (1972).
- [53] S. H. Vosko, L. Wilk, and M. Nusair, *Can. J. Phys.* **58**, 1200 (1980).
- [54] J. P. Perdew and A. Zunger, *Phys. Rev. B* **23**, 5048 (1981).
- [55] J. P. Perdew *et. al.*, *Phys. Rev. B* **46**, 6671 (1992); *Phys. Rev. B* **48**, 4978 (1993).
- [56] M. Weissbluth, *Atoms and Molecules*, Academic Press (1978).
- [57] J. Kübler, K.-H. Höck, J. Sticht, and A. R. Williams, *J. Phys. F: Met. Phys.* **18**, 469 (1988).
- [58] D. M. Bylander and L. Kleinman, *Phys. Rev. B* **58**, 9207 (1998).
- [59] A. M. Conte, Ph.D. thesis, *SISSA, Italy* (2007).
- [60] P. Nichols, N. Govind, E. J. Bylaska and W. A. de Jong, *J. Chem. Theory Comput.* **5** (3), 491 (2009).
- [61] L. A. Hemstreet, C. Y. Fong, and J. S. Nelson, *Phys. Rev. B* **47**, 4238 (1993).
- [62] G. Theurich and N. A. Hill, *Phys. Rev. B* **64**, 073106 (2001).
- [63] G. Theurich and N. A. Hill, *Phys. Rev. B* **66**, 115208 (2002).
- [64] A. D. Corso and A. M. Conte, *Phys. Rev. B* **71**, 115106 (2005).
- [65] P. Pyykkö, *Chem. Rev.* **88**, 563 (1988).
- [66] A. M. Conte, S. Fabris and S. Baroni, *Phys. Rev. B* **78**, 014416 (2008).

-
- [67] <http://www.quantum-espresso.org/>
- [68] E. C. Stoner, Proc. R. Soc. London Ser. A **169**, 339 (1939).
- [69] G. Stollhoff, A. M. Oleś, and H. Heine, Phys. Rev. B **41**, 7028 (1990).
- [70] A. R. Williams, R. Zeller, V. L. Moruzzi, C. D. Gelatt, and J. Kubler, J. Appl. Phys. **52**, 2067 (1981).
- [71] C. Kittel, Introduction to Solid State Physics, 8th ed., Wiley, Hoboken, NJ, (2005).
- [72] M. N. Huda, M. K. Niranjan, B. R. Sahu, and L. Kleinman, Phys. Rev. A **73**, 053201 (2006).
- [73] P. B. Dayal, B. R. Mehta, and P. D. Paulson, Phys. Rev. B **72**, 115413 (2005).
- [74] G. Nicolay, F. Reinert, and S. Hüfner, Phys. Rev. B **65**, 033407 (2001).
- [75] H. Cercellier, Y. Fagot-Recurat, B. Kierren, F. Reinert, D. Popović, and D. Malterre, Phys. Rev. B **70**, 193412 (2004).
- [76] G. Schütz, W. Wagner, W. Wilhelm, P. Kienle, R. Zeller, R. Frahm, and G. Materlik, Phys. Rev. Lett. **58**, 737 (1987).
- [77] C. R. Ast, J. Henk, A. Ernst, L. Moreschini, M. C. Falub, D. Pacilè, P. Bruno, K. Kern, and M. Grioni, Phys. Rev. Lett. **98**, 186807 (2007).
- [78] N. S. Akulov, Zeits. f. Physik **67**, 794 (1931).

-
- [79] R. M. Bozorth, *Phys. Rev.* **50**, 1076 (1936); *J. App. Phys.* **8**, 575 (1937).
- [80] J. H. van Vleck, *Phys. Rev.* **52**, 1178 (1937).
- [81] F. Bloch, G. Gentile, *Z. Phys.* **70**, 395 (1931).
- [82] H. Brooks, *Phys. Rev.* **58**, 909 (1940).
- [83] R. Raghunathan, S. Ramasesha and D. Sen, *Phys. Rev. B* **78**, 104408 (2008).
- [84] A. K. Rajagopal and J. Callaway, *Phys. Rev. B* **7**, 1912 (1973).
- [85] A. H. MacDonald and S. H. Vosko, *J. Phys. C* **12**, 2977 (1979).
- [86] J. Koringa, *Physica (Amsterdam)* **13**, 392 (1947).
- [87] W. Kohn and N. Rostoker, *Phys. Rev.* **94**, 1111 (1954).
- [88] O. K. Andersen, *Phys. Rev. B* **12**, 3060 (1975).
- [89] J. Trygg, B. Johansson, O. Eriksson, J. M. Wills, *Phys. Rev. Lett.* **75**, 2871 (1995).
- [90] Y. Xie and J. A. Blackman, *Phys. Rev. B* **69**, 172407 (2004).
- [91] L. Kleinman, *Phys. Rev. B* **21**, 2630 (1980).
- [92] A. Christensen, A. V. Ruban, P. Stoltze, K. W. Jacobsen, H. L. Skriver, J. K. Nørskov, and F. Besenbacher, *Phys. Rev. B* **56**, 5822 (1997).
- [93] J. H. Sinfelt, *Surf. Sci.* **500**, 923 (2002).

-
- [94] J. G. Chen, C. A. Menning, and M. B. Zellner, *Surf. Sci. Rept.* **63**, 201 (2008).
- [95] A. Gross, *Top. Catal.* **37**, 29 (2006).
- [96] H. Hoster, and R. J. Behm In: M. T. M. Koper, Editor, *Fuel Cell Catalysis: A Surface Science Approach*, Wiley & Sons, Chichester (2008).
- [97] J. Hornlike, T. Y. Lee, K. Junker, A. Endears, R. Skims, S. Binman, S. Maniocs, J. Mina, J. Stanton, H. Ebert, M. Hessler, K. Fauth, G. Schütz, A. Buchsbaum, M. Schmid, P. Varga, and K. Kern, *Phys. Rev. Lett.* **102**, 067207 (2009).
- [98] J. Q. Xiao, J. S. Jiang, and C. L. Chien, *Phys. Rev. Lett.* **68**, 3749 (1992).
- [99] V. Jaccarino, and L. R. Walker, *Phys. Rev. Lett.* **15**, 258 (1965).
- [100] L. Liebermann, J. Clinton, D. Edwards and J. Mathon, *Phys. Rev. Lett.* **25**, 232 (1970).
- [101] K. H. Ayashi, M. Sawada, H. Y. Amagami, A. K. Imura and A. K. Akizaki, *J. Phys. Soc. Japan* **73**, 2550 (2004).
- [102] M. A. Tomaz, D. C. Ingram, G. R. Harp, D. Lederman, E. Mayo and W. L. O'Brien, *Phys. Rev. B* **56**, 5474 (1997).
- [103] M. A. Tomaz, E. Mayo, D. Lederman, E. Hallin, T. K. Sham, W. L. O'Brien and G. R. Harp, *Phys. Rev. B* **58**, 11493 (1998).

-
- [104] S. Dennler, J. Hafner, M. Marsman, J. Morillo, Phys. Rev. B **71**, 094433 (2005).
- [105] M. Marathe, M. Imam and S. Narasimhan, Appl. Surf. Sci., **256**, 449 (2009).
- [106] J. L. Stevens and R. Q. Hwang, Phys. Rev. Lett. **74**, 2078 (1995).
- [107] M. Schick, G. Ceballos, Th. Peizer, J. Schäffer, G. Ranglov, J. Stober and K. Wandelt, J. Vac. Sci. Technol. A **12**, 1795 (1994).
- [108] D. O. Boerma, G. Dorenbos, G. H. Wheatley, T. M. Buck, Surf. Sci. **674**, 307 (1994).
- [109] S. Mehendale, Y. Girard, V. Repain, C. Chacon, J. Lagoute, S. Rousset, M. Marathe, and S. Narasimhan, Phys. Rev. Lett. **105**, 056101 (2010).
- [110] W. Hume-Rothery, and H. M. Powell, Z. Krist., **91**, 23 (1935).
- [111] Alloy Phase Diagram ASM Handbook; Hugh, B., Eds.; ASM International: Cleveland, OH, 1992; Vol. 3, Chapter 2, p27.
- [112] J. Kübler, Physica B **127**, 257 (1984).
- [113] S. C. Wang, and G. Ehrlich, Phys. Rev. Lett. **67**, 2509 (1991).
- [114] R. Q. Hwang, J. Schröder, C. Günther, and R. J. Behm, Phys. Rev. Lett. **67**, 3279 (1991).
- [115] S. Rousset, S. Chiang, D. E. Fowler, and D. D. Chambliss, Phys. Rev. Lett. **69**, 3200 (1992).

-
- [116] D. D. Chambliss, and S. Chiang, *Surf. Sci.* **264**, L187 (1992).
- [117] L. P. Nielsen, F. Besenbacher, I. Stensgaard, and E. Laegsgaard, *Phys. Rev. Lett.* **71**, 754 (1993).
- [118] H. Röder, R. Schuster, H. Brune, and K. Kern, *Phys. Rev. Lett.* **71**, 2086 (1993).
- [119] J. Neugebauer, and M. Scheffler, *Phys. Rev. Lett.* **71**, 577 (1993).
- [120] J. Yuhara, M. Schmid, and P. Varga, *Phys. Rev. B* **67**, 195407 (2003).
- [121] M. Schick, J. Schäfer, K. Kalki, G. Ceballos, P. Reinhardt, H. Hoffschulz, and K. Wandelt, *Surf. Sci.* 287-288, 960 (1993).
- [122] B. Sadigh, M. Asta, V. Ozolinš, A. K. Schmid, N. C. Bartelt, A. A. Quong, and R. Q. Hwang, *Phys. Rev. Lett.* **83**, 1379 (1999).
- [123] G. E. Thayer, N. C. Bartelt, V. Ozolinš, A. K. Schmid, S. Chiang, and R. Q. Hwang, *Phys. Rev. Lett.* **89**, 036101 (2002).
- [124] M. M. Blener, J. Blener, R. Schalek, and C. M. Friend, *Surf. Sci.* **594**, 221 (2005).
- [125] P. Liu, J. A. Rodriguez, J. T. Muckermann, and J. Hrbek, *Phys. Rev. B* **67**, 155416 (2003).
- [126] P. T. Sprunger, E. Laegsgaard, and F. Besenbacher, *Phys. Rev. B* **54**, 8163 (1996).
- [127] P. Hu, A. Wander, L. Morales de la Garza, M. P. Bessent, and D. A. King, *Surf. Sci. Lett.* **286**, L542 (1993).

-
- [128] X. K. Shu, P. Jiang, and J. G. Che, *Surf. Sci.* **545**, 199 (2003).
- [129] G. A. Attard, and D. A. King, *Surf. Sci.* **188**, 589 (1987).
- [130] H. Takahashi, M. Sasaki, S. Suzuki, S. Sato, T. Abukawa, S. Kono, and J. Osterwalder, *Surf. Sci.* **304**, 65 (1993).
- [131] J. Tersoff, *Phys. Rev. Lett.* **74**, 434 (1995).
- [132] R. Q. Hwang, *Phys. Rev. Lett.* **76**, 4757 (1996).
- [133] R. Q. Hwang, and M. C. Bartelt, *Chem. Rev.* **97**, 1063 (1997).
- [134] E. D. Tober, R. F. C. Farrow, R. F. Marks, G. Witte, K. Kalki, and D. D. Chambliss, *Phys. Rev. Lett.* **81**, 1897 (1998).
- [135] T. Volkmann, F. Much, M. Biehl, and M. Kotrla, *Surf. Sci.* **586**, 157 (2005).
- [136] M. Walther, M. Biehl, and W. Kinzel, *Physica Status Solidi (C)* **4**:3210-3220, (2007).
- [137] S. Weber, M. Biehl, W. Kinzel, and M. Kotrla, *J. Phys.: Condens. Matter* **20**, 265004 (2008).
- [138] R. S. Berry, J. Burdett, and A. W. Castleman, *Z. Physik* **26**, (1993).
- [139] F. A. Reuse, and S. N. Khanna, *Chem. Phys. Lett.* **234**, 77 (1995).
- [140] M. Castro, C. Jamorski, and D. R. Salahub, *Chem. Phys. Lett.* **271**, 133 (1997).

-
- [141] J. G. Louderback, A. J. Cox, L. J. Lising, D. C. Douglass, and L. A. Bloomfield, *Z. Physik D* **26**, 301 (1993).
- [142] S. N. Khanna, and S. Linderoth, *Phys. Rev. Lett.* **67**, 742 (1991).
- [143] B. V. Reddy, S. N. Khanna, and B. I. Dunlap, *Phys. Rev. Lett.* **70**, 3323 (1993).
- [144] A. J. Cox, J. G. Louderback, and L. Bloomfield, *Phys. Rev. Lett.* **71**, 923 (1993).
- [145] M. Weissmann, G. Garca, M. Kiwi, R. Ramirez, and C. Fu, *Phys. Rev. B* **73**, 125435 (2006).
- [146] A. Winkler, T. Mühl, S. Menzel, R. Kozhuharova-Koseva, S. Hampel, A. Leonhardt, and B. Büchner, *J. App. Phys.* **99**, 104905 (2006).
- [147] F. Wolny, U. Weissker, T. Mühl, A. Leonhardt, S. Menzel, A. Winkler, and B. Büchner, *J. App. Phys.* **104**, 064908 (2008).
- [148] R. Klingeler, S. Hampel, and B. Büchner, *Int. J. Hyperthermia* **24**, 496 (2008).
- [149] H.J. Elmers, J. Hauschild, H. Höche, U. Gradmann, H. Bethge, D. Heuer, and U. Köhler, *Phys. Rev. Lett.* **73**, 898 (1994).
- [150] M. Komelj, C. Ederer, J. W. Davenport, and M. Föhnle, *Phys. Rev. B* **66**, 140407 (2002).
- [151] P. Gambardella, M. Blanc, H. Brune, K. Kühnke, and K. Kern, *Phys. Rev. B* **61**, 2254 (2000).

-
- [152] S. M. York, and F. M. Leibsle, Phys. Rev. B **64**, 33411 (2001).
- [153] R. Družinić, and W. Hübner, Phys. Rev. B **55**, 347 (1997).
- [154] V. Bellini, N. Papanikolaou, R. Zeller, and P. H. Dederichs, Phys. Rev. B **64**, 094403 (2001).
- [155] A. B. Klautau, and S. Frota-Pessôa, Phys. Rev. B **70**, 193407 (2004).
- [156] B. Lazarovits, L. Szunyogh, P. Weinberger, and B. Ujfalussy, Phys. Rev. B **68**, 024433 (2003).
- [157] B. Lazarovits, L. Szunyogh, and P. Weinberger, Phys. Rev. B **67**, 024415 (2003).
- [158] A. Delin, E. Tosatti, and R. Weht, Phys. Rev. Lett. **92**, 057201 (2004).
- [159] S. R. Bahn, and K. W. Jacobsen, Phys. Rev. Lett. **87**, 266101 (2001).
- [160] C. Rau, C. Liu, A. Schmalzbauer, and G. Xing, Phys. Rev. Lett. **57**, 2311 (1986).
- [161] S. C. Wu, K. Garrison, A. Begley, F. Jona, and P. Johnson, Phys. Rev. B **49**, 14081 (1994).
- [162] A. Goldoni, A. Baraldi, G. Comelli, S. Lizzit, and C. Paolucci, Phys. Rev. Lett. **82**, 3156 (1999).
- [163] T. Bryk, D. M. Bylander, and L. Kleinman, Phys. Rev. B **61**, R3780 (2000).

-
- [164] R. Robles, J. Izquierdo, A. Vega, and L. C. Balbás, *Phys. Rev. B* **63**, 172406 (2001).
- [165] I. G. Batyrev, J.-H. Cho, and L. Kleinman, *Phys. Rev. B* **63**, 172420 (2001).
- [166] I. Morrison, D. M. Bylander, and L. Kleinman, *Phys. Rev. Lett.* **71**, 1083 (1993).
- [167] S. Ohnishi, C. L. Fu, and A. J. Freeman, *J. Magn. Magn. Mater.* **50**, 161 (1985).
- [168] R. L. Fink, C. A. Ballentine, J. L. Erskine, and J. A. Araya-Pochet, *Phys. Rev. B* **41**, 10175 (1990).
- [169] G. Bihlmayer, T. Asada, and S. Blügel, *Phys. Rev. B* **62**, R11937 (2000).
- [170] M. Weinert, S. Blügel, and P. D. Johnson, *Phys. Rev. Lett.* **71**, 4097 (1993).
- [171] I. Turek, S. Blügel, and J. Kudrnovsky, *Phys. Rev. B* **57**, R11065 (1998).
- [172] J. Redinger, S. Blügel, and R. Podloucky, *Phys. Rev. B* **51**, 13582 (1995).
- [173] S. Blügel, *Europhys. Lett.* **18**, 257 (1992).
- [174] S. Blügel, *Phys. Rev. Lett.* **68**, 851 (1992).
- [175] P. Giannozzi *et al.* *J. Phys. Condens. Matter* **21**, 395502 (2009).

-
- [176] N. W. Ashcroft and N. D. Mermin, *Solid State Physics* (Harcourt Asia, 2001), 1st ed.
- [177] S. K. Kwon, Z. Nabi, K. Kádas, L. Vitos, J. Kollár, B. Johansson, and R. Ahuja, *Phys. Rev. B* **72**, 235423 (2005).
- [178] T. B. Massalki, H. Okamoto, P. R. Subramanian, *Binary Alloy Phase Diagrams*, 2nd ed.; ASM International: Metals Park, OH, 1990.
- [179] M. Marathe, M. Imam, and S. Narasimhan, *Phys. Rev. B* **79**, 085413 (2009).
- [180] D. Spišák, and J. Hafner, *Phys. Rev. B* **70**, 014430 (2004).
- [181] R. Wu, and A. J. Freeman, *Phys. Rev. B* **45**, 7205 (1992).
- [182] C. L. Fu, A. J. Freeman, and T. Oguchi, *Phys. Rev. Lett.* **54**, 2700 (1985).
- [183] A. Ney, P. Pouloupoulos, and K. Baberschke, *Europhys. Lett.* **54**, 820 (2001).
- [184] J. S. Rowlinson, *Liquids and Liquid Mixtures* (Butterworth Scientific, London, (1982).
- [185] Jen-Hwa Hsu, Y. H. Huang, P. K. Tseng, and D. E. Chen, *IEEE Trans. on Mag.* **34**, 909 (1998).
- [186] M. A. Ruderman, C. Kittel, *Phys. Rev.* **96** (1954) 99.
- [187] O. Gunnarsson, *J. Phys. F: Met. Phys.* **6**, 587 (1976).

- [188] J. F. Janak, *Phys. Rev. B* **16**, 255 (1977).
- [189] Ph. Mavropoulos, S. Lounis, R. Zeller, and S. Blügel, *Appl. Phys. A* **82**, 103 (2006).
- [190] A. Baraldi, L. Bianchettin, E. Vesselli, S. De. Gironcoli, S. Lizzit, L. Petaccia, G. Zampieri, G. Comelli, and R. Rosci, *New J. Phys.* **9**, 143 (2007).
- [191] A. Ulman, *Chem. Rev.* **96**, 1533 (1996).
- [192] A. Ulman, *An Introduction to Ultrathin Organic Films Academic*, Boston, (1991).
- [193] F. Schreiber, *Prog. Surf. Sci.* **65**, 151 (2000).
- [194] R. G. Nuzzo, F. A. Fusco, D. L. Allara, *J. Am. Chem. Soc.* **109**, 2358 (1987).
- [195] M. Brust, M. Walker, D. Bethell, D. J. Schiffrin, R. Whyman, *J. Chem. Soc., Chem. Commun.*, **7**, 801 (1994).
- [196] P. J. Thomas, G. U. Kulkarni, C. N. R. Rao, *J. Nanosci. Nanotechnol.* **1**, 267 (2001).
- [197] X. Gao, K. Tam, K. M. K. Yu, S. C. Tsang, *Small*, **1**, 949 (2005).
- [198] R. J. Forster, T. E. Keyes, J. G. Vos, *Interfacial Supramolecular Assemblies*, Wiley. pp. 8894 (2003).
- [199] Z. H. Xiong, Di Wu, Z. V. Vardeny J. Shi, *Nature* **427**, 821 (2004).

- [200] S. J. Xie, K. H. Ahn, D. L. Smith, A. R. Bishop, A. Saxena, *Phys. Rev. B* **67**, 125202 (2003).
- [201] P. G. Hoertz, J. R. Niskala, P. Dai, H. T. Black, W. You, *J. Am. Chem. Soc.* **130**, 9763 (2008).
- [202] Y. Wu, Z. Xu, B. Hu, J. Howe, *Phys. Rev. B* **75**, 035214 (2007).
- [203] C. Lopez-Carls, T. C. Rojas, R. Litran, D. Martnez-Martnez, J. M. de la Fuente, S. Penades, A. Fernandez, *J. Phys. Chem. B* **109**, 8761 (2005).
- [204] S. Z. Deng, H. M. Fan, M. Wang, M. R. Zheng, J. B. Yi, R. Q. Wu, H. R. Tan, C. H. Sow, J. Ding, Y. P. Feng, K. P. Loh, *ACS Nano* **4**, 495 (2010).
- [205] M. A. García, J. M. Merino, E. Fernández Pinel, A. Quesada, J. de la Venta, M. L. Ruíz González, G. R. Castro, P. Crespo, J. Llopis, J. M. González-Calbet, and A. Hernando, *Nano Lett.* **7**, 1489 (2007).
- [206] M. S. Seehra, P. Dutta, S. Neelshwar, Y. Y. Chen, C. L. Chen, S. W. Chou, C. C. Chen, C. L. Dong, C. L. Chang, *Adv. Mater.* **20**, 1656 (2008).
- [207] E. Velu, C. Dupas, D. Renard, J. D. Renard, J. Sciden, *Phys. Rev. B* **37**, 668 (1988).
- [208] R. Allenspach, M. Stampanoni, A. Bischof, *Phys. Rev. Lett.* **65**, 3344 (1990).

-
- [209] M. Speckmann, H. P. Oepen, H. Ibach, Phys. Rev. Lett. **75**, 2035 (1995).
- [210] M. Dreyer, M. Kleiber, A. Wadas, R. Wiesendanger, Phys. Rev. B **59**, 4273 (1999).
- [211] L. Szunyogh, B. Ujfalussy, P. Bruno, P. Weinberger, J. Mag. Mag. Mater. **165**, 254 (1997).
- [212] P. Campiglio *et al.*, (unpublished) Private communication.
- [213] A. Ayuela, P. Crespo, A. Hernando, M.A. Garcia, P. M. Echenique, arXiv:1101.4109v1 [cond-mat.mtrl-sci] 21 Jan 2011.
- [214] D. Kruger, H. Fuchs, R. Rousseau, D. Marx, M. Parrinello, J. Chem. Phys. **115**, 4776 (2001).
- [215] H. Sellers, Surf. Sci. **294**, 99 (1993).
- [216] M. Grandbois, M. Beyer, M. Rief, H. Clausen-Schaumann, H. E. Gaub, Science **283**, 1727 (1999).
- [217] C. Chappert, P. Bruno, J. Appl. Phys. **64**, 5736 (1988).
- [218] B. Voigtländer, G. Meyer, N. M. Amer, Phys. Rev. B **44**, 10354 (1991).
- [219] J. Pommier, P. Meyer, G. Penissard, P. Bruno, F. Ferre, D. Renard, Phys. Rev. Lett. **65**, 2054 (1990).
- [220] J. L. Bubendorff, E. Beaupaire, C. Mény, P. Panissod, and J. P. Bucher, Phys. Rev. B **56**, R7120 (1997).

-
- [221] N. Marsot, R. Belkhou, H. Magnan, P. Le Fevre, C. Guillot, D. Chandris, *Phys. Rev. B* **59**, 3135 (1999).
- [222] K. Hyomi, A. Murayama, Y. Oka, U. Hiller, and C. M. Falco, *Appl. Phys. Lett.* **80**, 282 (2002).
- [223] Y. Girard, G. Baudot, V. Repain, S. Rohart, S. Rousset, A. Coati, Y. Garreau, *Phys. Rev. B* **72**, 155434 (2005).
- [224] C. D. Bain, J. Evall, J. M. Whitesides, *J. Am. Chem. Soc.* **111**, 7155 (1989).
- [225] M. E. Castro, J. M. White, *Surf. Sci.* **257**, 22 (1991).
- [226] G. J. Jackson, D. P. Woodruff, R. G. Jones, N. K. Singh, A. S. Y. Chan, B. C. C. Cowie, V. Formoso, *Phys. Rev. B* **84**, 119 (2000).
- [227] P. Bruno, *Phys. Rev. B* **39**, 865 (1989).
- [228] C. Andersson, B. Sanyal, O. Eriksson, L. Nordström, O. Karis, and D. Arvanitis, T. Konishi, E. Holub-Krappe, J. H. Dunn, *Phys. Rev. Lett.* **99**, 177207 (2007).
- [229] R. G. Nuzzo, L. H. Dubois, D. L. Allara, *J. Am. Chem. Soc.* **112**, 558 (1990).
- [230] J. B. Schlenoff, M. Li, H. Ly, *J. Am. Chem. Soc.* **117**, 12528 (1995).
- [231] N. Camillone III, T. Y. B. Leung, G. Scoles, *Surf. Sci.* **373**, 333 (1997).
- [232] H. Kondoh, C. Kodama, H. Sumida, H. Nozoye, *J. Chem. Phys.* **111**, 1175 (1999).

-
- [233] E. Barrena, C. Ocal, M. Salmeron, *J. Chem. Phys.* **111**, 9797 (1999).
- [234] A. Ferral, P. Paredes-Olivera, V. A. Macagno, E. M. Patrino, *Surf. Sci.* **525**, 85 (2003).
- [235] H. Grönbeck, A. Curioni, W. Andreoni, *J. Am. Chem. Soc.* **122**, 3839 (2000).
- [236] A. N. Caruso, L. G. Wang, S. S. Jaswal, E. Y. Tsybal, P. A. Dowben, *J. Mater. Sci.* **41**, 6198 (2006).
- [237] L. G. Wang, E. Y. Tsybal, S. S. Jaswal, *Phys. Rev. B* **70**, 075410 (2004).
- [238] L. G. Wang, E. Y. Tsybal, S. S. Jaswal, *J. Magn. Magn. Mat.* **286**, 119 (2005).
- [239] S. H. Ma, X. T. Zu, Z. Y. Jiao, H. Y. Xiao, *Eur. Phys. J. B* **61**, 319 (2008).
- [240] J. Lahtinen, P. Kantola, S. Jaatinen, K. Habermehl-Cwirzen, P. Salo, J. Vuorinen, M. Lindroos, K. Pussi, A. Seitsonen, *Surf. Sci.* **599**, 113 (2005).
- [241] E. Guerrero, M. A. Muñoz-Márquez, M. A. García, P. Crespo, E. Fernández-Pinel, A. Hernando, A. Fernández, *Nanotechnology* **19**, 175701 (2008).
- [242] I. Carmeli, G. Leitun, R. Naaman, S. Reich and Z. Vager, *J. Chem. Phys.* **118**, 10372 (2003).

- [243] S. Reich, G. Leitius, Y. Feldman, Appl. Phys. Lett. **88**, 222502 (2006).
- [244] P. Crespo, R. Litrán, T. C. Rojas, M. Multigner, J. M. de la Fuente, J. C. Sánchez-López, M. A. García, A. Hernando, S. Penadés, and A. Fernández, Phys. Rev. Lett. **93**, 087204 (2004).
- [245] A. Harnando, P. Crespo, M. A. Garcia, Phys. Rev. Lett. **96**, 057206 (2006).
- [246] J. V. Barth, H. Brunc, G. Ertl, R. J. Behm, Phys. Rev. B **42**, 9307 (1990).
- [247] K. Tamada, M. Hara, H. Sasabe, W. Knoll, Langmuir **13**, 1558 (1997).
- [248] Z. Suo, Y. F. Gao, J. Scoles, J. Appl. Mech. **71**, 24 (2004).
- [249] Z. Vager, I. Carmeli, G. Leitius, S. Reich, R. Naaman, J. Phys. Chem. Solids **65**, 713 (2004).
- [250] J. A. C. Bland and B. Heinrich (ed) *Ultrathin Magnetic Structures: I* (Berlin: Springer) (1994).
- [251] M. N. Baibich, J. M. Broto, A. Fert, F. Van Dau Nguyen, F. Petroff, P. Etienne, G. Creuzet, A. Friederich and J. Chazelas Phys. Rev. Lett. **61**, 2472 (1988).
- [252] N. H. Yeh, J. Magn. Soc. Jpn. **21**, 269 (1997).
- [253] J. G. Gay, and R. Richter, Phys. Rev. Lett. **56**, 2728 (1986).
- [254] E. Ising, Z. Phys. **31**, 253 (1925).

-
- [255] N. D. Mermin, and H. Wagner, *Phys. Rev. Lett.* **17**, 1133 (1966).
- [256] P. Gambardella, A. Dallmeyer, K. Maiti, M. C. Malagoli, W. Eberhardt, K. Kern and C. Carbone *Nature* **416**, 301 (2002).
- [257] J. Shen, R. Skomski, M. Klaua, H. Jenniches, S. S. Manoharan, and J. Kirschner, *Phys. Rev. B* **56**, 2340 (1997).
- [258] J. Hauschild, H. J. Elmers, and U. Gradmann, *Phys. Rev. B* **57**, R677 (1998).
- [259] G. Autès, C. Barreteau, D. Spanjaard, and M. C Desjonquères, *J. Phys.:Condens. Matter* **18**, 6785 (2006).
- [260] R. Sabirianov, *J. Magn. Magn. Mater.* **300**, 136 (2006).
- [261] J. C. Tung, G. Y. Guo, *Phys. Rev. B* **76**, 094413 (2007).
- [262] M. C. Desjonquères, C. Barreteau, G. Autès, and D. Spanjaard, *Phys. Rev. B* **76**, 024412 (2007).
- [263] R. Mazzarello, E. Tosatti, *Phys. Rev. B* **79**, 134402 (2009).
- [264] Y. Mokrousov, G. Bihlmayer, and S. Blugel, *Phys. Rev. B* **72**, 045402 (2005).
- [265] P. Ohresser, N. B. Brookes, S. Padovani, F. Scheurer, and H. Bulou, *Phys. Rev. B* **64**, 104429 (2001).
- [266] P. Ohresser, G. Chiringhelli, O. Tjernberg, N. B. Brookes, and M. Finazzi, *Phys. Rev. B* **62**, 5803 (2000).

-
- [267] R. Cheng, K. Yu. Guslienko, F. Y. Fradin, J. E. Pearson, H. F. Ding, Dongqi Li, and S. D. Bader, *Phys. Rev. B* **72**, 014409 (2005).
- [268] C. Li, A. J. Freeman, H. J. F. Jansen, C. L. Fu, *Phys. Rev. B* **42**, 5433 (1990).
- [269] K. Nakamura, T. Ito, A. J. Freeman, L. Zhong, and J. Fernandez-de-Castro, *Phys. Rev. B* **67**, 014420 (2003).
- [270] L. Szunyogh, B. Ujfalussy, P. Weinberger, *Phys. Rev. B* **51**, 9552 (1995).
- [271] G. Y. Guo, W-M. Temmerman, H. Ebert, *J. Phys. Condens. Matter* **3**, 8205 (1991).
- [272] R. Hammerling, C. Uiberacker, J. Zabloudil, and P. Weinberger, *Phys. Rev. B* **66**, 052402 (2002).
- [273] J. A. Stroschio, D. T. Pierce, R.A. Dragoset, and P.N. First, *J. Vac. Sci. Technol. A* **10**, 1981 (1992).
- [274] J. Xu, M. A. Howson, P. Hucknall, B. J. Hickey, R. Venkataraman, C. Hammond, M. J. Walker, and D. Greig, *J. Appl. Phys.* **81**, 3908 (1997).
- [275] V. Rodrigues, T. Fuhrer, and D. Ugarte, *Phys. Rev. Lett.* **85**, 4124 (2000).
- [276] R. H. M. Smit, C. Untiedt, A. I. Yanson and J. M. van Ruitenbeek, *Phys. Rev. Lett.* **87**, 266102 (2001).

-
- [277] Y. Oshima, H. Koizumi, K. Mouri, H. Hirayama, K. Takayanagi and Y. Kondo, *Phys. Rev. B* **65**, 121401 (2002).
- [278] C. Chappert, P. Bruno, B. Bartenlian, P. Beauvillain, A. Bounouh, R. Megy, and P. Vcillet, *J. Magn. Magn. Mater.* **148**, 165 (1995).
- [279] O. Toulemonde, V. Petrov, A. N. Abdi, and J. P. Bucher, *J. Appl. Phys.* **95**, 6565 (2004).
- [280] T. Allmers, and M. Donath, *Phys. Rev. B* **81**, 064405 (2010).
- [281] B. Voigtlander, G. Meyer, and N. M. Amer, *Surf. Sci. Lett.* **255**, L529 (1991).
- [282] G. Lugert, W. Robl, L. Pfau, M. Brockmann, and G. Bayreuther, *J. Magn. Magn. Mater.* **121**, 498 (1993).
- [283] K. Kyuno, R. Yamamoto, S. Asano, *Model. Simul. Mater. Sci. Eng.*, **1**, 133 (1993).
- [284] N. Takuchi, C. T. Chan, and K. M. Ho, *Phys. Rev. B* **43**, 899 (1991).
- [285] S. Grimme, *J. Comput. Chem.* **25**, 1463 (2004).
- [286] M. Dion, H. Rydberg, E. Schröder, D. C. Langreth and B. I. Lundqvist, *Phys. Rev. Lett.* **92**, 246401 (2004).
- [287] N. Sandhyarani and T. Pradeep, *Int. Rev. Phys. Chem.* **22**, 221 (2003).

Appendix A

Pseudopotentials Used

The information about the pseudopotentials (such as electronic configuration, cutoff radii, whether or not the nonlinear core corrections (NLCC) are applied, and the type of the functional (LDA or GGA)), are given in this appendix (see the table on the next page). We used scalar-relativistic as well as fully-relativistic pseudopotentials in our calculations. The fully-relativistic pseudopotentials are indicated by “rel” in the name of the corresponding PP, given in the table. All the pseudopotentials (except the relativistic Fe) were taken from the Quantum ESPRESSO website (<http://www.quantum-espresso.org>).

The relativistic Fe pseudopotential was provided by Cyrille Barreateau from CEA-Saclay, France. All the PPs, with the exception of relativistic one for sulfur, are ultrasoft. The cutoff radii are those of the ultrasoft wavefunctions (norm-conserving in the case of relativistic pseudopotential of sulfur).

Table A.1: Pseudopotentials (PP) used in our calculations. “T” or “F” in the column of nonlinear core correction (NLCC) stands for whether the nonlinear core correction was or was not applied, respectively.

El.	PP	Val. elec. config.	cutoff radii (a.u.)	NLCC	Functional
H	H.pz-rrkjus.UPF	$1s^1 2p^0$	1.2, 1.1	F	LDA
H	H.rel-pz-rrkjus.UPF	$1s^1 2p^0$	1.1, 1.1	F	LDA
C	C.pz-rrkjus.UPF	$2s^2 2p^2$	1.6, 1.6	F	LDA
C	C.rel-pz-rrkjus.UPF	$2s^2 2p^2$	1.7, 1.7	F	LDA
S	S.pz-van.ak.UPF	$3s^2 3p^4$	1.7, 1.7	F	LDA
S	S.rel-pz-rrkj.UPF	$3s^2 3p^4$	1.9, 2.1	F	LDA
Fe	Fe.pz-nd-rrkjus.UPF	$3d^7 4s^1 4p^0$	2.2, 2.2, 2.3	T	LDA
Fe	Fe.pbe-nd-rrkjus.UPF	$3d^7 4s^1 4p^0$	2.2, 2.2, 2.3	T	GGA
Fe	Fe.rel_LDA.RRKJ3.UPF	$3d^7 4s^1 4p^0$	2.2, 2.2, 2.3	T	LDA
Co	Co.pz-nd-rrkjus.UPF	$3d^8 4s^1 4p^0$	2.1, 2.5, 2.6	T	LDA
Co	Co.pbe-nd-rrkjus.UPF	$3d^8 4s^1 4p^0$	2.1, 2.5, 2.6	T	GGA
Co	Co.rel-pz-n-rrkjus.UPF	$3d^8 4s^1 4p^0$	2.1, 2.5, 2.6	T	LDA
Ni	Ni.pbe-nd-rrkjus.UPF	$3d^9 4s^1 4p^0$	2.5, 2.5, 2.6	T	GGA
Rh	Rh.pbe-nd-rrkjus.UPF	$4d^7 5s^2 5p^0$	2.5, 2.3, 2.6	T	GGA
Ag	Ag.pbe-d-rrkjus.UPF	$4d^{10} 5s^1 5p^0$	2.4, 2.3, 2.5	F	GGA
Cd	Cd.pbe-n-van.UPF	$4d^{10} 5s^2 5p^0$	2.1, 2.5, 2.5	T	GGA
Pt	Pt.pbe-nd-rrkjus.UPF	$5d^9 6s^1 6p^0$	2.4, 2.6, 2.6	T	GGA
Au	Au.pz-d-rrkjus.UPF	$5d^{10} 6s^1 6p^0$	2.4, 2.7, 3.3	F	LDA
Au	Au.pbe-nd-rrkjus.UPF	$5d^{10} 6s^1 6p^0$	2.4, 2.5, 3.3	T	GGA
Au	Au.rel-pz-rrkjus.UPF	$5d^{10} 6s^1 6p^0$	2.4, 2.7, 3.3	F	LDA
Pb	Pb.pbe-d-van.UPF	$5d^{10} 6s^2 6p^2$	2.3, 2.5, 2.5	F	GGA

620.112 97

P12

Recd. on
12/6/12

Display till 10/7/12.



236
30

266